Microwave Quantum Optics using Giant Artificial Atoms and Parametrically Coupled Superconducting Cavities

by

Vadiraj Manjunath Ananthapadmanabha Rao

A thesis
presented to the University of Waterloo
in fulfillment of the
thesis requirement for the degree of
Doctor of Philosophy
in
Electrical and Computer Engineering

Waterloo, Ontario, Canada, 2020

Examining Committee Membership

The following served on the Examining Committee for this thesis. The decision of the Examining Committee is by majority vote.

External Examiner:	Dr. Kater Murch Associate Professor, Dept. of Physics, Washington University in St.Louis
Supervisor(s):	Dr. Christopher Wilson Professor, Dept. of Electrical and Computer Engineering, University of Waterloo
Internal Member:	Dr. Michal Bajcsy Assistant Professor, Dept. of Electrical and Computer Engineering, University of Waterloo
Internal Member(s):	Dr. Slim Boumaiza Professor, Dept. of Electrical and Computer Engineering, University of Waterloo
Internal-External Member:	Dr. Kyung Soo Choi Assistant Professor, Dept. of Physics and Astronomy, University of Waterloo

Author's Declaration

I hereby declare that I am the sole author of this thesis. This is a true copy of the thesis, including any required final revisions, as accepted by my examiners.

I understand that my thesis may be made electronically available to the public.

Abstract

Artificially engineered atoms, built using superconducting electrical circuits, have had a broad impact on the field of quantum information and quantum computing. Based on the Josephson effect, superconducting qubits have provided a robust platform for engineering light-matter interactions at the single-photon level. The ability to precisely control and manipulate single photons using superconducting qubits and cavities, a field now popularly known as circuit quantum electrodynamics (circuit QED), has enabled new and novel regimes in quantum physics, which previously remained inaccessible. For instance, the coupling between individual photons and artificial atoms have been shown to reach the ultrastrong and deep-strong regimes, a feat which is difficult to achieve with natural atoms. The superconducting circuit platform is now a promising contender for building large-scale quantum processors, attracting large investments from academic, industry and government players.

This thesis uses superconducting circuits to engineer photon interactions in two separate studies. The first is aimed at studying the physics of "giant" artificial-atoms. The second study explores the route towards building a quantum heat engine using two parametrically-coupled, superconducting microwave cavities. We review the theoretical ideas and concepts which motivate our work, along with discussions of the design methodology, simulations, fabrication, measurement setup and the experimental findings.

In the first study, we explore a giant artificial atom, formed from a transmon qubit, which is coupled to propagating microwaves at multiple points along an open transmission line. The multipoint coupling nature of the transmon allows its radiated field to interfere with itself leading to some striking "giant" atom effects. For instance, we observe strong frequency dependent couplings of the transmon's transition levels to its electromagnetic environment, a feature which is not observed with ordinary artificial atoms. We measure large on/off ratios, as high as 380, for the coupling rate of the $|0\rangle - |1\rangle$ transition. Furthermore, we show that we can enhance or suppress the coupling rate of the $|1\rangle - |2\rangle$ transition relative to the $|0\rangle - |1\rangle$ transition, by more than a factor of 200. The relative modulation of the coupling rates was exploited to engineer a metastable state in the giant transmon and demonstrate electromagnetically-induced transparency (EIT), a typical signature of a lambda system. Our results show that we can transform the ladder structure of an ordinary transmon into a more interesting lambda system using a giant transmon, thereby paving the way for exploring new possibilities to study three-level physics in a waveguide-QED setting.

Extending giant atom physics to multiple giant atoms, we then explore a device with two giant artificial atoms connected in a braided configuration to a transmission line. The

braided topology of the qubits, offers an interesting regime where the qubits can interact with each other in a decoherence-free environment, where the interaction is mediated by virtual photons in the transmission line. We probe the resonant behavior of the qubits at two different frequency bias points, where we observe qualitatively different scattering behavior. Furthermore, when probing for the Autler-Townes Splitting (ATS), multiple resonances are observed for both resonant and off-resonant cases instead of the familiar doublet in the ATS spectroscopy. This comes as a surprise as the frequency-level spacings in both qubits are nominally identical. We believe these features could be an indication of a novel resonant interaction between the qubits facilitated by the braided topology. An effort to understand this theoretically is underway.

For our second study, we explore a system with two parametrically-coupled superconducting resonators, which implements an optomechanical-like interaction in an all-electrical network. The nonlinear nature of this interaction is mediated by a superconducting quantum interference device (SQUID), where the current in one resonator couples to the photon number in the other resonator. We propose to use this system to build a "photonic piston" engine in the quantum regime. We motivate the feasibility of the proposal by reviewing key theoretical results which demonstrate an Otto-cycle by appropriately driving the system with noise. Our experimental findings demonstrate the crucial nonlinear coupling that is required for the engine to work. We also show that we can increase the coupling strength between the resonators depending on the chosen flux operating point.

Acknowledgements

I would like to take this opportunity to thank all the people who have motivated and encouraged me to pursue the path of science, which now has become my job for life. Graduate studies is a long and stressful process, apart from the rich experiences it offers to a developing student in forming his/her personality and character. The struggles are many, the journey is alive and exciting and the reward is the satisfaction of having contributed to science, that will live on.

Firstly, I would like to thank my PhD supervisor, Christopher Wilson, for giving me an opportunity to pursue a PhD in Canada under his guidance. He has been a wonderful academic supervisor and I am fortunate to have trained under him. His profound knowledge of the scientific craft is something I admire and draw inspiration from. He has been very supportive during the difficult times when experiments didnt work and I am truly grateful for his generosity. Chris also gave me the academic freedom when it mattered most, which has helped me evaluate my own capabilities of working independently, and this thesis is a reminder of that. Chris's mentorship and my experiences with him, will continue to help me grow as I move on to my next scientific adventure.

My colleagues in the Engineered Quantum Systems Laboratory (EQSL), have been a constant support in helping me sail through my PhD journey. I am fortunate to have such a diverse and talented group of people as my colleagues. I have learnt a great deal from them. I would like to thank Pol and Sandbo for helping me get started and making my transition into the lab, a smooth one. Pol, you were an amazing PostDoc and I could not have asked for a better mentor apart from Chris. You were my go to guy for questions, conversations and guidance, academic or otherwise. I thank you for your patience. Sandbo, we started around the same time as PhD students. I admire your sense of dedication, attention to detail and the discipline that you showed towards your work. From late night fabrication exercises to running fridges, from doing measurements to having discussions, I enjoyed working alongside you for all these years. You were a great office mate too!. I would like to also thank Ibrahim, with whom I spent a lot of time in the cleanroom. your hardworking nature inspires me. I have learnt a great deal working alongside you trying to develop recipes and solve fabrication issues. Lastly, I would like to thank all the EQSL members, past and present, Chris Warren, Helen, Gaurav, Ingrid, Karthik, Mehran, Jimmy, Jamal, Huichen, Dima, Nizar and Luyao.

The devices presented in thesis thesis were fabricated in house at the Quantum Nanofab of the university. Having access to expensive fabrication tools is a privilege. Keeping them running and in prime condition is an extremely important part of the research process. I am

extremely grateful to the team members of the Nanofab, Vito, Nathan, Brian, Rod, Matt, Lino, Greg and Mai who give their best to ensure the smooth operations of the cleanroom. The support I received from each one of you has contributed towards the completion of my PhD research. I also would like to thank Alex Mitrovic, who machined the sample box used in this thesis. I enjoyed our conversations about our shared passion of machining. I thank Steve for helping us with providing support for data backups and setting up of a server for HFSS simulations. I would like to also acknowledge CMC for their CAD Compute cluster, which has been instrumental for running my heavy duty simulations.

I would not have reached this point, if not for the contributions of all my teachers and professors of my alma mater, who I have had the privilege to learn from. My salutations and heartfelt thanks to all of them. Prior to coming to Canada, I spent a good amount of time at the Tata Institute of Fundamental Research, in India, under the guidance of Vijay, helping to setup a superconducting circuits lab. I am indebted to Vijay for having been a source of support and for giving me the opportunity to spend time learning about superconducting circuits, both in theory and practical. Everything that I learnt from you proved valuable for my graduate studies.

Lastly but not the least, I would thank all friends and colleagues in IQC, who I was fortunate to meet while in Canada. They have had a positive effect on my life and I am thankful for all the wonderful moments and experiences I have shared with them. I thank Rahul, Idhaya, Aditya, J. Flannery, J. Bejanin, Bipin, Sreesh, Nikhil, Julia, Manjeet, Irene, among many others. Thank you all.

Dedication

This work of love would not have been possible without the constant support and love that I have received from my parents, my sister, extended family and friends. I am especially grateful to my parents for their patience and encouragement. To these beautiful people in my life, I dedicate this thesis.

Table of Contents

List of Figures

List of Tables

Chapter 1

Introduction

1.1 Waveguide quantum electrodynamics with giant artificial atoms

Light-matter interaction (LMI) has been one of the most widely explored phenomena in physics. In the microscopic limit, quantum-mechanical interactions can even be engineered between individual photons and atoms. Over the last decades, we have seen many seminal experiments where natural atoms are coupled to quantized electromagnetic fields in high-finesse optical and microwave cavities, a field known as cavity quantum electrodynamics (cavity QED) [1–4]. In more recent years, artificial atoms made using Josephson junctions were coupled to superconducting circuits to demonstrate new regimes of light-matter coupling in the microwave domain [5–10], a thriving field of research known as circuit QED.

The simplest theoretical treatments of LMI study the coupling of a two-level emitter, e.g., an atom or qubit, to one or more quantized electromagnetic (EM) modes using a series of approximations. The well-known Jaynes-Cummings model [11], which treats the coupling to a single EM mode, uses two key approximations. Firstly, the atom is treated as an ideal dipole, which is a valid approximation when the emitter is much smaller than the wavelength of light, as shown in Fig. 1.1(a). Secondly, the dynamics of the LMI are studied under the rotating-wave approximation (RWA), which is applicable when the light-matter coupling strength is still in the perturbative regime. This simplified treatment of LMI has been successful in explaining many phenomena in quantum optics with excellent agreement between theory and experiment [9]. In more complicated systems, where the emitter is coupled to a continuum of electromagnetic modes, the dipole approximation and

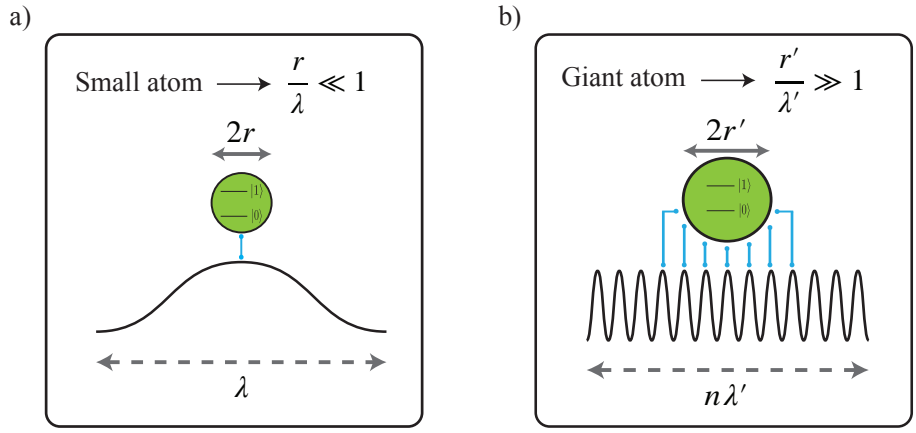

Figure 1.1: Small atom vs. a giant atom, coupled to an electromagnetic mode.

the RWA are still used with an additional, third assumption that the overall dynamics of the continuum are Markovian. The validity of the Markovian approximation is tied both to the small size of the emitter and the perturbative nature of the coupling.

Recent developments in microwave quantum optics using superconducting qubits coupled to open transmission lines, a field dubbed waveguide QED, have enabled experiments that demonstrate strong coupling of the qubit to the EM continuum [9, 12–18]. The ability to tightly confine and guide microwaves in these setups has opened up new avenues for single-photon routing [19], photon shaping [20], vacuum-mode engineering [21], interactions between distant qubits with collective decay effects [22], and observation of a large collective Lamb shift [23]. Flux qubits have been shown [7, 8] to operate in the so-called ultrastrong coupling regime [10], where the qubit's coupling rate to the EM continuum is comparable to its transition frequency, i.e., far beyond the perturbative regime. As a further consequence of this ultrastrong coupling, the EM spectral density seen by the emitter can no longer be approximated as frequency-independent, making the LMI a non-Markovian process. More recently, non-Markovian phenomena have been explored in a new setting where a transmon qubit is coupled to propagating phonons, in the form of surface acoustic waves (SAWs) [24]. Due to the slow velocity of the waves, the ratio of the size of the transmon to the wavelength of the SAW can be ~ 100 [25, 26] [see Fig. 1.1(b)]. In this limit, the dipole approximation clearly breaks down and new "giant atom" effects appear [27–30]. This includes scenarios where the qubit's radiated field can interfere with itself, creating a variety of non-Markovian behaviors [30–33]. For instance, nonexponential decay of the qubit was recently observed in such a system [24].

In this thesis, we explore a recent theoretical proposal to realize a giant artificial atom in a waveguide-QED system, where an otherwise conventional transmon qubit is coupled at multiple points to propagating microwaves in a transmission line (TL) [27]. The TL is suitably meandered with wavelength-scale distances between the coupling points. Even though the physical size of the transmon is small when compared to the wavelength of interest, the electric field at each coupling point in the TL is different. As a result, the transmon cannot be treated as a simple dipole, where the multipoint-coupling feature allows the emission amplitudes of the transmon to interfere with themselves, making it an effective giant artificial atom. This interference results in strongly frequency-dependent coupling of its many transitions, an effect that is not seen with an ordinary transmon [34]. Stronger modulation of the coupling strengths is made possible by increasing the number of coupling points [27]. We present experimental results comparing two separate giant transmons with different numbers of coupling points. We extract the coupling rates of the $|0\rangle - |1\rangle$ and $|1\rangle - |2\rangle$ transitions of the giant transmon as a function of frequency, and show that these can be strongly modulated. We further use this prototype system to engineer the giant transmon into an effective lambda system with a metastable excited state. As a benchmark of the system, we use it to demonstrate a phenomenon characteristic of lambda systems, namely, electromagnetically induced transparency (EIT).

The dynamics of the giant artificial atom was also studied in the setting of multiple giant atoms which are coupled to a TL [28]. The multi-point coupling nature was exploited to connect the giant atoms in various configurations. In the case of the braided configuration, these atoms were shown to interact in a decoherence-free environment mediated by virtual photons in the TL, a regime of qubit operation which has not been widely explored. The emergence of a decoherence-free space in a waveguide-QED architecture, where qubits are otherwise strongly coupled to a continuum of modes, is an exciting regime to explore photon mediated interactions between spatially separated qubits. This could pave way for new applications in quantum communication [35] and quantum simulation [36]. We explore a device with two giant artificial atoms connected in a braided configuration. Our experimental findings seem to suggest novel physics at play when the qubits are resonant with each other.

1.2 Towards quantum heat engines using superconducting resonators

Richard Feynman in his famous 1959 MIT talk "There's plenty of room at the bottom" [37] envisioned a scenario where heat engines could be built from single atoms. This insight of

Feynman has been one of the key driving forces in order to study thermodynamics in the quantum regime. Do the classical limits of thermodynamics apply to the quantum world? Can we build quantum heat engines which exceed the Carnot efficiency or does the efficiency bound still hold in the quantum case? Unless the theory is tested by appropriately designed experiments, these are open questions which still need answers. The field of quantum thermodynamics has progressed rapidly with emerging new theoretical ideas using quantum matter as a working substance [38–48] along with advances in experimental efforts [49–51].

Recently, O. Abah et al, [47] proposed a quantum heat engine using a single ion in a specially designed RF trap. They use the coupled vibrational modes of the ion to implement a quantum Otto cycle. Their proposal was realized in an experiment by Roßnagel et al [51], making Feynman's dream of building heat engines using single atoms a reality. Although this was an impressive demonstration, the dynamics of the engine were still classical owing to the dominant thermal noise.

Here, we propose to build a quantum heat engine analogous to the single-ion engine with tools borrowed from circuit QED. Johansson et al worked out the theory of a coupled resonator system using superconducting circuits, which implements a novel nonlinear coupling using a superconducting quantum interference device (SQUID) [52]. We realize that this system is a promising platform for implementing a "photonic-piston engine" with a potential to demonstrate an Otto cycle in the quantum regime [53], an all-electrical system to test some of the open questions in quantum thermodynamics. We explore the dynamics of the coupled-resonator device, which implements an optomechanical-like interaction Hamiltonian. We demonstrate the crucial nonlinear coupling between the resonators, a basic requirement for realizing an Otto-cycle in such a device.

1.3 Thesis overview

The thesis is structured in the following way. **Chapter 2** discusses the important theoretical ideas on which the the experimental results are based. The ideas are developed using well established concepts in circuit QED and microwave engineering, with key theoretical results borrowed in certain places. We begin by introducing the Josephson relations, a primary driver for building a key component in circuit QED, the Josephson junction, the only known nonlinear, lossless inductor. Two Josephson junctions in a closed superconducting loop form a SQUID, a nonlinear, tunable and lossless inductor. We then introduce the Cooper-pair box and its cousin, the transmon qubit, an artificial atom that is ubiquitous in circuit QED. In order to couple the qubit to the external environment to perform useful operations, microwave transmission lines and cavities are typically used in circuit QED.

We discuss the relevant microwave theory keeping in mind the devices that are studied in this thesis. A classical treatment of an artificial atom coupled to a transmission line is then presented. The chapter ends with a discussion on giant artificial atoms and on the implementation of a quantum heat engine with superconducting circuits. **Chapter 3** discusses the design methodology and the simulations performed to operate the devices in the right regime. Several variations were studied using commercially available electromagnetic simulation packages. Attempts to explain the observed experimental signatures and theoretical deviations are discussed by incorporating changes in the simulation parameters. **Chapter 4** introduces the fabrication process flow for making the devices discussed in this thesis. Critical steps during the fabrication process are reviewed. Also discussed are the various challenges and aspects of low temperature measurements. The fridge setup used in the measurements is also presented. **Chapter 5** presents our experimental results for the single giant transmon devices where we demonstrate strong frequency dependent couplings of the transmon's transition levels. We engineer the giant transmon as a lambda system and demonstrate electromagnetically-induced transparency (EIT). **Chapter 6** discusses the experimental results for a device with two giant transmons which are connected in a braided configuration. **Chapter 7** presents our experimental findings of a device which implements two parametrically coupled resonators with an optomechanical-like interaction Hamiltonian. We demonstrate the nonlinear interaction in the device, which is crucial for exploring the device as a quantum heat engine. In the end, **Chapter 8** summarises the overall conclusions from the work presented in this thesis.

Chapter 2

Background and Theory

This chapter introduces the theoretical ideas which form the basis of the physics explored in this thesis. At the heart of our devices is the Josephson junction, which provides the necessary nonlinearity in the system, making it possible to build artificial atoms and tunable microwave cavities. We will begin the discussion by introducing the Josephson equations and the superconducting quantum interference device (SQUID). Next, we will explore how a SQUID can be used in a macroscopic electrical circuit to mimic an artificial atom. Following standard textbook ideas, we will examine the properties of a microwave transmission line (TL), a key component for building microwave cavities (resonators). An artificial atom embedded in a microwave cavity or a TL is one of the most successful candidates for studying light-matter interaction (LMI) in the microwave regime, a growing field of research known as circuit QED. We will review this interaction of an artificial atom coupled to a TL, a prototype example of a typical waveguide-QED setup. We will then highlight the central results of giant artificial atoms coupled to a TL [27, 28]. Towards the end, we will explore a circuit that implements longitudinal coupling (optomechanical-like interaction) between two microwave cavities [52]. We will see how this setup can be used as a candidate prototype for building a quantum heat engine [52].

2.1 Superconductivity

One of the hallmarks of physics in the last century was the discovery of superconductivity by Heike Kamerlingh Onnes, a Dutch physicist, in 1911 [54]. He observed that the resistance of mercury dropped significantly at 4.2 K upon cooling it with liquid helium. This newly discovered state of matter, which he called the superconducting state, received widespread

attention, which ultimately led him to win a Nobel prize in physics in the year 1913. Unlike many experimental discoveries in physics, which are a consequence of developed theoretical models, the microscopic and phenomenological theories of superconductivity came long after its discovery [55–57].

The transition from normal metal to the superconducting state happens at the critical temperature, T_c, which varies for different metals. Below this temperature, the electrons in the superconductor pair up to form Cooper pairs. The attractive force that causes this pairing is mediated by the electron interaction with the lattice phonons. The microscopic theory of superconductivity, which explains the nature of the formation of Cooper pairs, is explained by the BCS-theory [55, 56]. Under normal circumstances, the fermionic nature of electrons allows a spin-up electron to pair with a spin-down electron thereby obeying the Pauli's exclusion principle. However, in a superconductor, the bosonic Cooper pairs, condense into a single quantum wavefunction $\Psi = \sqrt{n_c}e^{i\theta}$ where θ is the superconducting phase and n_c is the density of Cooper pairs. The Cooper pairs flow along the superconductor in unison, maintaining a constant phase δ between each pair. The bound state energy of a Cooper pair depends on the superconducting gap, 2Δ, which is the minimum energy required to break them into quasiparticles. Cooper pairs flow without scattering with the lattice phonons, which results in zero resistance at DC. This also explains why superconductors are bad conductors of heat.

Another key feature of superconductivity that distinguishes it from a normal metal is its response to externally applied magnetic fields. A type-1 superconductor, like aluminum, expels magnetic fields from its bulk when it undergoes a superconducting transition. This principle of perfect diamagnetism is explained by the Meissner effect [58]. We will see later on how this effect can be used to our advantage for building magnetic shields useful in superconducting experiments.

2.1.1 Josephson effect

In this section, we will introduce the seminal work of Brian Josephson who investigated the mechanism of tunnelling of Cooper pairs across two superconducting electrodes with a tunnelling barrier between them [59] as shown in Fig. 2.1(a). The two effects he predicted, the DC and the AC Josephson effect, remain as one of the greatest successes of the applicability of superconductivity in present day life. The junction formed by the barrier between the electrodes, popularly known as the Josephson junction (JJ), is ubiquitous in the field of circuit-QED. The JJ used in this thesis is fabricated using aluminum electrodes with a thin barrier of aluminum oxide between them.

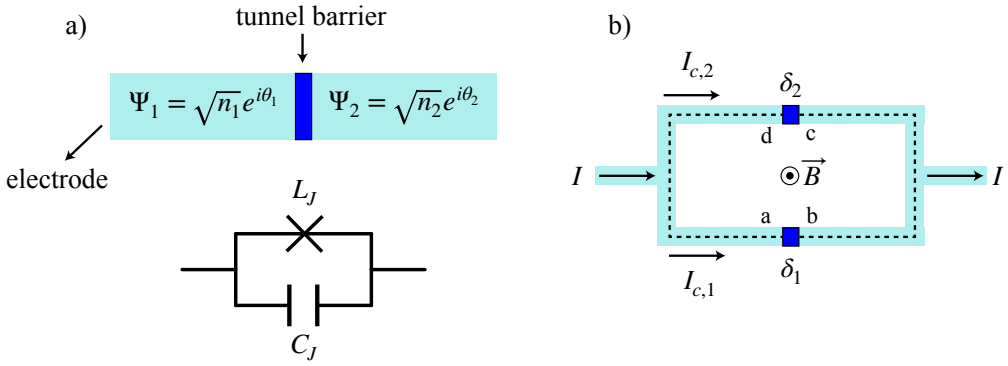

Figure 2.1: (a) Illustration of a Josephson junction formed by a tunnel barrier sandwiched between two superconducting electrodes. Also shown is its equivalent circuit. (b) A pair of Josephson junctions connected in a loop to form a SQUID.

The current, I, across a JJ depends on the phase difference of the Cooper pair wavefunctions, $\delta = \theta_1 - \theta_2$, across the barrier as

$$I = I_c \sin\delta, \tag{2.1}$$

where I_c is the critical current of the junction which is the maximum current that the junction can withstand before it goes to the normal state. Typically, I_c is controlled by the thickness of the tunnelling barrier. The nonlinear current-phase relationship given by Eq. (2.1) is called the DC Josephson effect since a DC current can flow through the junction without a voltage drop across it. A time-varying phase difference, $\delta(t)$, gives rise to a voltage, V, across the junction as

$$V = \frac{\Phi_0}{2\pi}\frac{d\delta}{dt}, \tag{2.2}$$

where $\Phi_0 = h/(2e)$ is the flux quantum. The voltage-phase relation given by Eq. (2.2) is referred to as the AC Josephson effect, as applying a DC voltage across the junction gives rise to an AC current through it. Using Eqs. (2.1) and (2.2), we can derive the expression for the Josephson inductance, L_J as

$$L_J = \frac{\Phi_0}{2\pi}\frac{1}{I_c\cos\delta}. \tag{2.3}$$

It is evident from Eq. (2.3) that L_J is nonlinear due to its dependence on δ. The physical geometry of the JJ also gives rise to a parallel capacitance, C_J, which depends on the

junction area and the oxide dielectric. Due to the small size of the junction, the plasma frequency $f_J = 1/(2\pi\sqrt{L_J C_J})$ is several tens of GHz. Since most superconducting microwave circuits that employ JJs operate at much lower frequencies, typically 4-12 GHz, the JJ behaves as a nonlinear, nondissipative inductor in this frequency regime. To calculate the characteristic energy scale for the junction, typically known as the Josephson energy E_J, consider the work done, ΔE on the junction when the junction phase δ changes over time. This can be calculated using the Josephson relations as,

$$\Delta E = \int IV dt = -\left(\frac{\Phi_0}{2\pi}\right) I_c \cos\delta = -E_J \cos\delta,$$

where $E_J = (\Phi_0/2\pi)I_c$.

2.1.2 DC SQUID

We now introduce the DC superconducting quantum interference device (SQUID), henceforth referred to as SQUID. A SQUID is a closed superconducting loop interrupted by two tunnel barriers in parallel as shown in Fig. 2.1(b). First invented by Ford Research Labs [60], the present day SQUID is one of the most sensitive magnetic field detectors that can be built.

The inductance of the SQUID depends on the total flux Φ threading its loop as shown in Fig. 2.1(b). The gauge-invariant phase difference across the junctions, δ_1 and δ_2, also depends on Φ. Hence, in order to derive the SQUID equations, we have to consider the phase contributions of the junctions and the superconductor around the SQUID loop in response to Φ following the notation shown in Fig. 2.1(b). This can be written as,

$$\oint_C \nabla\theta dl = (\theta_b - \theta_a) + (\theta_c - \theta_b) + (\theta_d - \theta_c) + (\theta_a - \theta_d)\,. \tag{2.4}$$

We can now calculate each of these phase contributions by using the definition for the gauge-invariant phase, δ, for the junctions and the supercurrent equation for the electrodes [61]. For the junctions we have,

$$\theta_b - \theta_a = -\delta_1 - \frac{2\pi}{\Phi_0}\int_a^b \vec{A} dl.$$
$$\theta_d - \theta_c = \delta_2 - \frac{2\pi}{\Phi_0}\int_c^d \vec{A} dl.$$

where A is the electromagnetic vector potential. For the electrode sections we use the supercurrent equation [61] which relates the supercurrent, $\vec{J}_s$, together with $\vec{A}$ and the phase of the Cooper pairs, θ, as,

$$\theta_c - \theta_b = \int_b^c \nabla\theta dl = -\Lambda \int_b^c \vec{J}_s dl - \frac{2\pi}{\Phi_0}\int_b^c \vec{A} dl.$$
$$\theta_a - \theta_d = \int_d^a \nabla\theta dl = -\Lambda \int_d^a \vec{J}_s dl - \frac{2\pi}{\Phi_0}\int_d^a \vec{A} dl.$$

By considering the contour of integration within the bulk of the superconductor where $\vec{J}_s = 0$ and adding the above four equations gives us the total phase difference around the SQUID loop as,

$$\oint_C \nabla\theta dl = \delta_2 - \delta_1 - \frac{2\pi}{\Phi_0}\oint_C \vec{A} dl.$$

To preserve the continuity of phase around the superconducting loop, the total phase must be an integer multiple of 2π. The previous equation now reads,

$$\delta_2 - \delta_1 = 2\pi n + \frac{2\pi}{\Phi_0}\Phi. \tag{2.5}$$

From Fig. 2.1(b), the total current through the SQUID is now,

$$I = I_{c,1}\sin\delta_1 + I_{c,2}\sin\delta_2.$$

By writing $\delta = (\delta_1 + \delta_2)/2$, the above equation can be re-written as,

$$I = I_{c,1}\sin\left(\delta - \pi\left(n + \frac{\Phi}{\Phi_0}\right)\right) + I_{c,2}\sin\left(\delta + \pi\left(n + \frac{\Phi}{\Phi_0}\right)\right).$$

Consider the case when $n = 0$ which simplifies the above equation to,

$$I = (I_{c,1} + I_{c,2})\left(\sin\delta\cos\frac{\pi\Phi}{\Phi_0} + \frac{(I_{c,2} - I_{c,1})}{(I_{c,1} + I_{c,2})}\cos\delta\sin\frac{\pi\Phi}{\Phi_0}\right).$$

Rewriting the sum of critical currents as $I_{c,1}+I_{c,2} = I_c$ and the difference as $I_{c,2}-I_{c,1} = \Delta I_c$ we have,

$$I = I_c\left(\sin\delta\cos\frac{\pi\Phi}{\Phi_0} + \frac{\Delta I_c}{I_c}\cos\delta\sin\frac{\pi\Phi}{\Phi_0}\right). \tag{2.6}$$

Differentiating Eq. (2.6) with respect to time, we obtain an expression for the SQUID inductance as,

$$L_{\rm sq} = \frac{L_{\rm sq}^{\rm max}}{\left(\cos\delta\cos\frac{\pi\Phi}{\Phi_0} - \frac{\Delta I_c}{I_c}\sin\delta\sin\frac{\pi\Phi}{\Phi_0}\right)},$$

where, the linear part of the SQUID's inductance is written as $L_{\rm sq}^{\rm max} = \Phi_0/(2\pi I_c)$. For a symmetric SQUID, the junctions are identical and so $\Delta I_c = 0$ and $I_c \to 2I_c$. We immediately can then see the similarity with that of a single junction as derived in Eq. (2.3) with the exception of the external flux term. Rewriting $L_{\rm sq}$ in terms of I, we get,

$$L_{\rm sq} = \frac{L_{\rm sq}^{\rm max}}{\sqrt{\cos^2 \frac{\pi\Phi}{\Phi_0} - \frac{I^2}{I_c^2}}}.$$

Simplifying the above expression in the limit of $I \ll I_c$, we obtain the inductance for a symmetric SQUID as,

$$L_{\rm sq} = \frac{L_{\rm sq}^{\rm max}}{\left|\cos \frac{\pi\Phi}{\Phi_0}\right|}. \tag{2.7}$$

The SQUID can thus be considered as a flux tunable inductor which forms the crucial building block for all devices presented in this thesis. The tunable Josephson energy, $E_{J,\rm sq}$ is given by,

$$E_{J,\rm sq} = E_{J,\rm sq}^{\rm max}\left|\cos \frac{\pi\Phi}{\Phi_0}\right|, \tag{2.8}$$

where $E_{J,\rm sq}^{\rm max} = (\Phi_0/2\pi)(2I_c)$.

The linear part of the inductance for both single junction and the SQUID depends on the critical current. As mentioned earlier, the critical current I_c for the single junction or the SQUID depends on the thickness of the tunnel barrier. When the junction is fabricated, its room temperature normal state resistance R_n has a direct relation with its critical current. This is given by the Ambegaokar-Baratoff relation [62],

$$I_c = \frac{\pi\Delta}{2eR_n}, \tag{2.9}$$

where $\Delta = 1.76 k_B T_c$ and k_B is the Boltzmann constant. For thin film Al, $\Delta \sim 210$ μeV. By calibrating the oxidation conditions of Al during fabrication, we can target a design specific R_n which will reflect in I_c when the devices are measured.

2.2 Artificial atom: Cooper-pair box

In the previous section, we derived the equation for the Josephson inductance for a single junction and the SQUID using the Josephson relations. In this section, we describe how

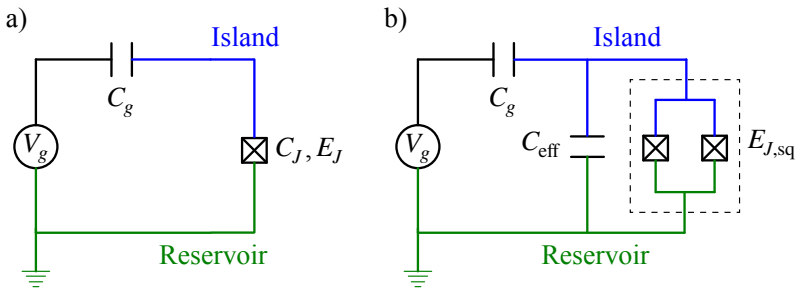

Figure 2.2: Equivalent circuit diagram for (a) the Cooper-pair box and (b) the transmon.

a JJ can be configured to be used an an artificial atom by utilizing the nonlinearity that it inherently possess. We will introduce the Hamiltonian of such a circuit based on the theoretical work that is presented in [34]. By diagonalizing the Hamiltonian in the chosen basis, we show the eigenenergies for the multiple transitions of the artificial atom thus formed.

Superconducting qubits can be constructed in multiple ways depending on the mechanism of control of the qubit states. The most popular being the charge qubit, the flux qubit and the phase qubit. A review of these qubits can be found in [9]. Here, we focus on the charge qubit which is based on the Cooper-pair box (CPB) [63–65] and an extension of the CPB, the transmon qubit [34]. The artificial atoms studied in this thesis employ the transmon design.

A Cooper-pair box is an electrical circuit that consists of a superconducting island which connects to a grounded superconducting reservoir via a JJ as shown in Fig. 2.2(a). Cooper pairs can tunnel to and from the island into the reservoir which is controlled by two dominant energy scales, the charging energy E_c and the Josephson energy E_J. The total capacitance of the island, $C_\Sigma = C_g + C_J$ determines $E_c = (2e)^2/2C_\Sigma$, which is the amount of energy needed to transfer a Cooper pair into the island. The gate voltage V_g determines the offset gate charge $n_g = C_g V_g/2e$, in the reduced form, on the island which can be modified by V_g. The Josephson energy E_j (defined earlier for a JJ) determines the coupling of the Cooper pairs between the island and the reservoir. To have a tunable E_J, the single junction shown in Fig. 2.2(a), can be replaced by a SQUID where $E_{J,\text{sq}}$ can be tuned by the external flux Φ.

We now introduce the Hamiltonian of the Cooper-pair box in the charge (number) basis following the discussion presented in [34, 65]. If the operator $\hat{n}$ indicates the number of excess Cooper pairs in the island, the total Hamiltonian including the contributions from

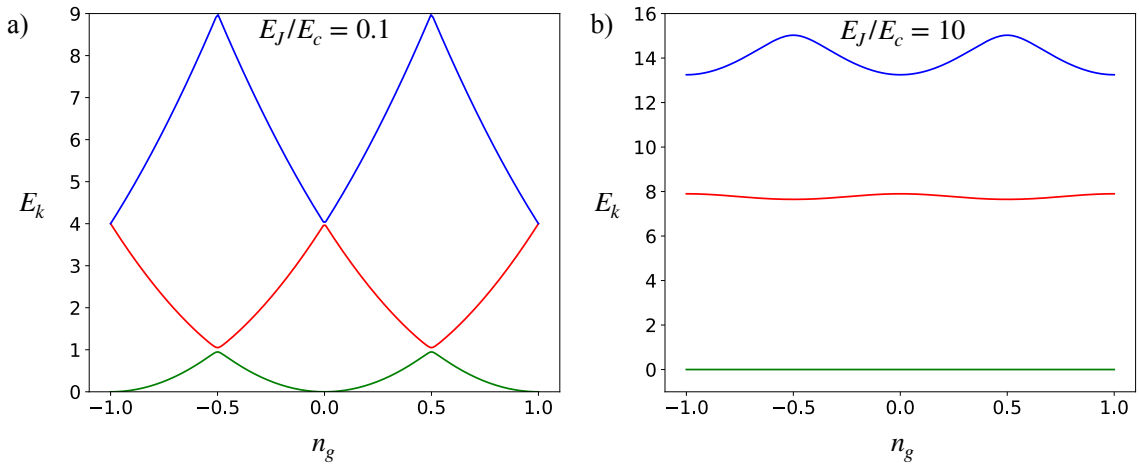

Figure 2.3: Energy spectrum vs. the offset gate charge for the Cooper-pair box when (a) $E_J/E_c = 0.1$ and (b) $E_J/E_c = 10$.

E_c and E_J can be written as,

$$\hat{H}_{\text{CPB}} = 4E_c \sum_{n=-\infty}^{\infty} (\hat{n} - n_g)^2 \, |n\rangle \langle n| - \frac{E_J}{2} \sum_{n=-\infty}^{\infty} (|n+1\rangle \langle n| + |n\rangle \langle n+1|). \tag{2.10}$$

The discrete energy spectrum E_k of state $|k\rangle$ can be written in terms of $\hat{H}_{\text{CPB}}$, which is continuous in n_g, as,

$$\hat{H}_{\text{CPB}} \, |k\rangle = E_k \, |k\rangle \tag{2.11}$$

where, $|k\rangle$ are the eigenstates of the CPB and E_k, the eigenenergies, which can be solved by diagonalizing $\hat{H}_{\text{CPB}}$ in a truncated space for $\hat{n}$. The CPB operates in a regime where $E_c > E_J$ where the qubit state is mostly governed by the charging energy of the gate capacitance. We plot the energy spectrum for the first three levels of the CPB in Fig. 2.3(a) for $E_J/E_c = 0.1$. The transition energy of the different levels can be tuned by the offset charge n_g. The sweet spot for operating the CPB is at odd-integer multiples of $n_g = 0.5$. At these bias points, the ground state and the first excited state of the CPB hybridize to form an avoided-level crossing where the separation depends on E_J. Since the difference in energies between the first and the second excited state is much greater than that of the ground and the first excited state, the lowest two energy levels can be selectively addressed without populating the higher levels. This difference in energies is frequently referred to as the anharmonicity. The CPB operating at the sweet spot in the low E_J/E_c regime does

well as a two-level system due to its large anharmonicity. However, the price one pays is at the cost of charge noise as small changes in n_g can result in large qubit frequency fluctuations.

2.2.1 Transmon regime

To overcome sensitivity of the CPB to charge noise, a large shunt capacitance C_{eff} is added across the junction which increases the overall capacitance C_Σ of the island, i.e, $C_\Sigma = C_g + C_J + C_{\text{eff}}$ as shown in Fig. 2.2(b). The single junction is replaced by a SQUID which allows for the tuning of $E_{J,\text{sq}}$. The reduction of E_c makes the ratio E_J/E_c large. The CPB operating in the regime where $E_J \gg E_c$ is more popularly known as the transmon qubit [34]. The large E_J/E_c causes an exponential suppression in the charge dispersion resulting in an energy profile which is more flat [34]. This helps to reduce the sensitivity of the transmon to charge noise with a wide operating range for n_g. However, this comes at a price of reduced anharmonicity between the energy levels. The $|0\rangle - |1\rangle$ transition frequency, ω_{10} can be written as [34],

$$\omega_{10} = (\sqrt{8E_{J,\text{sq}}E_c} - E_c)/\hbar. \tag{2.12}$$

The anharmonicity between the first two transitions is given by [34],

$$|\omega_{21} - \omega_{10}| = E_c/\hbar. \tag{2.13}$$

2.3 Microwave transmission-line theory

The goal of this section is to introduce the theory of a microwave TL as a starting point for analyzing circuits that are studied in this thesis. Typically, the characteristic length of a TL is a significant fraction of the wavelength or even several wavelengths. As a result, the voltage $V(x,t)$ and the current $I(x,t)$ in a TL will vary in both magnitude and phase along its length.

To study this behavior we use the transmission line theory, where the TL is modelled as a two-wire conductor in order to sustain a transverse electromagnetic mode (TEM). Following the standard procedure prescribed in [66], we can derive the equations for $V(x,t)$ and $I(x,t)$ by considering the lumped-element model for an infinitesimal section Δx of the TL as shown in Fig. 2.4, where R_0 is the series resistance for both conductors, L_0 is the self-inductance between the conductors, G_0 is the conductance between the conductors

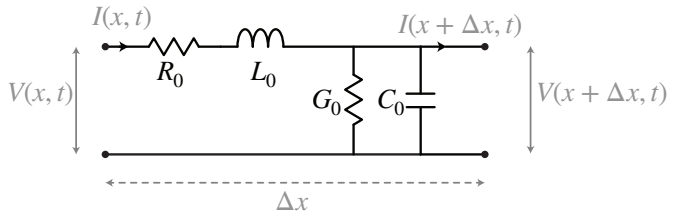

Figure 2.4: Lumped-element equivalent circuit model of a transmission line (TL).

facilitated by the dielectric and C_0 is the capacitance between the conductors. All these parameters are defined per unit length of the two conductors. The currents and voltages are defined at the input and the output of the conductors as shown in Fig. 2.4. Using Kirchhoff's laws, we can write,

$$V(x+\Delta x,t)-V(x,t)=-\left(L_0\Delta x\frac{dI(x,t)}{dt}+R_0\Delta x I(x,t)\right).$$
$$I(x+\Delta x,t)-I(x,t)=-\left(C_0\Delta x\frac{dV(x+\Delta x,t)}{dt}+G_0\Delta x V(x+\Delta x,t)\right).$$

Dividing the above equations with Δx and taking the limit, $\Delta x \to 0$, we can obtain the Telegrapher equations as,

$$\frac{dV(x,t)}{dt}=-\left(L_0\frac{dI(x,t)}{dt}+R_0 I(x,t)\right).$$
$$\frac{dI(x,t)}{dt}=-\left(C_0\frac{dV(x,t)}{dt}+G_0 V(x,t)\right).$$

For sinusoidal time-varying voltage and current phasors, at steady state, the Telegrapher equations reduces to the wave equations which can be written as,

$$\begin{aligned}\frac{d^2V(x)}{dx^2}-\gamma^2V(x)=0\\ \frac{d^2I(x)}{dx^2}-\gamma^2I(x)=0\end{aligned}\tag{2.14}$$

where $\gamma=\alpha+i\beta=\sqrt{(R_0+i\omega L_0)(G_0+i\omega C_0)}$ is the complex propagation constant, α is the attenuation constant and β is the phase constant of the TL. The solutions for Eq. (2.14) can be written in terms of forward (denoted by superscript +) and backward (denoted by

superscript $-$) propagating voltages and currents as,

$$\begin{aligned} V(x) &= V^+ e^{-\gamma x} + V^- e^{\gamma x} \\ I(x) &= I^+ e^{-\gamma x} + I^- e^{\gamma x} \end{aligned} \tag{2.15}$$

where $I^+ = V^+/Z_0$ and $I^- = -V^-/Z_0$ and $Z_0 = \sqrt{(R_0 + i\omega L_0)/(G_0 + i\omega C_0)}$ is the characteristic impedance of the TL. Using Eq. (2.15), we can write the expressions for $V(x,t) = Re[V(x)e^{i\omega t}]$ and $I(x,t) = Re[I(x)e^{i\omega t}]$ as,

$$\begin{aligned} V(x,t) &= V^+ \cos(\omega t - \beta x)e^{-\alpha x} + V^- \cos(\omega t + \beta x)e^{\alpha x} \\ I(x,t) &= \frac{V^+}{Z_0} \cos\big(\omega t - \beta x + \phi^+\big)e^{-\alpha x} - \frac{V^-}{Z_0} \cos\big(\omega t + \beta x + \phi^-\big)e^{\alpha x} \end{aligned} \tag{2.16}$$

where, $\phi^\pm$ is the phase angle of the complex current $I^\pm$ with respect to $V^\pm$.

Coplanar Waveguide (CPW)

For the devices that are presented in this thesis, the architecture of choice to implement a TL is the finite-ground coplanar waveguide (CPW) [67], which is shown pictorially in Fig. 2.5. It consists of a central conductor, the signal line of width W and ground plane conductors on either side separated by a gap S from the signal line. The metal is patterned on the substrate of height H which has a relative dielectric constant ϵ_r. The CPW architecture has many advantages over other conventional TL architectures. The circuit is planar and can be fabricated using standard micro fabrication techniques with relative ease. The characteristic impedance Z_0^{CPW} of the CPW TL depends solely on the circuit geometry and is given by [67],

$$Z_0^{\text{CPW}} = \frac{30\pi}{\sqrt{\epsilon_{\text{eff}}}} \frac{K(k_0')}{K(k_0)} \tag{2.17}$$

where $K(k_0)$ and $K(k_0')$ are the complete elliptic integrals of the first kind where $k_0 = W/(W+2S)$ and $k_0' = \sqrt{1-k_0^2}$. The inductance L_0 and capacitance C_0 per unit unit length of the CPW TL is given by [67],

$$\begin{aligned} L_0 &= \frac{\mu_0}{4} \frac{K(k_0')}{K(k_0)} \\ C_0 &= 4\epsilon_0 \epsilon_{\text{eff}} \frac{K(k_0)}{K(k_0')}, \end{aligned} \tag{2.18}$$

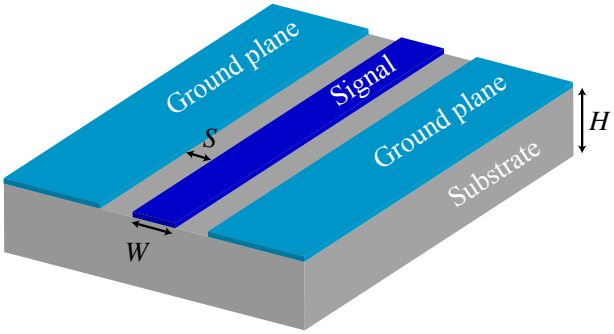

Figure 2.5: Coplanar waveguide architecture of a transmission line formed by a central conductor of width W, equally separated from ground planes on both sides by a gap S, on top of a substrate of height H.

where, μ_0 and ϵ_0 are the permeability and permittivity of free space satisfying $c = 1/\sqrt{\mu_0\epsilon_0}$ and $\epsilon_{\text{eff}} = (1+\epsilon_r)/2$. For a typical superconducting circuit, the conductors are formed using a superconducting metal with thickness $t \ll W, S$ and the substrate height $H \gg W, S$. Due to the substrate dielectric, the phase velocity of the waves in a CPW TL, $v = c/\epsilon_{\text{eff}} = 1/\sqrt{L_0 C_0}$.

2.3.1 Lossless transmission line terminated by a load

As mentioned before, the advantage of working with superconducting circuits is that the TL can be approximated to be lossless. We will now simply the equations presented earlier under the lossless approximation. For a lossless TL, $R_0 = G_0 = 0$ and hence $Z_0 = \sqrt{L_0/C_0}$. The complex propagation constant $\gamma = i\beta$ and $\beta = \omega/v = \omega\sqrt{L_0 C_0}$ and the wavelength $\lambda = 2\pi v/\omega$. We will now consider a lossless TL which is terminated by an arbitrary load impedance Z_L as shown in Fig. 2.6.

Using Eq. (2.15), Z_L can be written as,

$$Z_L = \frac{V(0)}{I(0)} = \left(\frac{V^+ + V^-}{V^+ - V^-}\right) Z_0$$

By defining the reflection coefficient $\Gamma = V^-/V^+$, the above equations can be re-written as,

$$\Gamma = \frac{Z_L - Z_0}{Z_L + Z_0} \tag{2.19}$$

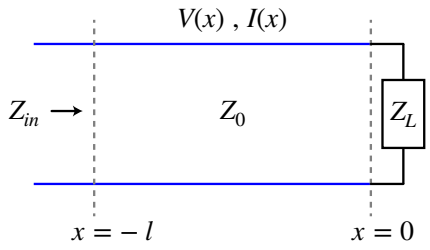

Figure 2.6: A lossless transmission line terminated by an arbitrary load impedance.

Using Eqs. (2.15) and (2.19) , we can write an expression for the input impedance Z_{in} of the TL as seen from a point $x = -l$ into the direction of the load as,

$$Z_{in} = \left(\frac{V^+ e^{i\beta l} + \Gamma V^+ e^{-i\beta l}}{V^+ e^{i\beta l} - \Gamma V^+ e^{-i\beta l}} \right) Z_0$$

Simplifying the above expression, we obtain,

$$Z_{in} = \left(\frac{Z_L + iZ_0 \tan \beta l}{Z_0 + iZ_L \tan \beta l} \right) Z_0 \tag{2.20}$$

Eq. (2.20) forms the starting point for deriving equations for TL resonators which are discussed in this thesis.

2.3.2 Capacitively coupled $\lambda/4$ (quarter-wave) resonator

Microwave resonators can be constructed in a variety of ways [66]. Here, we will focus on TL-based resonators with specific boundary conditions which behave as resonators. In particular, we consider a lossless TL of a finite length l which is short-circuited to ground on one end and an open-circuit boundary on the other end. The grounded boundary condition implements a voltage-node and the open-circuit condition creates a voltage-antinode. This will result in standing waves corresponding to a wavelength $\lambda = 4l/n$, where n is an odd integer which represents the mode number. The circuit will resonate at frequencies $f_n = nv/4l$. For our purposes, we are interested only in the fundamental mode. The circuit is shown in Fig. 2.7(a).

We begin by considering the input impedance of a shorted TL of length $l = \lambda/4$ without the effect of the coupling capacitor C_c. Using Eq. (2.20) we can write this down as,

$$Z_{in}^{\lambda/4} = jZ_0 \tan(\beta l) . \tag{2.21}$$

We can now look at the behavior of this circuit near its resonance frequency by writing βl as,

$$\beta l = \frac{\omega_0 l}{v_p} + \frac{\Delta\omega l}{v_p},$$

where, ω_0 is the fundamental resonance frequency for the $\lambda/4$ resonator and $\Delta\omega = \omega - \omega_0$ is the detuning from ω_0. Using the fact that $l = \lambda/4$ and $v = (\omega_0\lambda)/2\pi$, we can reduce Eq.(2.21) to,

$$Z_{in}^{\lambda/4} \approx \frac{-i2Z_0\omega_0}{\pi\Delta\omega} \tag{2.22}$$

Consider the input impedance of a parallel lumped-element LC circuit near its resonance frequency which can be derived as,

$$Z_{in}^{LC} = \frac{-j}{2C\Delta\omega}. \tag{2.23}$$

Comparing Eq. (2.22) and Eq. (2.23), one can see the similarity in behavior of the short circuited $\lambda/4$ resonator as a parallel LC circuit near ω_0 with the following lumped parameters:

$$L = \frac{4Z_0}{\pi\omega_0} \quad ; \quad C = \frac{\pi}{4Z_0\omega_0} \tag{2.24}$$

For the case when $\alpha \neq 0$, it can be shown that the loss can be lumped into the parallel resistor $R = Z_0/(\alpha l)$ [66].

The coupling capacitor C_c couples the $\lambda/4$ resonator to the external environment via a feedline of impedance Z_0 as shown in Fig. 2.7(a) as well as in its equivalent lumped-element model in Fig. 2.7(b). The task now is to calculate the overall impedance $Z_{\lambda/4}$ of the resonator in presence of C_c. This is done by transforming the series circuit formed by the elements Z_0 and C_c into an effective parallel circuit comprising of Z_0' and C_c' (see Fig. 2.7(c)) and equating the real and imaginary parts of the series and parallel circuit respectively as,

$$Z_0 = \frac{Z_0'}{1 + \omega^2 C_c'^2 Z_0'^2} \quad ; \quad C_c = \frac{1 + \omega^2 C_c'^2 Z_0'^2}{\omega^2 C_c' Z_0'^2} \tag{2.25}$$

The above equations can be further simplified by making the quality factors of the series and parallel circuit to be the same, i,e, $1/(\omega C_c Z_0) = \omega C_c' Z_0'$. This is done to ensure that the series circuit behavior is the same as the transformed parallel circuit when connected to an external resonant circuit. With this, Eq. (2.25) can be further simplified to give,

$$Z_0' = Z_0 \frac{1 + \omega^2 C_c^2 Z_0^2}{\omega^2 C_c^2 Z_0^2} \quad ; \quad C_c' = \frac{C_c}{1 + \omega^2 C_c^2 Z_0^2} \tag{2.26}$$

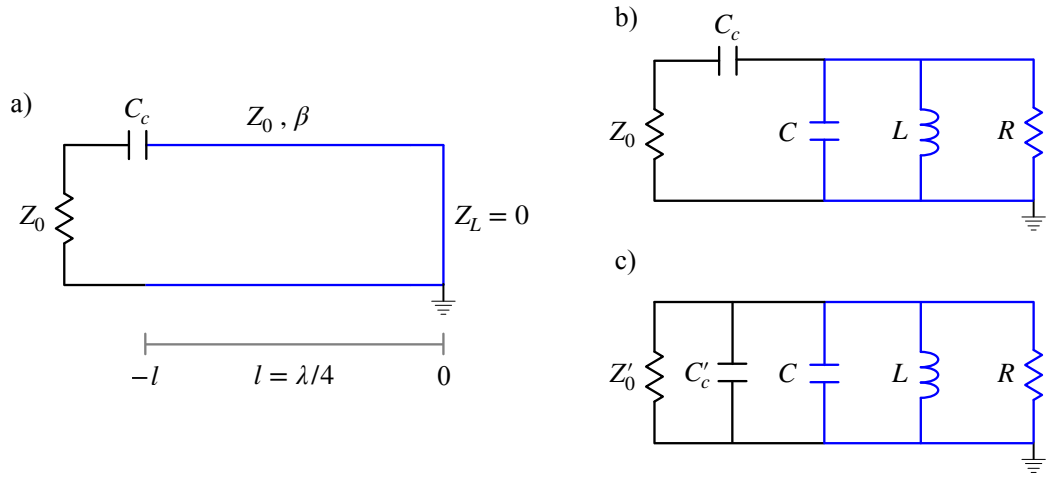

Figure 2.7: (a) Model of a capacitively-coupled quarter-wave resonator. (b) Equivalent circuit of the model shown in (a) where the shorted TL is replaced by a parallel LC circuit. (c) Redrawing the circuit in (b) after a series to parallel circuit transformation.

The circuit representation in Fig. 2.7(c), offers a simplified platform to extract the internal, Q_{int}, and external, Q_{ext}, quality factors of the resonant circuit coupled to its environment. The quality factor is a measure of loss in the circuit. For superconducting resonators, the internal loss in the circuit, typically occurs due to dielectric loss or due to two level systems (TLS) among many others [68,69]. This internal loss, although negligible, can then be lumped into R. Resonators with $Q_{\text{int}} > 1,000,000$ have been demonstrated using superconducting circuits using improved fabrication techniques [70]. Another channel of loss is represented by the resonator's coupling to its environment which in Fig. 2.7(c) is due to the transformed Z_0'. By varying C_c, we can control the amount of energy that can be injected into the resonator which also sets the rate at which energy leaks out of the system. The total loss is then set by Q_{tot} which can be written as,

$$\frac{1}{Q_{\text{tot}}} = \frac{1}{Q_{\text{int}}} + \frac{1}{Q_{\text{ext}}} \tag{2.27}$$

Using the expressions for quality factor for parallel RLC circuits from [66], Q_{int} and Q_{ext}

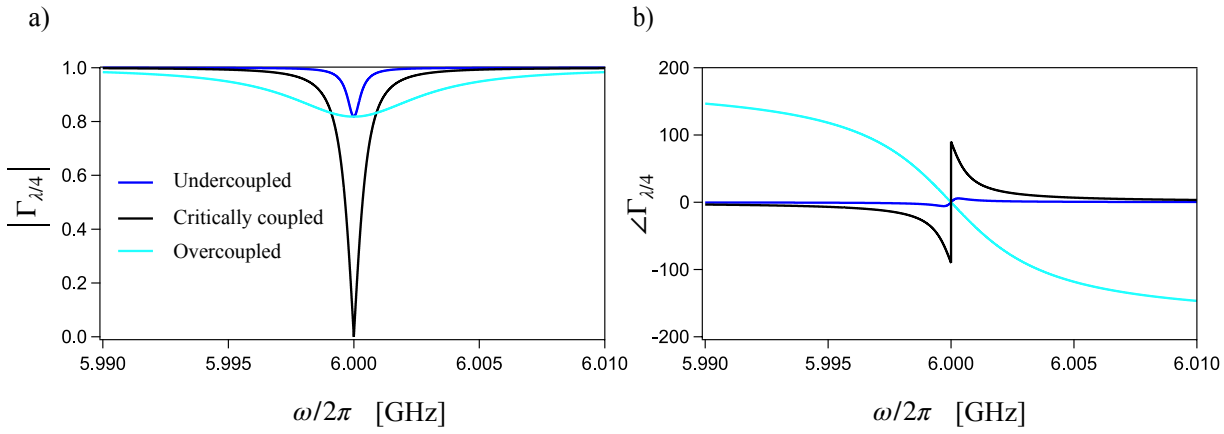

Figure 2.8: (a) Magnitude and (b) phase of the reflection coefficient for a capacitively-coupled quarterwave resonator in the under-coupled, critically-coupled and over-coupled regimes.

for the circuit shown in Fig. 2.7(c) can be worked out as,

$$\begin{aligned} Q_{\text{int}} &= \omega_0 R \left(C + \frac{C_c}{1 + \omega_0^2 C_c^2 Z_0^2} \right) \\ Q_{\text{ext}} &= \frac{1}{\omega_0 C_c^2 Z_0} \left(C(1 + \omega_0^2 C_c^2 Z_0^2) + C_c \right) \end{aligned} \tag{2.28}$$

where, $\omega_0 = 1/\sqrt{L(C + C_c')}$. Under experimental conditions, $(\omega_0 C_c Z_0)^2 \ll 1$ and so the above expressions for Q_{int} and Q_{ext} reduce to,

$$Q_{\text{int}} = \omega_0 R(C + C_c) \qquad ; \qquad Q_{\text{ext}} = \frac{C + C_c}{\omega_0 C_c^2 Z_0} \tag{2.29}$$

Since all the elements in Fig. 2.7(c) are in parallel, we can now write an expression for admittance $Y_{\lambda/4} = 1/Z_{\lambda/4}$ as,

$$Y_{\lambda/4} = \frac{1}{R} + \frac{1}{i\omega L} + i\omega(C + C_c').$$

After some algebraic manipulations, the impedance of the $\lambda/4$ resonator can be written as,

$$Z_{\lambda/4} = \left(\frac{1}{R} + i2\Delta\omega(C + C_c') \right)^{-1}. \tag{2.30}$$

The reflection coefficient $\Gamma_{\lambda/4}$ of the resonator with respect to Z_0' can be calculated using,

$$\Gamma_{\lambda/4} = \frac{Z_{\lambda/4} - Z_0'}{Z_{\lambda/4} + Z_0'}.$$

From the definitions of Q_{int} and Q_{ext} given by Eq. (2.29), a simplified equation for $\Gamma_{\lambda/4}$ can be evaluated as,

$$\Gamma_{\lambda/4} = \frac{\frac{1}{Q_{\text{ext}}} - \frac{1}{Q_{\text{int}}} - i2\frac{\Delta\omega}{\omega_0}}{\frac{1}{Q_{\text{ext}}} + \frac{1}{Q_{\text{int}}} + i2\frac{\Delta\omega}{\omega_0}} \tag{2.31}$$

The total quality factor of the circuit, Q_{tot}, depends on the participation of Q_{ext} and Q_{int}. Depending on the value of C_c, the resonator can be either undercoupled ($Q_{\text{tot}} \sim Q_{\text{int}}$), critically coupled ($Q_{\text{ext}} = Q_{\text{int}}$) or overcoupled ($Q_{\text{tot}} \sim Q_{\text{ext}}$). Typically, resonators are designed to be in the over-coupled regime of operation, as the total loss mostly depends on the coupling to the environment which is under the control of the experimenter. Figure 2.8 shows the magnitude, $\left|\Gamma_{\lambda/4}\right|$, and phase, $\angle\Gamma_{\lambda/4}$ using Eq. (2.31) for three different coupling regimes at a fixed Q_{int} and varying Q_{ext}.

2.3.3 Frequency tunable $\lambda/4$ resonator

The previous section introduced the basic operation of a short-circuited $\lambda/4$ cavity. The equations were derived with the load impedance $Z_L = 0$. In this section, we present a frequency tunable $\lambda/4$ resonator for a non-zero Z_L which is introduced by the impedance of a SQUID. For a symmetric-SQUID terminated $\lambda/4$ resonator, $Z_L = Z_{\text{sq}}$ is modified by

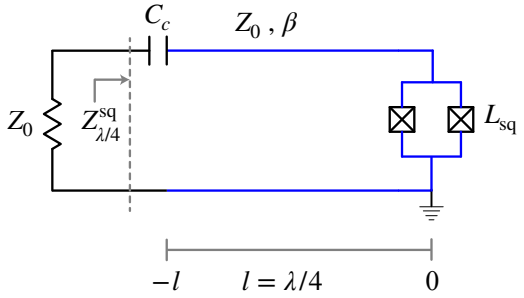

Figure 2.9: Model of a capacitively-coupled, SQUID terminated quarter-wave resonator

the flux-tunable inductance $L_{\rm sq}$ of the SQUID (see Eq. (2.7)) as,

$$Z_{\rm sq} = i\omega L_{\rm sq} = \omega \frac{\Phi_0}{2\pi(2I_c)\left|\cos\frac{\pi\Phi}{\Phi_0}\right|} \tag{2.32}$$

where, I_c is the maximum critical current of each junction. From Fig. 2.9, the total impedance, $Z^{\rm sq}_{\lambda/4}$, of a lossless TL of length $l = \lambda/4$ and characteristic impedance Z_0, coupled to its environment by a coupling capacitor C_c on one end and terminated by a SQUID on the other is given by,

$$Z^{\rm sq}_{\lambda/4} = \frac{1}{i\omega C_c} + Z_0 \frac{Z_{\rm sq} + iZ_0 \tan\beta l}{Z_0 + iZ_{\rm sq}\tan\beta l} \tag{2.33}$$

The reflection coefficient $\Gamma^{\rm sq}_{\lambda/4}$ can then be written as,

$$\Gamma^{\rm sq}_{\lambda/4} = \frac{Z^{\rm sq}_{\lambda/4} - Z_0}{Z^{\rm sq}_{\lambda/4} + Z_0}. \tag{2.34}$$

We can solve Eq. (2.34) numerically by choosing appropriate values for C_c, I_c and l. The value of $Z_0 = 50\ \Omega$, unless specified otherwise. Figure 2.10 shows the frequency tunability of an extremely overcoupled $\lambda/4$ resonator as a function of Φ/Φ_0, a design that is experimentally motivated which is discussed in Chapter 7. The color represents the phase of the reflection coefficient, $\angle\Gamma^{\rm sq}_{\lambda/4}$. To obtain the plot in Fig. 2.10, we use $I_c = 0.325\ \mu$A, $l = 3.75$ mm, $C_c = 150$ fF and $Z_0 = 50\ \Omega$.

2.3.4 Capacitively-coupled $\lambda/2$ resonator

In this section, we present a simple analysis for a two port network which comprises a TL of length $l = \lambda/2$, coupled to its environment using input and output coupling capacitors C_c as shown in Fig. 2.11(a). The circuit thus formed is a half-wave resonator which is another class of TL based resonators discussed in this thesis. Two-port networks, such as the circuit shown in Fig. 2.11(a), can be analyzed using the transmission ($ABCD$) matrix method [66]. Each component of the circuit is represented by a two-port $ABCD$ matrix and when multiple components are cascaded together, the $ABCD$ matrix of the full circuit is obtained by simply multiplying the individual matrices.

In the circuit shown in Fig. 2.11(a), the three components correspond to the input and output coupling capacitors together with the TL line of length $\lambda/2$. In general, the $ABCD$

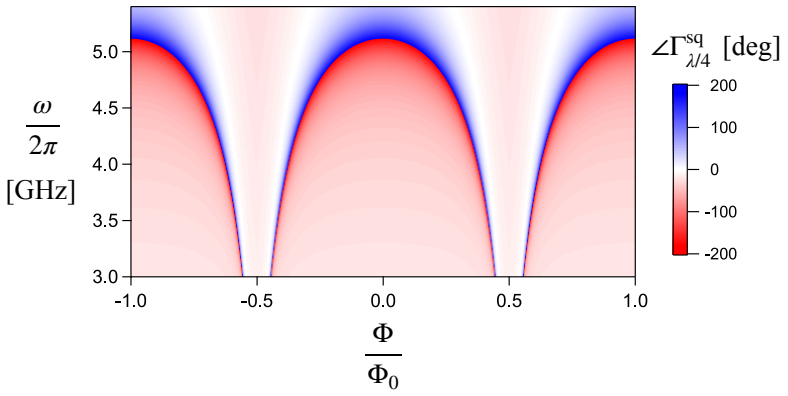

Figure 2.10: Frequency tunability of a capacitively-coupled, SQUID terminated $\lambda/4$ resonator where the color shows $\angle\Gamma^{sq}_{\lambda/4}$ for different flux bias conditions.

matrix M for a two-port network is written as,

$$M = \begin{bmatrix} A & B \\ C & D \end{bmatrix}$$

where the elements of the matrix correspond to A, B, C and D. Depending on the component, the matrix elements differ. The $ABCD$ matrices for a capacitor C_c and the TL can be written as [66],

$$M_{C_c} = \begin{bmatrix} 1 & \frac{1}{i\omega C_c} \\ 0 & 1 \end{bmatrix} \quad ; \quad M_{\mathrm{TL}} = \begin{bmatrix} \cos\beta l & iZ_0 \sin\beta l \\ \frac{i}{Z_0}\sin\beta l & \cos\beta l \end{bmatrix} \tag{2.35}$$

The overall matrix $M_{\lambda/2} = M_{C_c}.M_{\mathrm{TL}}.M_{C_c}$ can be evaluated which gives us the new matrix elements A, B, C and D for the capacitively-coupled $\lambda/2$ resonator. Using the $ABCD$ parameters, the S-parameters can be calculated using the conversion table given in [66]. The transmission coefficient, or S_{21}, can be written down as,

$$S_{21} = \frac{2}{A + \frac{B}{Z_0} + CZ_0 + D} \tag{2.36}$$

By numerically solving for the different matrix elements using appropriate values for $l = \lambda/2$ and C_c, we can obtain S_{21}. Figure 2.11(b) shows the $|S_{21}|$ obtained using $l = 178$ mm and $C_c = 130$ fF, both of which are experimentally motivated. As expected, we see the fundamental mode of the $\lambda/2$ resonator at $f_{\lambda/2} = 329$ MHz.

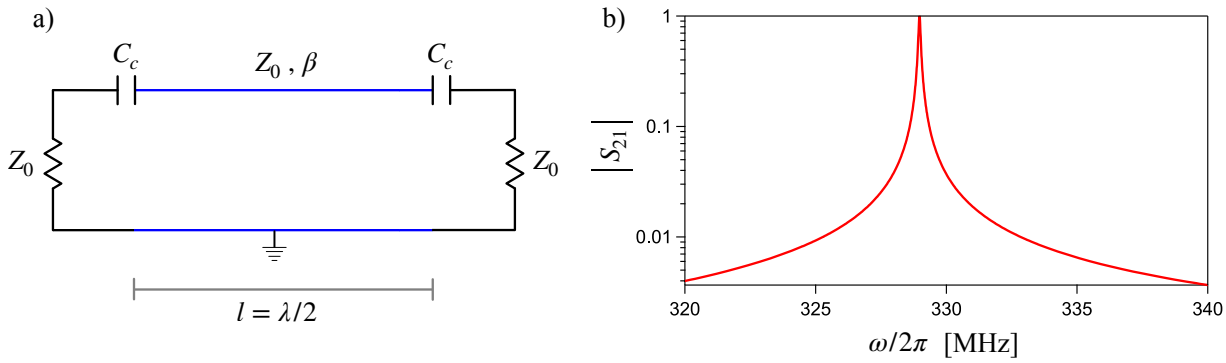

Figure 2.11: (a) Model of a capacitively-coupled lossless $\lambda/2$ resonator. (b) $|S_{21}|$ calculated numerically using the $ABCD$ matrix method.

The actual implementation of the $\lambda/2$ resonator in this thesis follows a novel stepped-impedance design of the TL which is motivated and discussed in Chapter 3. The result shown in Fig. 2.11(b) assumes that $Z_0 = 50\ \Omega$ for the entire resonator's length. However, we note that the $ABCD$ matrix method can be adopted to simulate the stepped-impedance design of the TL relatively easily.

2.4 Artificial atom coupled to a transmission line

We now introduce a transmon which is capacitively coupled to a TL. The network is shown in Fig. 2.12(a), where the transmon is replaced by its equivalent circuit, which is described earlier. A simplified version of this circuit showing the relevant impedances is shown in Fig. 2.12(b). This circuit forms the basis of many experimental studies where the qubit is coupled to a continuum of vacuum modes of the TL [14, 16, 17, 19, 21]. To analyze such a circuit, we approximate the transmon qubit as a classical harmonic oscillator. Although a harmonic oscillator has infinite, equally-spaced energy levels, it can be treated as an effective two-level system under the approximation that the incident field in the TL is weak enough to only excite the $|0\rangle - |1\rangle$ transition of the qubit.

2.4.1 Classical scattering model

At the coupling point, the characteristic impedance Z_0 of the TL is interrupted by the transmon's impedance, which causes the incoming field to scatter resulting in reflection.

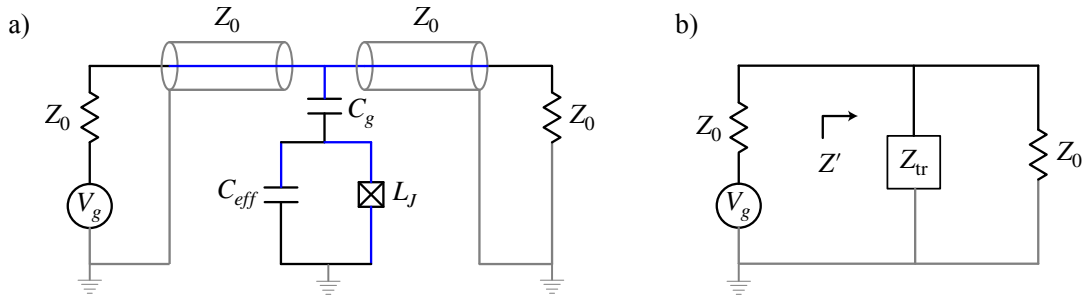

Figure 2.12: (a) Equivalent circuit of a transmon qubit capacitively coupled to a TL. (b) Rewriting the circuit in (a) in terms of the transmon impedance.

Following the procedure outlined in [71], we are interested in deriving the reflection coefficient, r, and the transmission coefficient, t, of the two-port network shown in Fig. 2.12(b). The transmon impedance, $Z_{\rm tr}$ is given by,

$$Z_{\rm tr} = \frac{1}{i\omega C_g} + \left(i\omega C_{\rm eff} + \frac{1}{i\omega L_J}\right)^{-1}$$

The impedance Z' seen from the left of the coupling point as shown in Fig. 2.12(b) can be written as,

$$Z' = \frac{Z_{\rm tr} Z_0}{Z_{\rm tr} + Z_0}$$

Using the above impedances, r can be calculated as,

$$r = \frac{Z' - Z_0}{Z' + Z_0} = \frac{\omega C_g Z_0 (1 - L_J C_{\rm eff}\omega^2)}{-\omega C_g Z_0 (1 - L_J C_{\rm eff}\omega^2) + i2\left(1 - \frac{\omega^2}{\omega_0^2}\right)}. \tag{2.37}$$

Near the resonance frequency $\omega_0 = 1/\sqrt{L_J(C_g + C_{\rm eff})}$, we can write $\omega = \omega_0 + \delta\omega$. After some algebraic manipulations, r can be approximated near ω_0 as,

$$r \simeq \frac{-1}{1 + \dfrac{i\delta\omega}{\Gamma}}. \tag{2.38}$$

where $\Gamma = \omega_0^2 C_g^2 Z_0/(4(C_g + C_{\rm eff}))$ is the relation rate of the qubit into the TL. Using the $ABCD$ matrix for a shunt impedance across a TL (see Fig. 2.12(a)), it can be shown that $t = 1 + r$ [66]. Figure 2.13 shows $|r|$ and $|t|$ as a function of ω for $C_g = 10$ fF, $C_{\rm eff} = 30$ fF,

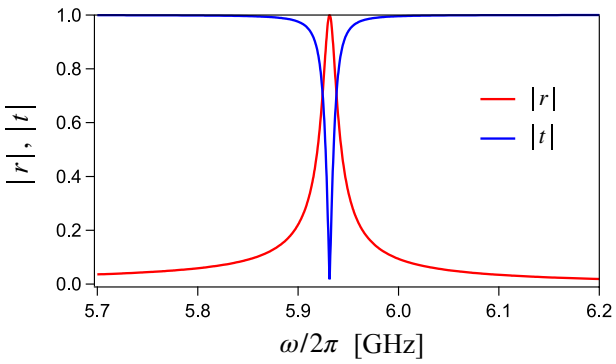

Figure 2.13: Magnitude of reflection $|r|$ and transmission coefficient $|t|$ for a transmon coupled to a transmission line using a classical model

$L_J = 18$ nH and $Z_0 = 50\ \Omega$. Similar results (not shown here) were obtained by using the $ABCD$ matrix method to obtain the S11 and S21 scattering parameters for the network shown in Fig. 2.12(b).

The quantum model for an artificial atom coupled to 1D vacuum can been derived using a master equation solution and is discussed in [13, 71]. The transmission coefficient t for the $|0\rangle - |1\rangle$ transition can be written as,

$$t = 1 - r_0 \frac{1 - \mathrm{i}\delta\omega_\mathrm{p}/\gamma_{10}}{1 + (\delta\omega_\mathrm{p}/\gamma_{10})^2 + \Omega_\mathrm{p}^2/(\Gamma_{10}\gamma_{10})}, \tag{2.39}$$

where $\delta\omega_\mathrm{p}$ is the probe frequency detuning from ω_{10}, Γ_ϕ is the dephasing rate (sum of pure dephasing and non-radiative decay), $\gamma_{10} = \Gamma_{10}/2 + \Gamma_\phi$ is the total decoherence rate, $r_0 = \Gamma_{10}/2\gamma_{10}$, and Ω_p is the probe Rabi frequency which is proportional to the probe amplitude.

2.5 Giant artificial atoms

The transmon qubit, discussed earlier, has been very successful in its applicability in circuit QED, paving the way for many seminal demonstrations of light-matter interactions and quantum computation protocols [9]. Its versatility so far has been limited by the ladder structure of its transition levels which imposes a strict condition on their relaxation

(coupling) rates [72], i.e,

$$\Gamma_{n+1,n} = (n+1)\Gamma_{1,0}, \tag{2.40}$$

where, $\Gamma_{j,i}$ is the relaxation rate of the $|i\rangle - |j\rangle$ transition. As a result, the relaxation rates of its many transitions are fixed by design irrespective of the transmon's operating frequency. To circumvent this limitation, a new design was first proposed by Kockum et al [27], where an ordinary transmon qubit can be engineered to behave as a giant artificial atom by coupling the transmon to propagating photons of a 1D TL at multiple points, which are spatially separated by an order of wavelength λ. As the photons travel, they pick up a phase ϕ between the coupling points which causes the emission/absorption amplitudes of the giant transmon to interfere, resulting in a frequency-dependent coupling of its transition levels, an effect which is not observed in an ordinary transmon. By suitably engineering the anharmonicity of the qubit, the coupling rate of the $|1\rangle - |2\rangle$ transition can be modulated relative to the $|0\rangle - |1\rangle$ transition, adding a new flavour to the existing transmon toolbox. This feature of the giant transmon enables new possibilities where interesting three-level physics can now be engineered and explored [29].

Extending to designs with multiple giant artificial atoms, Kockum et.al, predicted interesting new regimes when these artificial atoms are connected in certain physical geometries [28]. One such topology is when two giant artificial atoms are connected in a braided configuration. In this particular design, the qubits interact with each other in a decoherence-free space (DCF), where both the individual relaxation rates and the collective decay rates of the qubits are zero but with a non-zero exchange interaction between them. Such a setup is valuable from a quantum communication perspective where waveguides are required to transfer information between different parts of a larger superconducting network in a DCF environment. In this section, we briefly review the work presented in [27] and [28] to motivate our experimental efforts in this direction.

2.5.1 Single-giant artificial atom

Here, we review some of the main aspects of a giant artificial atom which is coupled to a 1D TL at multiple points using the results presented in [27]. The TL is suitably meandered such that the spacing between subsequent coupling points is of the order of λ as illustrated by a cartoon in Fig. 2.14(a), where a giant artificial atom is coupled at three points along a meandered TL. We consider the symmetric case where the coupling strength at each point is the same and the distance between subsequent coupling points is constant, i.e, $x_2 - x_1 = x_3 - x_2 = \lambda$. The phase acquired by a photon as it propagates between the

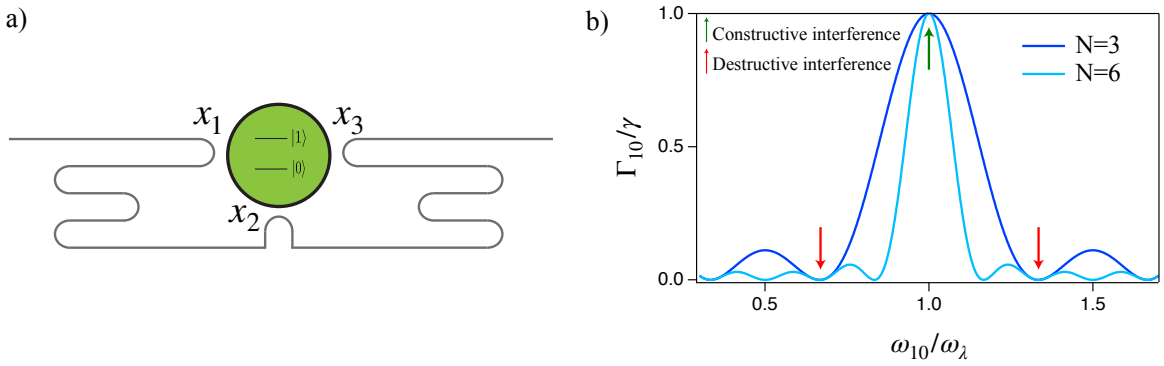

Figure 2.14: (a) Cartoon of a giant artificial atom coupled to a TL at three points. (b) Normalized Γ_{10} for the $|0\rangle - |1\rangle$ transition of the giant artificial atom vs. $\omega_{10}/\omega_\lambda$ [27]. The arrows show the frequency points where the qubit is strongly and weakly coupled to the TL. The value of ω_λ is fixed by design.

coupling points is given by,

$$\phi = \frac{\omega_{10}}{v}(x_2 - x_1) = 2\pi\frac{\omega_{10}}{\omega_\lambda}, \tag{2.41}$$

where, ω_{10} is the $|0\rangle - |1\rangle$ transition frequency of the transmon and $\omega_\lambda = 2\pi v/\lambda$ which is fixed by design. The phase ϕ can thus be varied by varying ω_{10}. The relaxation rate Γ_{10} depends on ϕ and is worked out to be [27],

$$\Gamma_{10}(\omega_{10}) = \gamma\frac{1-\cos(N\phi)}{1-\cos(\phi)} \tag{2.42}$$

where, γ is the bare relaxation rate without any interference effects and N is the number of connection points. Figure 2.14(b) shows Γ_{10}/γ as a function of $\omega_{10}/\omega_\lambda$ for different N. When $\omega_{10} = \omega_\lambda$ (shown by green arrow), we see a maximum in the profile as ϕ contributes to the constructive interference of the emission/absorption amplitudes of the giant transmon. At this point, the giant transmon is maximally coupled to the TL. We also observe frequency points where the coupling is ideally turned off (shown by red arrows). These points correspond to when the emission/absorption amplitudes destructively interfere. By increasing the number of coupling points, we see that the frequency dependence of the coupling can be made much stronger resulting in more frequency points where the coupling is zero.

Another striking feature of a giant transmon is the ability to relatively tune the relaxation rates of its multiple transitions. For the first two transitions of the transmon, we

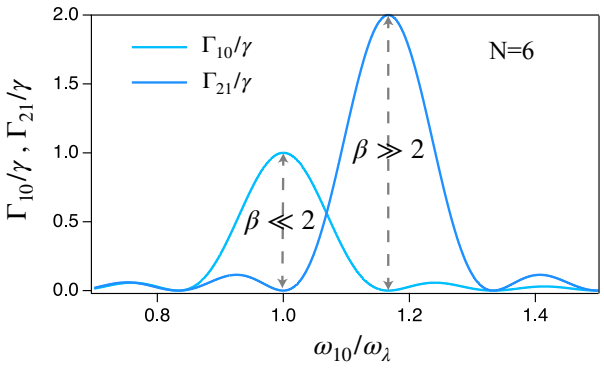

Figure 2.15: Relative modulation of the relaxation rates of the $|0\rangle - |1\rangle$ and $|1\rangle - |2\rangle$ transition for anharmonicity chosen such that $E_c/\hbar = 0.166\omega_\lambda$ for an artificial atom with six coupling points [27]. By biasing the $|0\rangle - |1\rangle$ transition at the frequency points marked by dashed arrows, β can be enhanced or suppressed

can define the relaxation rate modulation factor, $\beta = \Gamma_{21}/\Gamma_{10}$. Using Eq. (2.40), $\beta = 2$ for an ordinary transmon. For the giant transmon, we can modulate β by choosing the anharmonicity such that when the $|0\rangle - |1\rangle$ transition is minimally coupled, the $|1\rangle - |2\rangle$ transition can be maximally coupled or vice-versa. This is shown in Fig. 2.15 for $N = 6$, where we plot Γ_{10} and Γ_{21} for an anharmonicity $E_c/\hbar = 0.166\omega_\lambda$ using the analysis presented in [27]. At the two frequency bias points shown by grey arrows, we observe that β can be modulated strongly, deviating from the factor 2. In order to obtain maximum modulation of β on both sides of the spectrum, the anharmonicity plays an important role. Increasing the number of connection points, eases the requirement of E_c.

The ability to modulate β, allows many interesting quantum optics effects that can now be explored with the giant transmon as a metastable state can now be engineered. One particular effect, which we explore is electromagnetically induced transparency (EIT) which is discussed in Chapter 5.

2.5.2 Braided-giant artificial atoms

The single giant transmon reviewed in the previous section can now be extended to multiple giant transmons which forms the basis of the theoretical study presented in [28]. Since each transmon has multiple coupling points, the qubits can now be connected in multiple ways. Out of these, we are interested in the case of the braided giant transmons. A cartoon

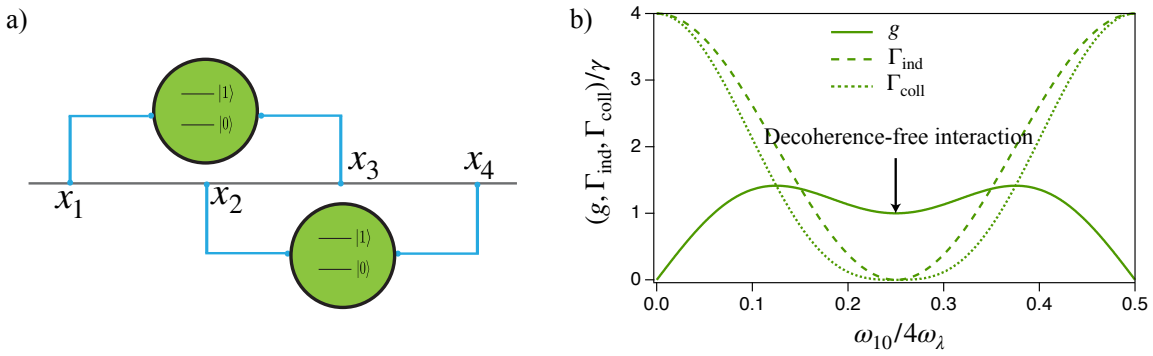

Figure 2.16: (a) Cartoon of giant artificial atoms, each with two coupling points to a TL, connected in a braided configuration. (b) Theoretical rates for the braided giant transmon configuration [28]. There exists a special frequency bias point shown by the arrow, where the qubits can have an exchange interaction in a decoherence-free environment. The interaction is mediated by virtual photons in the TL.

illustrating the braided transmons is shown in Fig. 2.16(a) where each transmon has two coupling points to the TL and are braided such that the first connection point x_2 of the bottom transmon is between the first x_1 and the second connection point x_3 of the top transmon.

As before, we are interested in the symmetric case where the coupling of the transmon to the TL is the same at each connection point and the spacings between the points is fixed, i.e, $x_2 - x_1 = x_3 - x_2 = x_4 - x_3 = \lambda/4$. For simplicity, both transmons are identical. The transmons are characterized by their individual relation rate, Γ_{ind}, collective decay rate, Γ_{coll}, and the exchange interaction strength, g which is mediated by the TL. Using the results from [28], these rates are expressed as,

$$\begin{aligned} \Gamma_{\text{ind}} &= 2\gamma(1 + \cos 2\phi) \\ \Gamma_{\text{coll}} &= \gamma(3\cos\phi + \cos 3\phi) \\ g &= \frac{\gamma}{2}(3\sin\phi + \sin 3\phi) \end{aligned} \tag{2.43}$$

where, ϕ is the phase as defined earlier. The normalized rates are plotted in Fig. 2.16(b) as a function $\omega_{10}/\omega_\lambda$. It is to be noted that Γ_{coll} is plotted as $|\Gamma_{\text{coll}}|$. The striking feature of the braided transmon design is the operating point $\omega_{10} = \omega_\lambda$ where $\Gamma_{\text{ind}} = \Gamma_{\text{coll}} = 0$ but $g \neq 0$. At this bias point, referred to as the DCF frequency, the qubits interact with each other in a decoherence-free environment, mediated by virtual photons in the TL. Photon-mediated interactions between distant qubits have been previously demonstrated

in circuit QED [22], but not in a fully protected space. Recently, at the time of our own experimental explorations with braided transmons, the DCF interaction was experimentally demonstrated by another competing group [73].

2.6 Photonic piston using superconducting resonators

We now switch gears to discuss a theoretical proposal on the implementation of a quantum heat engine using superconducting resonators. We call this the "Photonic piston". The system consists of two resonators: a high frequency, SQUID-terminated $\lambda/4$ resonator, which is analogous to a mechanical piston and a low frequency, $\lambda/2$ resonator which is used to store the work thus performed in the form of a coherent current at steady state. This section introduces the basics of such a device.

2.6.1 Optomechanical-like interaction Hamiltonian

In order to better understand the photonic piston engine, it is good to build an intuition for it from standard optomechanics theory [74]. As it turns out, the optomechanical interaction Hamiltonian, which we will discuss shortly, closely simulates the piston action in our device. To see this, consider a standard optomechanical setup as shown in Fig. 2.17(a). The setup consists of an optical cavity, with resonance frequency ω_c, made up of two semi-transparent mirrors out of which one of them can mechanically vibrate with resonance frequency Ω_m. As the mirror vibrates, ω_c changes. In other words, the position of the movable mirror parametrically couples to the cavity's resonance frequency. The Hamiltonian of such a system can be written as,

$$H = \hbar\omega_c a^\dagger a + \hbar\Omega_m b^\dagger b,$$

where, $a(a^\dagger)$ and $b(b^\dagger)$ are the annihilation(creation) operators for photons and phonons respectively. Since the position co-ordinate x of the movable mirror parametrically couples to the cavity's resonance frequency $\omega_c(x)$, one can expand ω_c near the equilibrium position of the mirror, $x_0 = 0$ as:

$$\omega_c(x) = \omega_c + x\frac{\partial\omega_c}{\partial x} + ...$$

Using just the linear term in the expansion, the Hamiltonian of the system can be re-written as:

$$H = \hbar\omega_c a^\dagger a + \hbar\Omega_m b^\dagger b - \hbar G x_{\text{zpf}} a^\dagger a \left(b + b^\dagger\right) \tag{2.44}$$

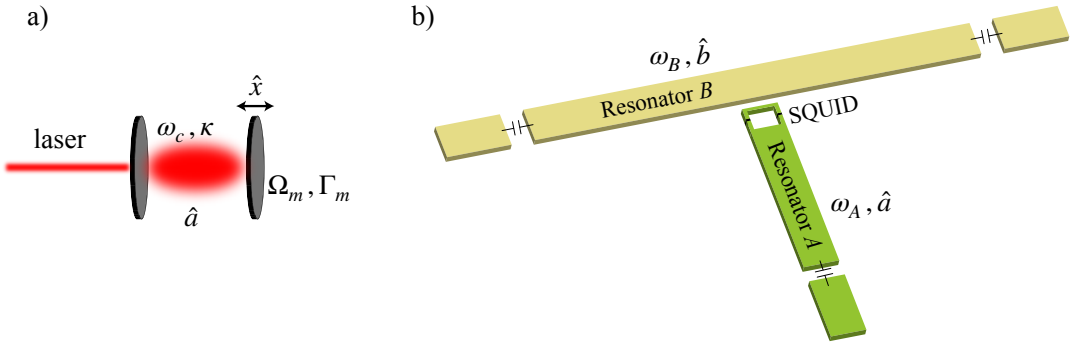

Figure 2.17: (a) A typical optomechanical setup consisting of two mirrors forming an optical cavity of frequency ω_c. One of the mirrors can mechanically vibrate with frequency Ω_m as shown. (b) Illustration of superconducting resonators implementing an optomechanical-like interaction in an all-electrical network. The nonlinear interaction is mediated by the SQUID.

where, $G = -\partial\omega_c/\partial x$ is the cavity pull-in parameter, x_{zpf} is the zero point fluctuations of the mirror and $x = x_{\text{zpf}}\left(b + b^\dagger\right)$ is the position operator. The single photon coupling strength is given by $g_0 = Gx_{\text{zpf}}$. The parametric interaction Hamiltonian $H_I = -\hbar G x_{\text{zpf}} a^\dagger a \left(b + b^\dagger\right)$ is non-linear, i.e, the position of the movable mirror, x, couples to the photon number operator, $a^\dagger a$, of the optical cavity. The origin of this interaction comes from radiation pressure due to the photon momentum transfer to the movable mirror when the cavity is excited by a laser at ω_c. When photons collide with the movable mirror, the force corresponding to the radiation pressure acting on the mirror is given by the gradient of the interaction energy:

$$F = -\frac{\partial H_I}{\partial x} = \hbar G a^\dagger a \tag{2.45}$$

From Eq. (2.45), we see that for a fixed cavity pull-in G, as the cavity photon number changes, the backaction force due to radiation pressure changes, leading to the displacement of the mirror. The larger the backaction drive, the more the mirror displaces. To model the movable mirror as a piston, one can imagine the mirror being connected by a spring. As the mirror compresses the spring, the cavity's effective resonance frequency decreases resulting in a situation similar to the expansion stroke of an automobile. The restoring force due to the spring pushes the piston back, similar to the compression stroke.

To implement such an interaction using superconducting resonators, Johansson et al., demonstrated that quantized field amplitude in one resonator can couple to the pho-

ton number in another resonator using a nonlinear parametric interaction mediated by a SQUID [52]. This system implements the same interaction Hamiltonian given by Eq. (2.44), but in an all electrical system. The electrical network composed of the two superconducting resonators is shown in Fig. 2.17(b). Resonator A is a SQUID-terminated $\lambda/4$ resonator and resonator B is a $\lambda/2$ resonator. The resonators are coupled to the feedlines via coupling capacitors at their ends. The SQUID is positioned near the current antinode of the $\lambda/2$ resonator. The nonlinear interaction is mediated by the SQUID due to its sensitivity to an external magnetic flux Φ_{ext} which has two components: a fixed DC component Φ^0_{ext}, applied by an external coil and a small AC component $\Delta\Phi^B$, generated by the zero-point fluctuations of the current I^B_{zpf} of resonator B near the vicinity of the SQUID. As a result, the resonance frequency of the $\lambda/4$ resonator, ω_A, changes in response to Φ_{ext}. In other words, $\Delta\Phi^B$ generated by I^B_{zpf} of resonator B parametrically couples to the resonance frequency ω_A or the energy of resonator A. By Taylor expanding $\omega_A(\Phi_{\text{ext}})$ around Φ^0_{ext} and keeping only the linear term, the Hamiltonian of this circuit can be written as,

$$H = \hbar\omega^0_A a^\dagger a + \hbar\omega_B b^\dagger b + \hbar\Delta\Phi^B_{\text{zpf}}\frac{\partial\omega_A}{\partial\Phi_{\text{ext}}}a^\dagger a(b+b^\dagger), \tag{2.46}$$

where, ω^0_A is the resonance frequency at $\Phi_{\text{ext}} = \Phi^0_{\text{ext}}$, $\Delta\Phi^B = \Delta\Phi^B_{\text{zpf}}(b+b^\dagger)$ and $\partial\omega_A/\partial\Phi_{\text{ext}}$ is the slope of the frequency tuning profile of resonator A at $\Phi_{\text{ext}} = \Phi^0_{\text{ext}}$. The zero point fluctuations of the current in resonator B, I^B_{zpf}, generates a flux $\Delta\Phi^B_{\text{zpf}} = I^B_{\text{zpf}}L_{\text{tot}}$ which is proportional to the total loop inductance L_{tot} of the SQUID. Identifying $I^B_{\text{zpf}} = \sqrt{\hbar\omega_B/L_B}$, where L_B is the total inductance of resonator B, the single-photon coupling strength can then be written as,

$$g_0 = \frac{\partial\omega_A}{\partial\Phi_{\text{ext}}}L_{\text{tot}}\sqrt{\frac{\hbar\omega_B}{L_B}}. \tag{2.47}$$

Thus, g_0 can be increased by biasing the SQUID near $\Phi_0/2$ where $\partial\omega_A/\partial\Phi_{\text{ext}}$ is maximum, as seen from Fig. 2.10. The SQUID loop inductance $L_{\text{tot}} = L_{\text{geom}} + L_{\text{kin}}$, where L_{geom} is the geometric inductance and L_{kin} is the kinetic inductance of the SQUID loop. Normally for a SQUID, L_{kin} is negligible. However, by modifying the geometry of the SQUID, we can boost the kinetic inductance in order to increase g_0. In order to couple the SQUID to resonator B, it was proposed that the galvanic coupling scheme will give the largest g_0 compared to when the SQUID is inductively coupled to resonator B [52]. We propose to complement the galvanic coupling scheme by further increasing g_0 by taking advantage of the kinetic inductance of the SQUID's coupling arm. Figure. 2.18(a) shows a proposed design of the coupled resonator system where the SQUID is galvanically coupled to resonator B, i.e, part of the ground plane of resonator B in incorporated into the geometry of the SQUID. By meandering the SQUID's coupling arm in the form of a long

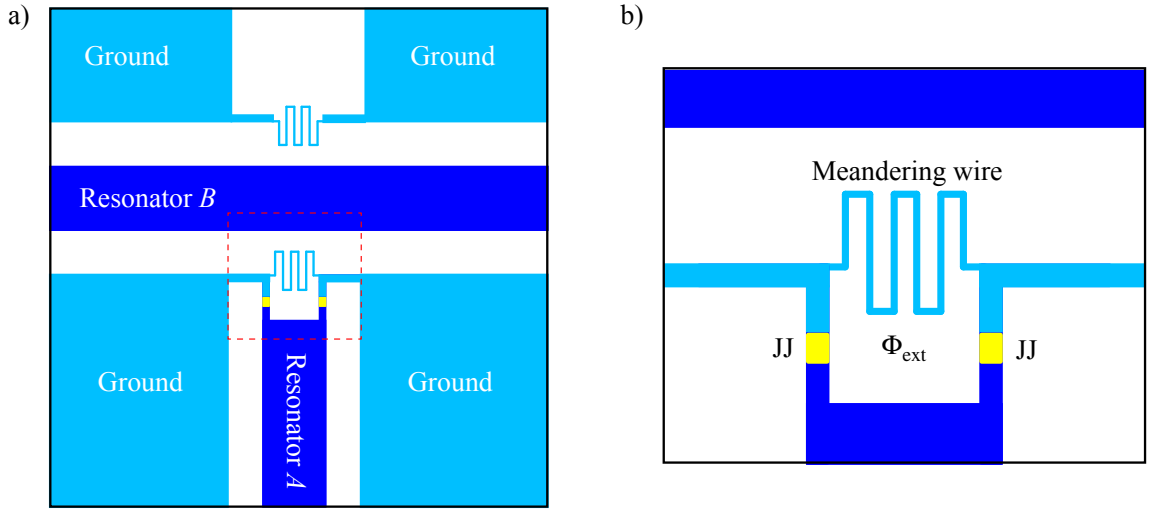

Figure 2.18: Cartoon of a coupled-resonator system where the SQUID of resonator A is galvanically connected to the ground plane of resonator B to implement the nonlinear optomechanical-like interaction Hamiltonian. (b) Closeup of the coupling arm of the SQUID, which forms a part of resonator B's ground plane, is thin and meandered to increase g_0 by boosting its kinetic inductance.

thin wire (see Fig. 2.18(b)) we can increase its kinetic inductance which further increases g_0. From Fig. 2.18(a), the ground plane of resonator B is intentionally split using the meandering wire geometry to ensure that the ground current symmetrically distributes along the meandering wire on both sides of resonator B.

The galvanic coupling scheme is shown to be a promising architecture to reach the single-photon strong-coupling regime in this coupled-resonator system [52], a primary requirement for realizing a quantum heat engine with this device.

2.6.2 Otto-cycle using the photonic piston

In this section, we discuss the implementation of an Otto-cycle using the coupled-resonator system. The resonance frequencies are chosen such that $\omega_A \gg \omega_B$. The device is cooled down to a low temperature T_0 using a standard dilution refrigerator, such that $\hbar\omega \gg k_B T_0$. Although this condition ensures that both resonators are operating in the quantum regime where the number of thermal photons is small, due to the difference in the resonance

frequencies, resonator B has a higher background thermal occupation than resonator A. For an engine operation, designing its cold and hot bath environment is crucial from an operation standpoint as the efficiency of the engine depends on the temperature difference between its hot and cold baths [75]. For the photonic piston engine, the baths are engineered in the following way.

Bath engineering

To ensure that the average thermal occupation $\bar{n}_A$ and $\bar{n}_B$ in both resonators is the same, a continuous quasi-thermal noise drive with appropriately chosen amplitudes is applied at the input of both resonators. The use of a noise drive to vary the average thermal population, and hence the effective photon temperature in a superconducting resonator, has been experimentally demonstrated where effective temperatures of up to 100 K was achieved [76]. The amplitude of the noise drive determines the photon temperature. The large internal quality factors of these resonators ensures that the noise does not cause dissipation, thus allowing for arbitrary large effective photon temperatures. The average thermal occupation of the photons in the resonators is given by the Plank distribution formula as,

$$\bar{n}_i = \frac{1}{\exp\left(\hbar\omega_i/k_B T_i\right) - 1}, \tag{2.48}$$

where T_i with $i = (A, B)$ represents the effective photon temperature in resonators A and B. To ensure $\bar{n}_A = \bar{n}_B$ when $\omega_A \gg \omega_B$, Eq. (2.48) suggests that $T_A \gg T_B$ which is achieved by the continuous noise drives. The cold bath, $\bar{n}_c$, for resonator A and B is thus set by T_A and T_B respectively when $\bar{n}_A = \bar{n}_B = \bar{n}_c$.

To engineer the hot bath, $\bar{n}_h$, a second noise drive to simulate $\bar{n}_h$ is applied at the input of resonator A whose amplitude is modulated by square pulse [53]. This periodic noise drive simulates the heating and cooling cycle of an engine, i.e, when the pulse is ON the steady-state effective thermal occupation $\bar{n}'_A$ of resonator A is $\bar{n}'_A = (\bar{n}_c + \bar{n}_h)/2$ and when the pulse is OFF, $\bar{n}'_A = \bar{n}_c$ [53]. Thus, the heating stage raises the photon number which is equivalent to increasing the effective photon temperature and the cooling stage couples the resonator A to $\bar{n}_c$ thus reducing the temperature back to its initial value. Resonator B is always coupled to its cold bath n_c. Figure 2.19(a) illustrates the noise driving scheme of the coupled-resonator system.

Dynamics using classical Langevin equations

To study the classical dynamics of the system, the Hamiltonian given by Eq. (2.46) can be treated as a classical model. By replacing the annihilation(creation) operators with complex amplitudes, i.e, $a \to \alpha_A$ and $b \to \alpha_B$, the Langevin equations of motion for the two resonators can then be written as [53],

$$\begin{aligned}\dot{\alpha}_A &= -\left(i\omega_A - ig_0\left(\alpha_B^* + \alpha_B\right) + \frac{\kappa_h}{2} + \frac{\kappa_A}{2}\right)\alpha_A + \xi_h(t) + \xi_A(t),\\ \dot{\alpha}_B &= -\left(i\omega_B + \frac{\kappa_B}{2}\right)\alpha_B + ig_0\left|\alpha_A\right|^2 + \xi_B(t),\end{aligned} \tag{2.49}$$

where, κ_h, κ_A and κ_B set the coupling of the two resonators to their hot and cold baths, $\xi_h(t)$ is the delta-correlated stochastic noise simulated the hot bath, $\xi_A(t)$ and $\xi_B(t)$ simulate the noise from the cold bath drive. Here, we assume that $\kappa_h = \kappa_A$ during the heating stage and $\kappa_h = 0$ during cooling. By rewriting the complex amplitudes of the resonators in the form of their quadrature amplitudes, i.e, for $i = (A, B)$, $\alpha_i = (X_i + iY_i)/\sqrt{2}$ and writing $\xi_i = \xi_x^i + i\xi_y^i$ for the the bath environments for the resonators, a set of four-coupled differential equations can be written down as [53],

$$\begin{aligned}dX_A &= \left[\omega_A Y_A - g_0\sqrt{2}X_B Y_A - \kappa_A' X_A\right]dt + dW_x^h + dW_x^A,\\ dY_A &= -\left[\omega_A X_A - g_0\sqrt{2}X_A X_B + \kappa_A' Y_A\right]dt + dW_y^h + dW_y^A,\\ dX_B &= \left[\omega_B Y_B - \frac{\kappa_B}{2}X_B\right]dt + dW_x^B,\\ dY_B &= -\left[\omega_B X_B + \frac{\kappa_B}{2}Y_B - \frac{g_0}{\sqrt{2}}\left(X_A^2 + Y_A^2\right)\right]dt + dW_y^B,\end{aligned} \tag{2.50}$$

where, $\kappa_A' = (\kappa_h + \kappa_A)/2$, $dW_k^i = \xi_k^i dt$ for $k = (x, y)$ is the Wiener stochastic process of width $\sqrt{\kappa_i \bar{n}_i dt}$ [53].

The coupled equations can be solved numerically using realistic experimental parameters where Gaussian noise is used to simulate the necessary noise drives discussed before. The parameters used for the simulation are the same as used in [53], i.e, $\omega_A/2\pi = 10$ GHz, $\omega_B/2\pi = 500$ MHz, $\kappa_A/2\pi = 2$ GHz, $\kappa_B/2\pi = 50$ MHz, $g_0/2\pi = 2$ GHz, $\bar{n}_A = \bar{n}_B = \bar{n}_c = 0.01$ and $\bar{n}_h = 0.125$. Resonator A's coupling to the hot bath is modulated at $\omega_B/2\pi$ such that each stage of heating and cooling takes a time of (π/ω_B) s. The simulation parameters are normalized to ω_A. Figure 2.19(b) shows the modulation of the photon number in resonator A for many cycles of heating and cooling the resonator due to the periodic, incoherent noise drive. Due to the nonlinear parametric interaction, we see an emergence of

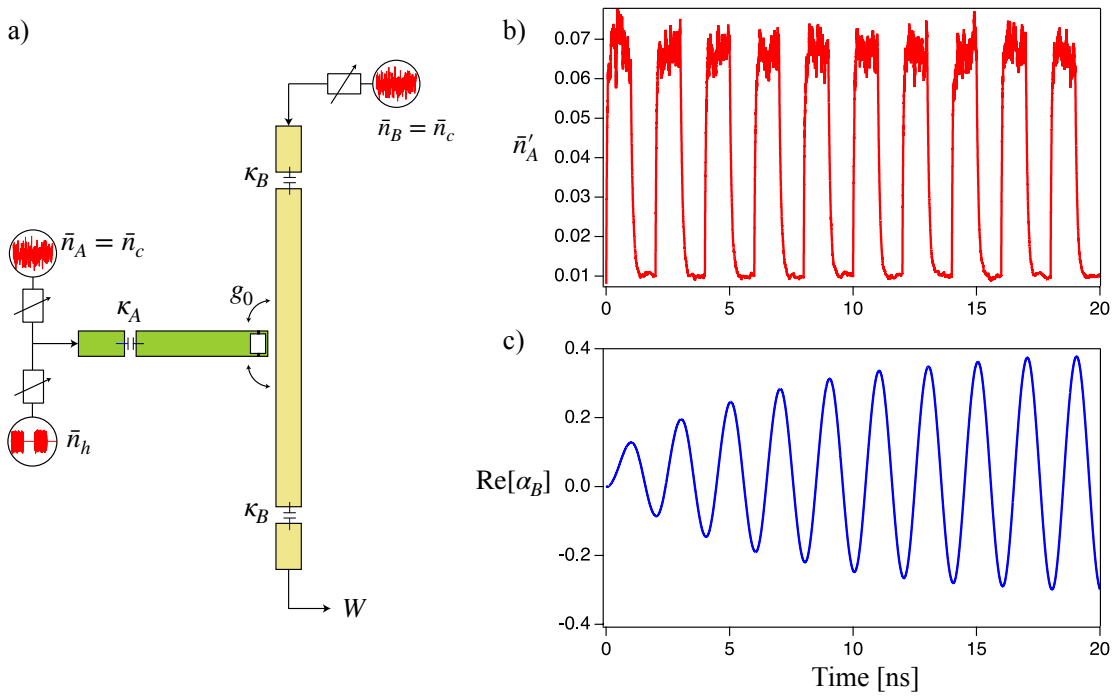

Figure 2.19: (a) Implementing cold and hot baths for the photonic piston engine using the coupled-resonator system. The cold baths for both resonators are set by the continuous noise drives such that $\bar{n}_c = \bar{n}_A = \bar{n}_B$. The hot bath is implemented by a periodic noise drive such that $n_h > n_c$. (b) The photon number in resonator A, $\bar{n}'_A$, is modulated as a result of heating and cooling with the noise drives on resonator A for many cycles. (c) The real part of the complex field amplitude in resonator B showing the build up of a coherence in time.

a coherent build up of current in resonator B as shown in Fig. 2.19(c), thus demonstrating the basic nature of a heat engine i.e, conversion of incoherent heat to coherent work.

Otto-cycle using photonic-piston engine

The Otto-cycle, proposed by German engineer Nikolaus Otto, is at the heart of modern day internal combustion engines [75]. The cycle of the engine can be described by the illustration shown in Fig. 2.20(a) which is drawn specific to the photonic-piston engine, but is easily generalized to any system which implements the Otto-cycle.

By heating and cooling the photons of resonator A for many cycles, a limit cycle for the

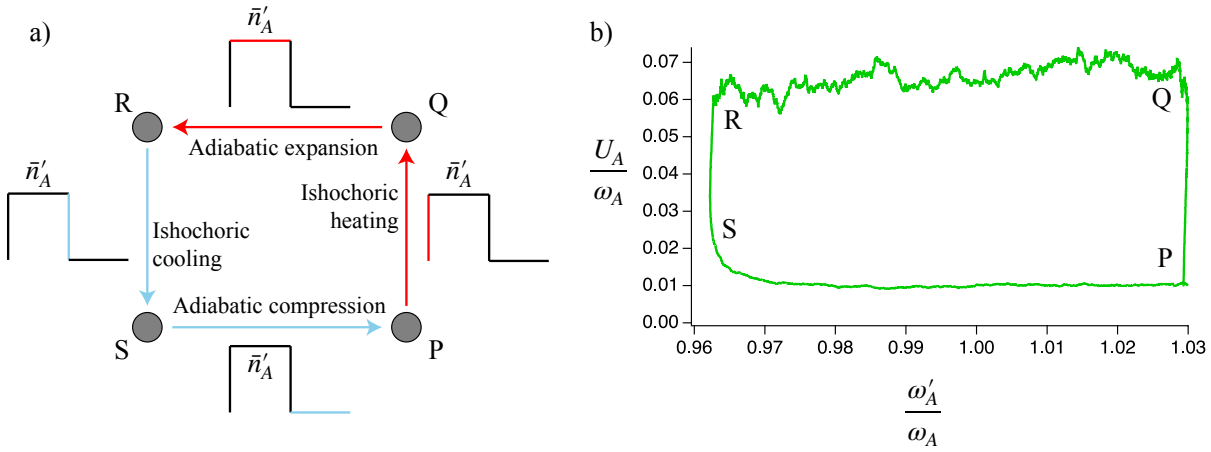

Figure 2.20: (a) Different stages of an Otto-cyle using the photonic-piston engine. (b) A limit cycle is established at steady-state showing resonator A's internal energy U_A as a function of its effective resonance frequency ω'_A. Its operation mimics the workings of an Otto cycle.

system is established at steady state which mimics the Otto-cycle of engine operation [75]. The simulated Otto-cycle is shown in Fig. 2.20(b) where the internal energy of resonator A, $U_A = \omega'_A n'_A$, is plotted as a function of $\omega'_A = \omega_A - 2g_0\mathrm{Re}[\alpha_B]$. The cycle is typically represented by four stages: (P-Q) An isochoric heating stage where the effective photon temperature of resonator A is increased during the raising edge of the noise pulse acting on resonator A. This process happens at a constant ω'_A, which simulates an isochoric process where the work done by the piston is zero. At Q, the temperature of resonator A reaches thermal equilibrium. (Q-R) In this leg of the cycle, the noise pulse is ON and the piston adiabatically expands resulting in the increase of the electrical length of resonator A, thus reducing ω'_A. There is build up of coherence in resonator B in the form of a current which translated to the work done by the piston. (R-S) Here, the noise pulse is turned OFF and the photon temperature in resonator A begins to reduce at constant ω'_A. The resonator A attains its equilibrium temperature as it is now coupled to its respective cold bath. No work is done in this stage. (S-P) This adiabatic compression stage pushes the piston, while increasing ω'_A to its initial value and in the process reverses the direction of current in resonator B.

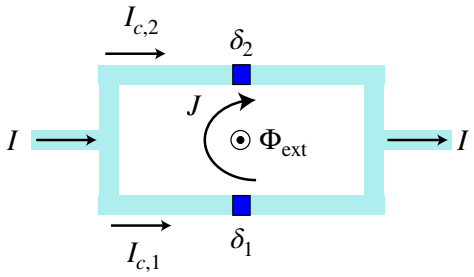

Figure 2.21: Illustration showing the circulating current in a SQUID in response to an applied flux

2.6.3 Dependence of SQUID bias current vs. circulating current

The classical Langevin equations helps to build an intuitive understanding of the dynamics of the photonic-piston engine. To understand the physical mechanism of the piston action mediated by the SQUID, it is useful to look at the response of the SQUID when the photon number of resonator A is modulated. To see this, consider the SQUID with an input current I and flux-biased at an external DC flux Φ_{ext} as shown in Fig. 2.21. A superconducting loop, such as the SQUID, generates a circulating current J in the loop to counter this applied field. As a result, the currents in the SQUID branches are no longer equal. For a symmetric SQUID, the input current I can be written as,

$$I = 2I_c \sin\left(\frac{\delta_1+\delta_2}{2}\right)\cos\left(\frac{\delta_1-\delta_2}{2}\right), \tag{2.51}$$

where, I_c is the critical current of each junction. The circulating current can be worked out to be,

$$J = I_c \sin\left(\frac{\delta_1-\delta_2}{2}\right)\cos\left(\frac{\delta_1+\delta_2}{2}\right). \tag{2.52}$$

The fluxoid quantization condition gives $\delta_1-\delta_2 = 2\pi n+2\pi(\Phi/\Phi_0)$, where $\Phi = \Phi_{\text{ext}}-L_{\text{tot}}J$. Writing $\delta = (\delta_1+\delta_2)/2$ and with some algebraic manipulations, we obtain the following equation,

$$J^2 = I_c^2 \sin^2\frac{\pi\Phi}{\Phi_0} - \frac{I^2}{4}\tan^2\frac{\pi\Phi}{\Phi_0}. \tag{2.53}$$

By Taylor expanding the trigonometric terms in Eq. (2.53) around Φ_{ext}, we can show that for small values of J, $J \sim I^2$. This suggests that the number of photons which is proportional to I^2 also can vary J. Hence modulating the photons in a SQUID terminated

$\lambda/4$ resonator, is equivalent to modulating J. For the case of the coupled-resonator system, since the coupling arm of the SQUID forms a part of the ground plane of resonator B, the circulating current J in the SQUID directly couples with the current in resonator B.

Chapter 3

Design and Simulations

This chapter presents the various design considerations and methodologies that form the basis for realizing the central ideas presented in this thesis. We begin with the necessary equations, introduced earlier in Chapter 2, for numerical modeling of the proposed devices. We do this at the level of choosing the initial parameters to have the devices work in the right regime of operation. We also perform circuit and electromagnetic simulations using commercially available simulation packages from Keysight and Ansys. The microwave simulations help us iterate designs and adds a level of confidence to the overall final design. In this chapter, we will present simulations which were performed on the measured devices with feedback on how future designs can be improved by considering several design variations.

3.1 Single-giant transmon

This section discusses the design methodology for two separate devices each with a single-giant transmon qubit having three (3CP) and six coupling points (6CP) to a one-dimensional transmission line (TL), which has a characteristic impedance of 50 Ω. The CPW architecture which is used to fabricate the TL is discussed in Chapter 2. The devices presented in this section, which will be referred to as 3CP and 6CP hereon, will be the focus of discussion in Chapter 5.

The goal of these devices is to study the giant atom effects discussed in [27], for instance, the frequency dependence of the qubit's relaxation (coupling) to its electromagnetic environment as a function of the number of coupling points. In Chapter 2, we saw that

the qubit's coupling to the TL reaches a maximum when its transition frequency corresponds to the inter-coupling distance, $\omega_\lambda^{\mathrm{S}}$, where the superscript SGT refers to single-giant transmon. We also saw that the coupling can also ideally vanish at other frequency points around $\omega_\lambda^{\mathrm{S}}$. From a design standpoint, this translates to having a qubit with wideband tunability in our measurement bandwidth of 4-8 GHz with appropriately chosen $\omega_\lambda^{\mathrm{S}}$ so that we can map the frequency-dependent coupling behavior. In this section, we address these design goals and simulate the device behavior using idealized circuit models and full-chip electromagnetic simulations of the final device layout.

3.1.1 Qubit parameters

To have a tunable transmon qubit, we need to replace the single Josephson junction (JJ) with a pair of JJs forming a closed superconducting loop, more popularly known as a SQUID. The properties of the SQUID are discussed in more detail in Chapter 2. The more relevant parameters of the tunable transmon qubit, hereafter referred to as transmon, are its maximum Josephson energy, $E_J^{\max}$, and the charging energy, E_c, which depends on the geometry of the shunting capacitor electrodes which also provides the necessary coupling of the qubit to the TL. The resulting capacitance matrix of the transmon can be simplified using linear circuit analysis where we will derive expressions for E_c and the voltage-coupling constant, β_g, of the transmon to the TL. $E_J^{\max}$ is a parameter that depends on the fabrication conditions of the JJs whereas E_c is controlled solely by design. By targeting a certain $E_J^{\max}$ and E_c, it is possible to park the maximum frequency of the qubit anywhere in the measurement band as discussed in Chapter 2. For our purposes, we park it outside the measurement band for two reasons. Firstly, this allows us to capture a background trace without the qubit spectrum which is useful for fitting our experimental data. Secondly, since our qubit is frequency tunable using an external coil, we can study the frequency dependence of its relaxation rate over the full range of our measurement bandwidth of 4-8 GHz. Choosing the maximum frequency of the qubit inside the measurement band limits this frequency range.

Calculating the inter-coupling distance from $\omega_\lambda^{\mathrm{S}}$

In order to have wavelength-scale spacings between the coupling points of the giant transmon, we have to sufficiently meander the TL. The microwave photons in the TL pick up a phase as they travel between coupling points which contributes to constructive and destructive interference of the qubit emission amplitudes as discussed in Chapter 2. The phase acquired by the photon is given by Eq. (2.41). We will set $\omega_{10}/2\pi = \omega_\lambda^{\mathrm{S}}/2\pi = 5.75$ GHz as

the design frequency bias point which corresponds to maximum coupling of the qubit to the TL when $\phi = 2\pi$ (see Chapter 2 for more details). Substituting these in Eq. (2.41) gives us the required distance between coupling points, $(x_2 - x_1) = 20.54$ mm using the effective dielectric constant $\epsilon_{\text{eff}} = 6.45$ for a CPW on intrinsic silicon substrate with $\epsilon_r = 11.9$. In both 3CP and 6CP devices, we consider the symmetric case where all the distances between the coupling points are fixed at 20.54 mm.

Calculation of E_c and β_g

Our next design goal is to fix E_c which also dictates the anharmonicity of the giant transmon. We use Ansys's Q3DExtractor to iteratively design the geometry of the transmon's capacitor electrodes to achieve the required E_c. But before we dive into the actual numbers, let us look at the physical layout of a transmon circuit coupled to a CPW TL which is shown in Fig. 3.1(a). Here we consider a typical transmon qubit but the analysis is valid for a giant transmon as well. The SQUID (shown in grey) is shunted by two large inter-digitated electrodes (shown in red and green) which form the self-capacitance of the transmon qubit. The electrodes are capacitively coupled to the center conductor (blue) and the ground planes (light blue) of the TL and also serves to provide the necessary coupling of the qubit to its electromagnetic environment. A simplified circuit model can be written down by considering the capacitances between the different metal islands (nodes) as shown in Fig. 3.1(b). The nodes are appropriately numbered and colored corresponding to their respective layout in Fig. 3.1(a). The SQUID is represented by its equivalent junction capacitance C_J and Josephson energy E_J. By exciting the circuit with a DC voltage source, V, between appropriate nodes and solving the resulting set of linear equations as prescribed in [34], it is possible to extract both E_c and β_g.

The charging energy $E_c = e^2/2C_\Sigma$, where q is the electron's charge and C_Σ is the total capacitance of the transmon network. To calculate C_Σ, we inject a voltage V across nodes 1 and 2 (see Fig. 3.1(d)) and calculate the total capacitance seen from these nodes. We do it by writing a set of equations using Kirchhoff's laws and solving for the different voltages V_{ij}, across nodes i and j, and the charges $Q_{ij} = C_{ij}V_{ij}$ on the capacitors. The capacitance matrix, typically known as the Maxwell capacitance matrix, for the circuit layout can be generated using Q3DExtractor which gives us C_{ij} across the different nodes. Typically, the value of C_{34}, which is the capacitance between the CPW center conductor and the ground plane, is orders of magnitude larger than the other capacitances in the circuit. Hence, solving V_{ij} in the limit of large C_{34} gives us $V_{34} = 0$. This simplifies the circuit in

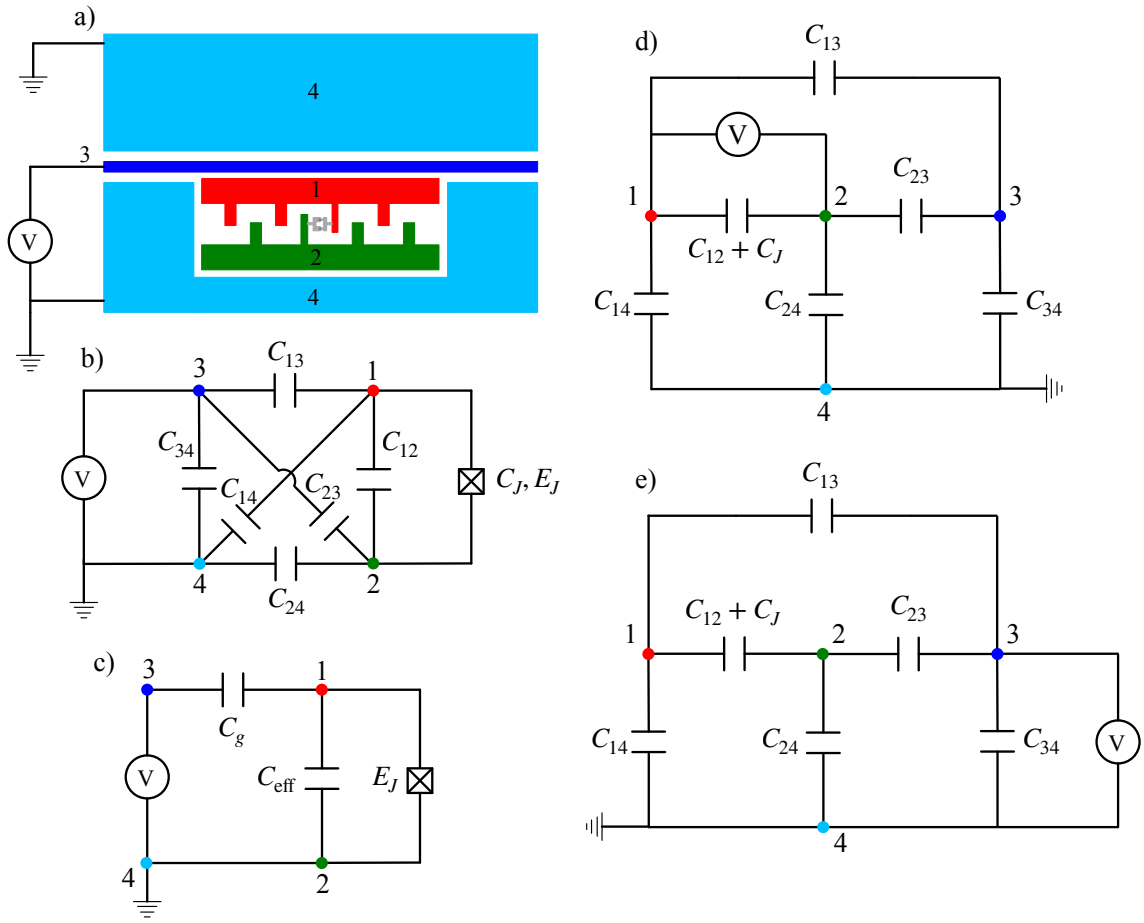

Figure 3.1: (a) Model of a transmon capacitively coupled to a CPW TL, where all the conductors are appropriately numbered. A voltage source V is used to excite the transmon. (b) Equivalent circuit of the model shown in (a) where each color-numbered node represents a conductor. The nodes are connected by capacitors, each representing the effective capacitance between the respective conductors. The JJ is shown by its circuit symbol. (c) Reduced capacitance network of (b). (d) Simplified circuit to extract E_c. (e) Circuit same as (b) where the JJ capacitance C_J is added between nodes 1 and 2.

Fig. 3.1(d) even further which then gives us:

$$C_\Sigma = C_{12} + C_J + \frac{(C_{13}+C_{14})(C_{23}+C_{24})}{(C_{13}+C_{14}+C_{23}+C_{24})}. \tag{3.1}$$

The design choice of E_c in our single-giant transmon devices is related to another novel feature of the giant transmon which is the ability to tune the relative relaxation rates of its different transitions, also discussed in Chapter 2. We will focus on the $|0\rangle - |1\rangle$ and the $|1\rangle - |2\rangle$ transitions which are separated in frequency by the transmon's anharmonicity. One of the goals of our work with giant transmons, is to engineer a maximally coupled $|1\rangle - |2\rangle$ transition at a frequency bias point where the $|0\rangle - |1\rangle$ transition is minimally coupled. However in order to achieve this, the anharmonicity between the transitions needs to be very high, roughly on the order of a GHz for both 3CP and 6CP devices from the theoretical estimates (see Chapter 2). This translates to C_Σ ~15-20 fF, which is difficult to achieve considering the physical size of the transmon electrodes. Another design limitation which arises due to such high E_c is the resulting choice of E_J. For instance, to design a transmon qubit with $\omega_{10}/2\pi = 6$ GHz and an $E_c/h = 1$ GHz requires an $E_J/h \sim 6$ GHz using Eq. (5.2). This gives us an $E_J/E_c = 6$ which is not an ideal transmon regime of operation (see Chapter 2). Considering these limitations, we aim to target $E_c/h \sim 500$ MHz for our giant transmon devices which seems like a reasonable tradeoff between design goals and practical implementation.

To design the required geometry of the giant transmon electrodes which gives us $E_c/h \sim 500$ MHz, we use Q3DExtractor to achieve the necessary $C_\Sigma \sim 38$ fF. Figure 3.2 shows the final layout of the giant transmon for the 3CP and 6CP devices. The different metal islands are color coded according to the generalized transmon structure shown in Fig. 3.1. The center conductor and the ground plane together with the transmon electrodes are all modelled as perfect electrical conductors. From the simulated Maxwell capacitance matrix, we estimate E_c to be close to the design value for both devices using Eq. (3.1). As depicted in Fig. 3.2, one of the capacitor electrodes (red) in both devices extends all the way across the coupling sites and is designed to ensure equal coupling to the TL at each site. The total length of this capacitor electrode is still much smaller when compared to the wavelength of interest.

Following the discussion from earlier, another key parameter of the transmon which can be extracted from the Maxwell capacitance matrix is β_g which is used to calculate the parameter g. To extract β_g, we re-write the capacitance network shown in Fig. 3.1(b) into a simple capacitive voltage divider circuit as shown in Fig. 3.1(c), where C_g is the gate capacitance which provides the necessary coupling capacitance to the transmon from the external driving source voltage V. Looking from the SQUID point of view, C_g and C_{eff}

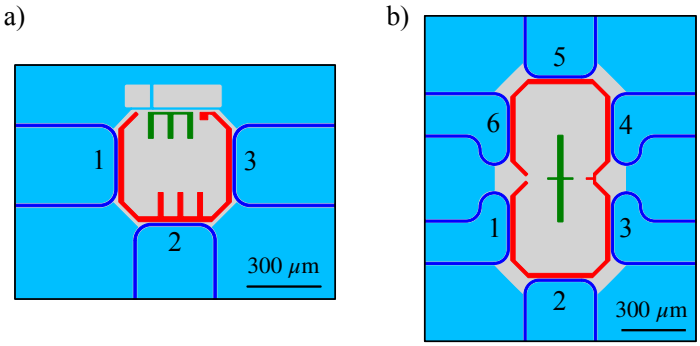

Figure 3.2: Q3DExtractor model for the giant transmons in 3CP and 6CP devices. The coupling sites are numbered and the layout is color-coded following the generalized transmon structure in Fig. 3.1

are in parallel which allows us to write $C_g + C_{\text{eff}} = C_\Sigma$, where we absorb C_J into C_{eff}. Since we can extract C_Σ using Eq. (3.1), the task now is to calculate C_g which is achieved by generating a set of equations using Kirchhoff's laws for the circuit in Fig. 3.1(e) and solving for V_{12} which can be written as:

$$V_{12} = V\left[\frac{C_{13}C_{24} - C_{23}C_{14}}{(C_{13}+C_{14})(C_{23}+C_{24}) + (C_{12}+C_J)(C_{13}+C_{14}+C_{23}+C_{24})}\right]. \tag{3.2}$$

The parameter β_g is then given by:

$$\beta_g = \frac{V_{12}}{V} = \frac{C_g}{C_\Sigma}. \tag{3.3}$$

The value of g that can be calculated using β_g gives the bare coupling constant of the giant transmon without including the interference effects.

3.1.2 Chip layout modelling

Once we have the giant transmon layout finalized, we move ahead on designing the 3CP and 6CP chip layout which involves meandering the TL suitably between the coupling sites. Care is taken so that the distance between the sites is equal to the designed value obtained from Eq. (2.41).

We study the chip behavior using both an ideal circuit model and a full-chip electromagnetic simulations. The ideal circuit model for the 3CP device is shown in Fig. 3.3(a).

The transmon structure is replaced by its equivalent capacitance network obtained from the Maxwell capacitance matrix discussed earlier. The SQUID is represented by a linear inductor L_J. The TL between the connection points is replaced by a CPW component with length λ equal to the inter-coupling distance calculated from Eq. (2.41). For the CPW parameters, we choose width $W = 10$ μm, gap $S = 6.5$ μm and the height of the substrate $H = 530$ μm. The circuit is then excited using 50 Ω ports at the input and output of the TL. As we will see later, this simple model captures the essential physics of the frequency-dependent coupling of the giant transmon. However, converting this idealized circuit model into an equivalent design layout involves full-chip electromagnetic modelling which brings out several design challenges.

The simulation methodology we adopt for layout simulations follows the central idea of black-box quantization (BBQ) technique introduced in [77]. The BBQ technique allows the designer to generate the quantized Hamiltonian of weakly anharmonic superconducting circuits comprised of Josephson junctions which are coupled to linear lumped-element or distributed networks. For our purposes, we are only interested in simulating the linear response of the meandering TL which is coupled to the transmon by treating the SQUID as a linear inductor. The black box approach we follow is shown pictorially in Fig. 3.3(b-e) where we use Ansys HFSS to simulate the S-parameters of our linear circuit.

We begin with the situation shown in Fig. 3.3(b), where the giant transmon is capacitively coupled to a linear microwave electromagnetic environment, such as the TL at multiple points. Equivalently, in circuit terms, this can be simplified to a situation depicted in Fig. 3.3(c), where the transmon is approximated by its equivalent circuit model (see Fig. 3.1(c)), where $L_J = (\Phi_0/2\pi)^2(1/E_J)$ is the linear part of the transmon's inductance. In order to simulate the overall linear response of this circuit, we break the problem into two parts. As a first simulation, we simulate the S-parameters from 4-8 GHz of the full-chip layout which consists of the giant transmon's capacitance electrode geometry ($C_\Sigma = C_g + C_{\text{eff}}$) and the meandering CPW TL. We introduce 50 Ω lumped ports at the input and output of the TL and also at the SQUID section (L_J) of the transmon. The simulated S-parameters model the effect of giant transmon's coupling to the TL and also includes any parasitic microwave effects, such as slotline modes [78, 79], that could arise due to the effect of meandering the TL. This completes the characterization of the microwave environment without the effect of the SQUID inductance.

For the second simulation, we use the S-parameter file (SnP) from the first simulation, which can be exported to a circuit simulator such as Keysight ADS, where we can now replace the SQUID excitation port as an inductor with a suitable value. By re-calculating the S-parameters of the TL with the inductor, we observe the transmon qubit resonance signature as a dip in the transmission co-efficient of the TL in the 4-8 GHz band. We

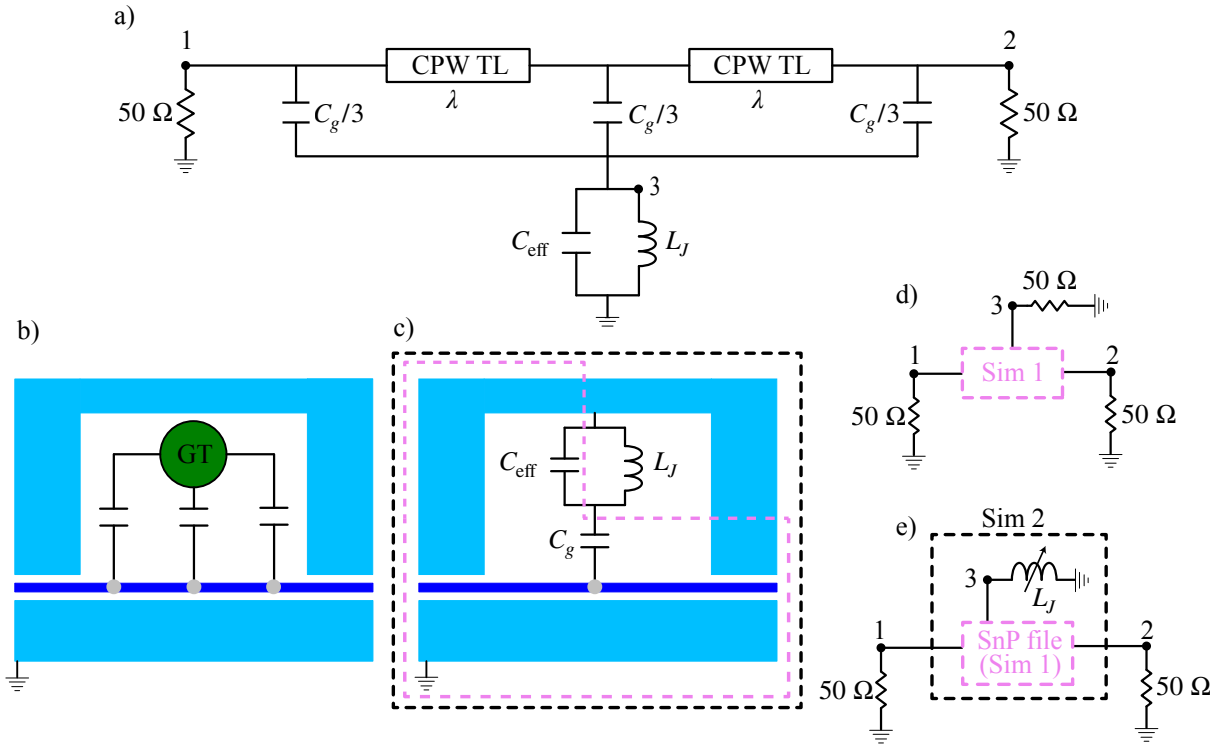

Figure 3.3: (a) Model of a giant transmon capacitively coupled to a CPW TL at three points. We use this model for the performing ideal circuit simulation by treating the SQUID as a linear inductor. The values of C_g and C_{eff} are obtained from Maxwell capacitance matrix simulated in Q3DExtractor. (b) Cartoon of a giant transmon coupled at three points to a CPW TL. In the actual layout, the electrodes of the transmon capacitance are included and the TL is meandered between the connection points. (c) The SQUID of the transmon is replaced by a linear inductor. The layout is comprised of the physical geometry of the TL and the transmon capacitance. The dashed colored boxes indicate the consideration for the layout simulations. (d) The pink box takes into account the physical layout alone and the simulation is done in HFSS. The inductor is replaced by a port along with the input and output ports of the TL. (e) The S-parameter results of (d) is exported into ADS, where the SQUID port is now replaced by an inductor and re-simulated to gives us the desired qubit resonance signature in the band of interest.

can now parametrically sweep the value of this inductance thereby changing the resonance frequency ω_{10} of the transmon near ω_λ^S. The linewidth of the resonance feature can be fit using Eq. (2.39) to extract the relaxation rate Γ_{10} and ω_{10}. By redoing this at different ω_{10} near ω_λ^S, we are able to simulate the frequency-dependent coupling $\Gamma_{10}(\omega)$ of the giant transmon.

3.1.3 Microwave simulations

This section discusses the simulation results for the idealized circuit model and the device layout for both 3CP and 6CP devices. With the device layout simulations, we compare various scenarios which include the effect of adding wirebonds and airbridges to suppress spurious modes possibly related to slotline mode propagation in the TL. The results we extract from these simulations seem to follow the theoretical prediction of the frequency-dependent coupling of the giant transmon providing useful insights on how future devices can be designed.

Following the simulation methodology discussed earlier, we extract Γ_{10} and ω_{10} by fitting the transmission spectrum for each value of the SQUID inductance L_J using Eq. (2.39) for both circuit and layout simulations. The results for the 3CP and 6CP devices are plotted in Fig. 3.4 and Fig. 3.5 respectively, where each simulation result is appropriately highlighted by a legend which describes the design variation considered below. Also shown in the figure is the microwave transmission background for the different design variations.

We begin by simulating the idealized circuit model using CPW TL components in Keysight ADS. The circuit for the 3CP device is shown in Fig. 3.3(a). For the 6CP device, we modify this circuit accordingly to include three more connection points. From Fig. 3.4(d) and Fig. 3.5(d), we see that the circuit simulation results agrees well with theoretical prediction for both devices [27]. As for the device layout simulations in HFSS, we present several design variations. As a first baseline simulation, we simulate the exact layout of the 3CP and 6CP device that was measured in the cryostat. The measurement results are discussed later in Chapter 5. Apart from validating the device design, one of the main reasons for undertaking in-depth layout simulations with variations in HFSS is to try and understand the observed experimental deviation of the frequency-dependent coupling behavior of the 3CP and 6CP devices from theoretical prediction which we discuss in Chapter 5. Allowing design variations in layout simulations has helped us identify this deviation which we mainly attribute to parasitic microwave effects like slotline modes which could originate due the breaks in the ground planes, meandering of the TL etc. To address this possible issue, we added aluminum wirebonds wherever possible across the

ground planes of the chip prior to mounting in the cryostat. The layout of the device with wirebonds in the same places as the measured chip is shown in Fig. 3.4(a-b) and Fig. 3.5(a-b) for both 3CP and 6CP devices respectively.

The parasitic modes are more obvious when we simulate the microwave background using the black box approach discussed earlier. This can be seen in Fig. 3.4(c) and Fig. 3.5(c) for the 3CP and 6CP devices. In the layout simulations for the measured device and when we consider the absence of wirebonds, we see the strong presence of spurious modes in the simulation band. The modes captured by the simulation for the measured device were also seen in measurements (not shown here) at nearly the same frequencies. To address this issue, we added more wirebonds in the simulation (layout not shown here) in places that were not experimentally accessible, i.e, at the meander bends and across the two floating ground planes in between connection points. We immediately see that this helps suppress the spurious modes. The ideal layout solution to this problem are airbridges [80]. Due to their compact size and smaller footprint than a wirebond, airbridges can be placed near the edges of the ground plane where the ground current is at its maximum. This helps in having a stricter microwave ground which helps in suppressing slotline modes. Although airbridges are a routine fabrication step in superconducting circuits [81], we did not implement them in our devices which are discussed in this thesis as the recipe was still under development. Nevertheless, we can simulate their effects by including them in our simulation models (layout not shown here).

The effect of the wirebonds and airbridges can also be seen on Γ_{10} as shown in Fig. 3.4(d) and Fig. 3.5(d) for the 3CP and 6CP devices respectively. We normalize Γ_{10} to the maximum simulated value and ω_{10} to the frequency where maximum Γ_{10} was simulated for the respective devices. We observe that the frequency where this happens is very close to the design value ω_λ^S discussed earlier in this chapter. The results indicate close match to theory with the simulated airbridges giving the best match. However, when we consider the layout of the measured device, it clearly deviates from the theoretical profile. We attribute this to spurious modes we saw earlier which modifies the background in a way to give a sharper Γ_{10} profile as a function of ω_{10}. For future device explorations using giant transmons, airbridges are the way forward.

3.2 Braided giant transmons

We will now focus on a device which consists of two giant transmons each with two coupling points to the TL. The transmons are connected in a braided configuration which is discussed in Chapter 2. The device will be referred to as BGT hereon. The highlight of the braided

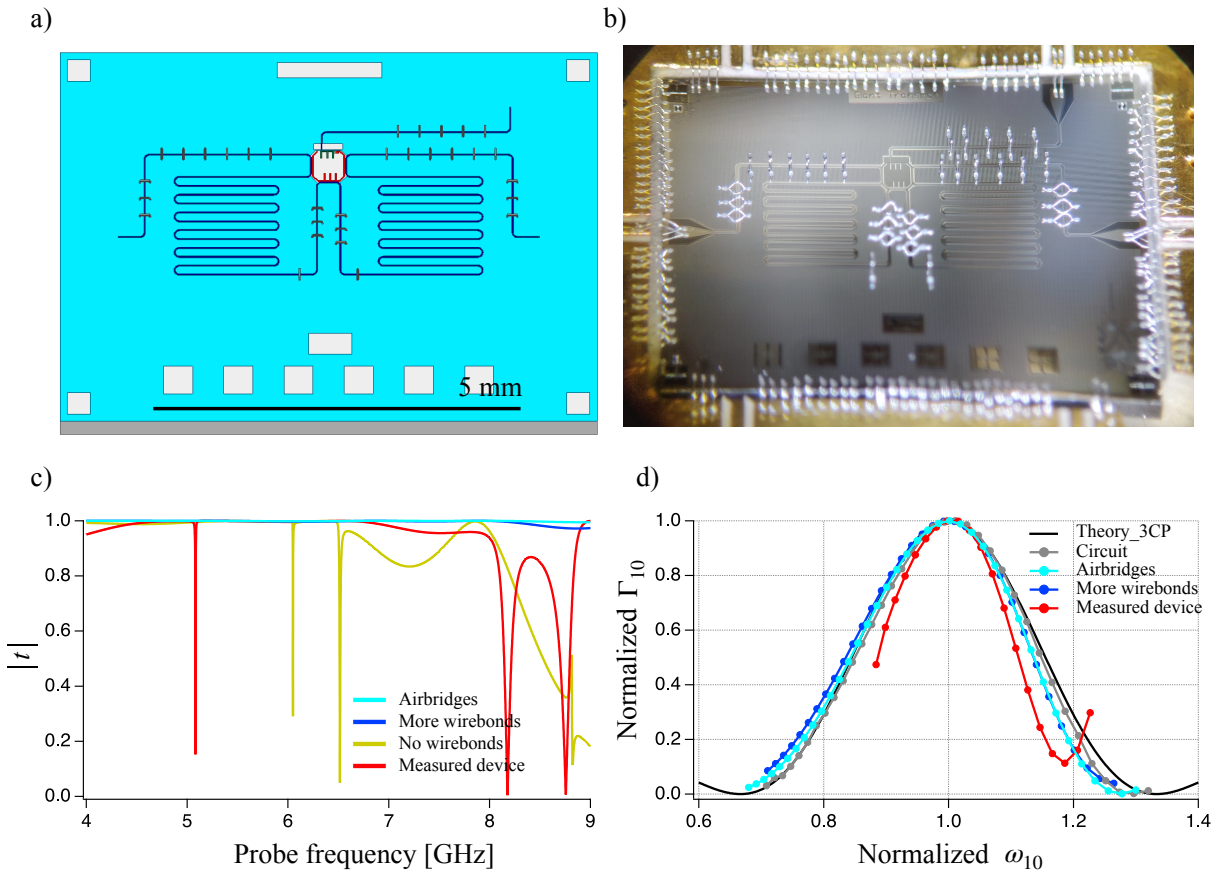

Figure 3.4: (a) HFSS model of the measured 3CP device. (b) Optical micrograph of the measured 3CP device. (c) Simulated t as a function of probe frequency for different scenarios as explained in the main text. For the device that was measured, we observe spurious modes in the simulation. Replacing the wirebonds with a high density of airbridges gave the best microwave background in the simulation. (d) Γ_{10} extracted by fitting the simulation results using Eq. 2.39, for different values of ω_{10}, which is obtained by varying L_J as shown in Fig. 3.1(e). The extracted Γ_{10} is normalized to its maximum simulated value and ω_{10} is normalized to the frequency where maximum Γ_{10} was simulated for each simulation variation. The simulation of the measured device shows deviation from the theoretical prediction.

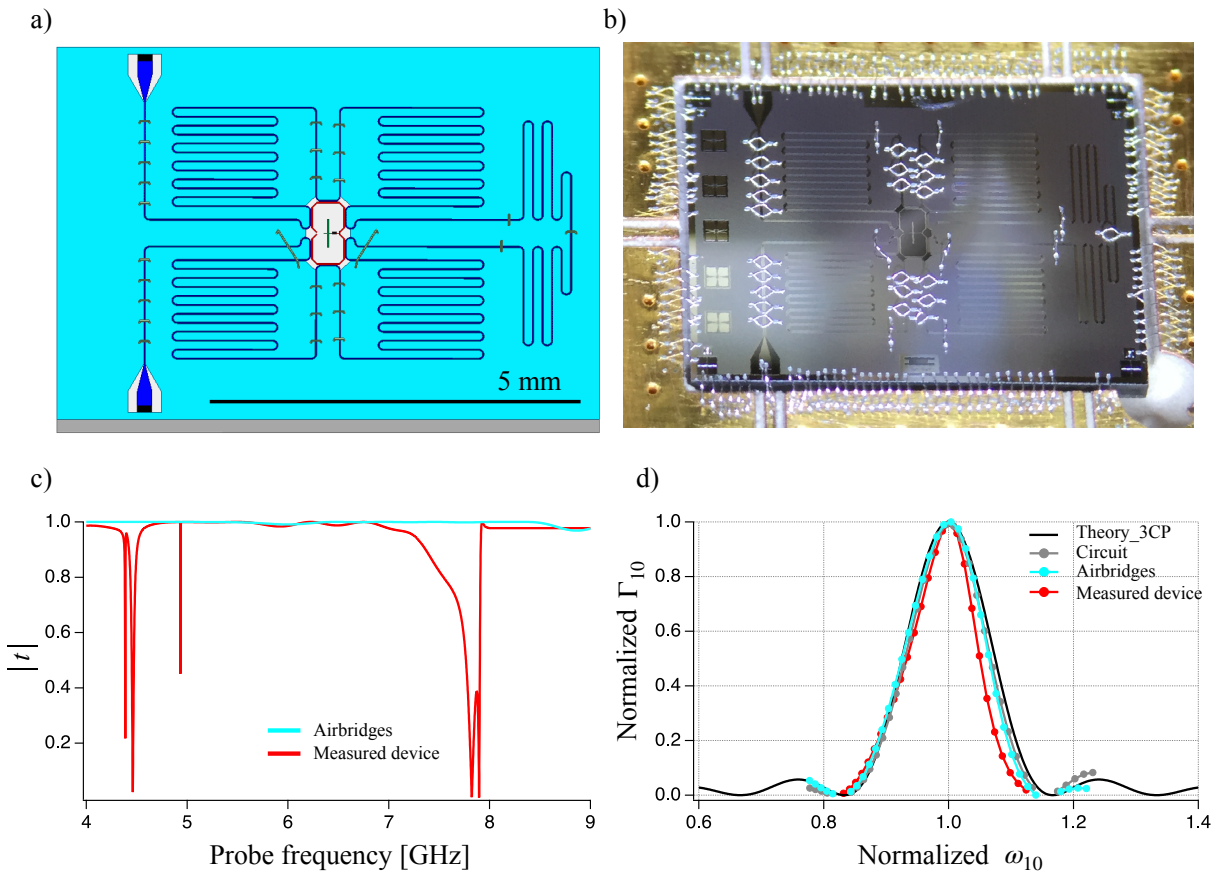

Figure 3.5: (a) HFSS model of the measured 6CP device. (b) Optical micrograph of the measured 6CP device. (c) Simulated t as a function of probe frequency for different scenarios as explained in the main text. For the device that was measured, we observe spurious modes in the simulation. Replacing the wirebonds with a high density of airbridges gave the best microwave background in the simulation. (d) Γ_{10} extracted by fitting the simulation results using Eq. 2.39, for different values of ω_{10}. The extracted Γ_{10} is normalized to its maximum simulated value and ω_{10} is normalized to the frequency where maximum Γ_{10} was simulated for each simulation variation. The simulation of the measured device shows deviation from the theoretical prediction, consistent with the trend that was observed in the 3CP device.

configuration is the availability of a decoherence-free interaction point, $\omega_\lambda^{\mathrm{B}}$ (superscript B refers to BGT device), in the frequency domain where the transmon's individual and collective decay into the TL is zero but they can still have a finite exchange interaction between them. We will explore the different design considerations and simulate the final device layout. Our simulations bring out some subtle effects that must be considered in order for the device to work in the right regime of operation.

3.2.1 Qubit parameters

For choosing the qubit parameters, a lot of the discussion which was presented earlier applies here as well. We target an $E_c/h = 500$ MHz for both qubits which is achieved using a similar electrode geometry as was used in the 3CP device. We use a global flux coil to tune the qubits over a wide range in our measurement bandwidth. Among many design variations considered, here we discuss a specific case, where qubit A has a separate voltage excitation line (X gate) and qubit B has a local flux line (Z gate), which is used to selectively tune the qubits into resonance with each other. Although both qubits have the same electrode geometry, their SQUID loop areas are designed to be different by a factor of 1.5. This was done to have the qubit resonance frequencies cross each other near $\omega_\lambda^{\mathrm{B}}$ using the global flux alone.

We first fix the inter-coupling distance between the connection points to be 5 mm. For the decoherence-free interaction between the qubits, the phase acquired by the photon between successive coupling points should be $\phi = \pi/2$ [28]. Using Eq. (2.41), this translates to $\omega_\lambda^{\mathrm{B}}/2\pi = 5.91$ GHz.

3.2.2 Microwave simulations

Circuit simulations

Our first check is to simulate an equivalent circuit model for the BGT device. This is shown in Fig. 3.6(a) with CPW TL components of length equal to 5 mm between the coupling points. The giant transmon qubits are replaced by their equivalent circuit deduced using the Maxwell capacitance matrix simulated in Q3DExtractor. Both qubits have the same capacitance matrix with the only free parameters in simulation being their SQUID inductance values, L_J^A and L_J^B for qubit A and B respectively. The results of the L_J^A parameter sweeps are shown in Fig. 3.6(b) where we plot the simulated $|t|$ for different values of L_J^A, with L_J^B chosen such that qubit B is out of the simulation band. The transmission spectra

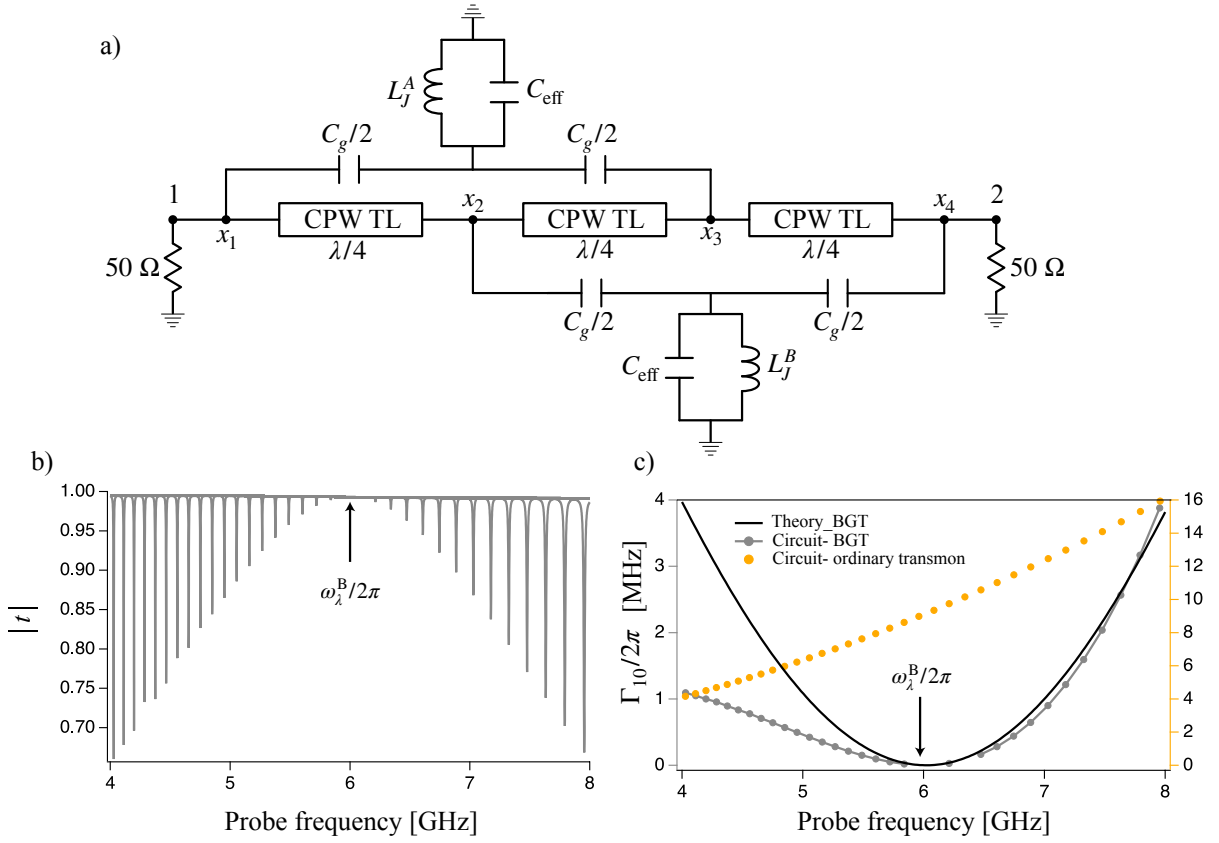

Figure 3.6: (a) Model of two giant transmons, each with two coupling points to a TL, connected in a braided configuration. We use this model for the performing ideal circuit simulation by treating the SQUID as a linear inductor. The values of C_g and C_{eff} are obtained from Maxwell capacitance matrix simulated in Q3DExtractor. (b) Simulated t for different values of L_J^A. The results are appended together, such that each dip in t corresponds to a different L_J^A. The qubit is decoupled from the TL at $\omega_\lambda^B/2\pi$ as expected. (c) Each transmission spectra is fitted using Eq. (2.39) to extract Γ_{10} and ω_{10}. At higher frequencies, the Γ_{10} follows the theoretical prediction but deviates at lower frequencies. We also extract Γ_{10} for the case of an ordinary transmon coupled to the TL at a single point. In this case, we see that $\Gamma_{10} \propto \omega_{10}^2$ which is confirmed by the classical model described in Section. 2.4.1. For the giant transmon, the strong deviation of Γ_{10} at lower frequencies could stem from this additional dependence on ω_{10}.

are appended together in the plot for clarity. As qubit A's resonance frequency is swept across $\omega_\lambda^B/2\pi$, we see that the dip in the $|t|$ changes indicating its frequency-dependent coupling behavior and the envelope of this behavior follows the theoretical prediction [27], with the minimum corresponding to $\omega_\lambda^B/2\pi$. The same behavior is expected from qubit B due to symmetry.

The model described by Eq. (2.39) takes into account dephasing, which is absent in simulations. Although the envelope in Fig. 3.6(b) follows the theoretical prediction, it does not explain the changing resonance linewidth as a function of frequency. To understand this, we use Eq. (2.39) and extract Γ_{10} by allowing the fit to account for dephasing. Figure 3.6(c) shows the extracted Γ_{10} for each of the transmission spectrum obtained by varying L_J^A. At higher frequencies, the Γ_{10} follows the theoretical prediction relatively well. At low frequencies, the values of the extracted Γ_{10} deviate from theory. This can be explained by considering the case of an ordinary transmon qubit coupled to TL at a single point (circuit not shown here). In doing this simulation, we keep C_Σ equal to that of the BGT device. Re-doing the same simulation by appropriately modifying the circuit, we see that Γ_{10} for an ordinary transmon shows a quadratic dependence with frequency as shown in Fig. 3.6(c). This becomes clear when we consider a classical model of an artificial atom coupled to a TL, which is discussed in Section. 2.4.1. For this case, we show that $\Gamma_{10} \propto \omega_{10}^2$.

In the theory simulations for both single [27] and multiple giant transmons [28], the intrinsic dependence of Γ_{10} with ω_{10} is assumed to be constant and so the frequency dependence for Γ_{10} only includes the interference effects. However, this is not true in practice as we demonstrate from our simulations. The strong deviation we see at low frequencies can be due to this intrinsic lower coupling. The total frequency dependence of Γ_{10} is then the sum of contributions from the active suppression from interference effects and also the quadratic dependence, which could explain the asymmetry in Γ_{10} we observe for the BGT device. We also observe this asymmetry in circuit simulations at low frequencies for the 3CP and 6CP devices discussed earlier.

Chip layout simulations

Following the black box approach discussed earlier, we simulate the layout of the device that was measured which is discussed later in Chapter 6. The HFSS layout and the measured device is shown in Fig. 3.7(a-b). The simulated transmission coefficient for the measured device does not show any spurious modes in the background. This is expected as the layout does not involve extreme meanders like the previous devices discussed earlier. The inductance L_J^A of qubit A is then swept in order to study its frequency-dependent coupling

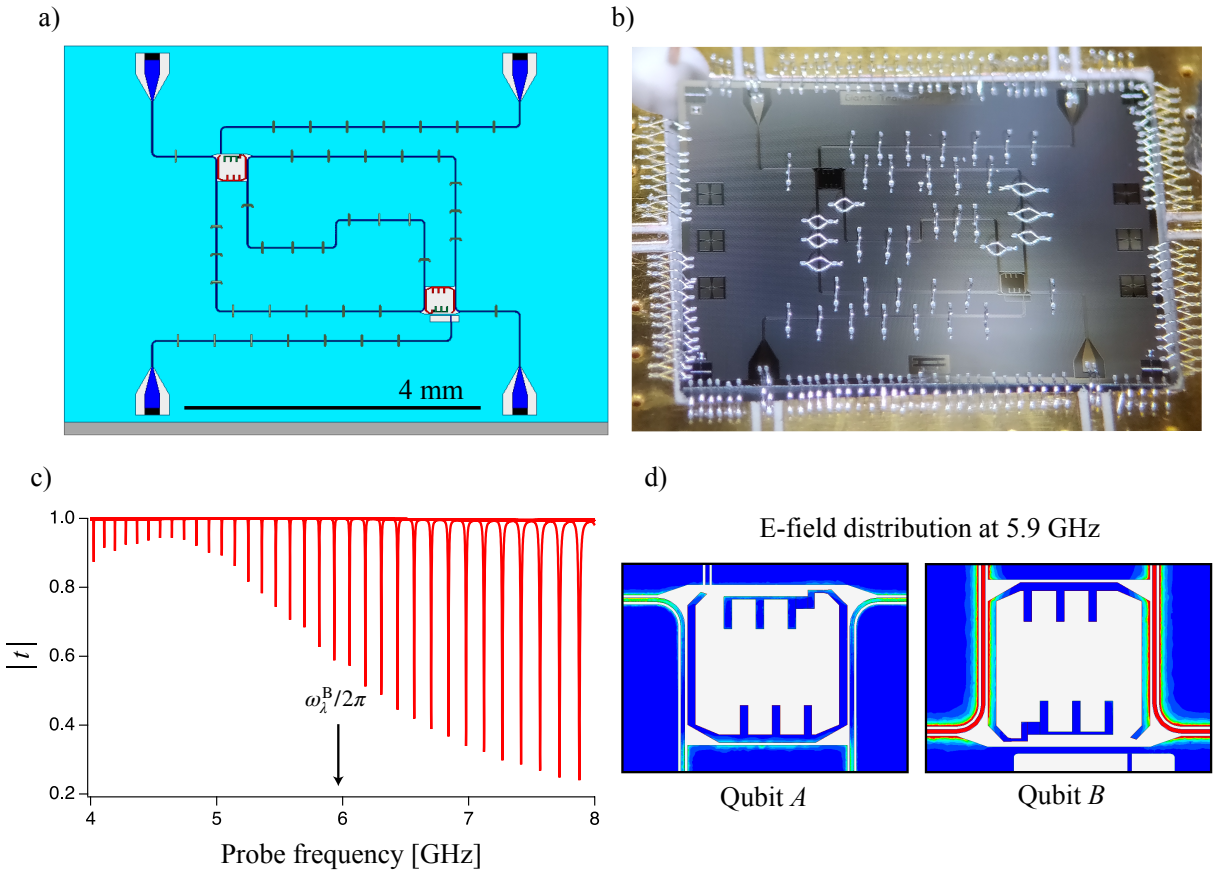

Figure 3.7: (a) HFSS model of the measured BGT device. (b) Optical micrograph of the measured BGT device. (c) Simulated $|t|$ as a function of probe frequency for different values of L_J^A of qubit A, with qubit B parked outside the simulation band. Qubit A decouples at a frequency much lower than $\omega_\lambda^B/2\pi$. (d) Electric-field distribution for qubits A and B at $\omega_\lambda^B/2\pi = 5.9$ GHz. The JJ in both qubits is modelled as a 50 Ω port. As the distance between the coupling points for each qubit is $\lambda/2$ at $\omega_\lambda^B/2\pi$, the braided configuration ensures that when qubit A is at a voltage node, qubit B is at a voltage antinode. The field at the coupling points of qubit B is phaseshifted by π. From the field simulation alone, both qubits should decouple at $\omega_\lambda^B/2\pi$ which contradicts the result obtained in (c). However, a closer view at the junction site reveals that there is still a finite field gradient across the junction at $\omega_\lambda^B/2\pi$ which causes it to couple to the to TL. This stray field gradient is generated by the ground currents near the vicinity of the junction. The asymmetry in the position of the junction could explain this discrepancy.

around $\omega_\lambda^B/2\pi$. The results are plotted in Fig. 3.7(c) which demonstrate a clear deviation from the expected theoretical behavior. The decoupling frequency is far below $\omega_\lambda^B/2\pi$ and understanding this will be the focus of the remaining simulation exercise.

The first check is to plot the magnitude of the electric field across different conducting surfaces as shown in Fig. 3.7(d) at $\omega_\lambda^B/2\pi$. The color indicates the magnitude of the field in the substrate where blue represents a low magnitude and red corresponds to a high magnitude. For clarity, only the field under the conductors is shown. The total distance between the two coupling points for each qubit is $\lambda/2$ at the designed $\omega_\lambda^B/2\pi = 5.91$ GHz which corresponds to a total phase $\phi = \pi$. Therefore, when the first coupling point of qubit A is at a node, its second coupling point will still be at a node. However, since the first coupling point of qubit B is symmetrically located between the two coupling points of qubit A due to the braided configuration (see Fig. 3.6(a)), the coupling points of qubit B will then be at antinodes, where the fields at the points are phase shifted by π. We can clearly see that this is the case from Fig. 3.7(d) which demonstrates that the layout of the TL is properly designed at $\omega_\lambda^B/2\pi$ and that both qubits should ideally be decoupled from an electric-field perspective alone. However, this does not explain the shifted decoupling frequency point we see in Fig. 3.7(c).

To explore this, we added a high density of airbridges to the device layout to see if this helps with minimizing ground currents close to the junction and thereby reduce the stray coupling across it. Fig. 3.8(a) shows the transmission coefficient spectra for the L_J^A sweep for qubit A. It is clear from the figure that adding airbridges helps to move the decoupling frequency closer to $\omega_\lambda^B/2\pi$. This further strengthens our hypothesis about the junction's stray coupling to ground currents which prevents the qubit from decoupling at $\omega_\lambda^B/2\pi$ as designed. As a final check, we move the position of the junction to the center of the transmon structure, symmetrically connecting across the two electrode islands, away from the ground plane and redo the simulation with the airbridges. The results are shown in Fig. 3.8(b) which agrees well with theory. The qubit decouples very close to the designed $\omega_\lambda^B/2\pi$ GHz. Bringing the junction to the center of the qubit is not a practical choice for exploring BGT devices as implementing a local flux line to selectively tune the qubits becomes difficult. But the simulations do give us valuable inputs on how to carefully design the position the junction for future designs such that the stray coupling to the junction can be minimized.

3.2.3 Simulating qubit-qubit resonant interaction

The simulation results of the measured device can also be used to study the scattering parameters of the TL when the qubits are brought into resonance with each other. These

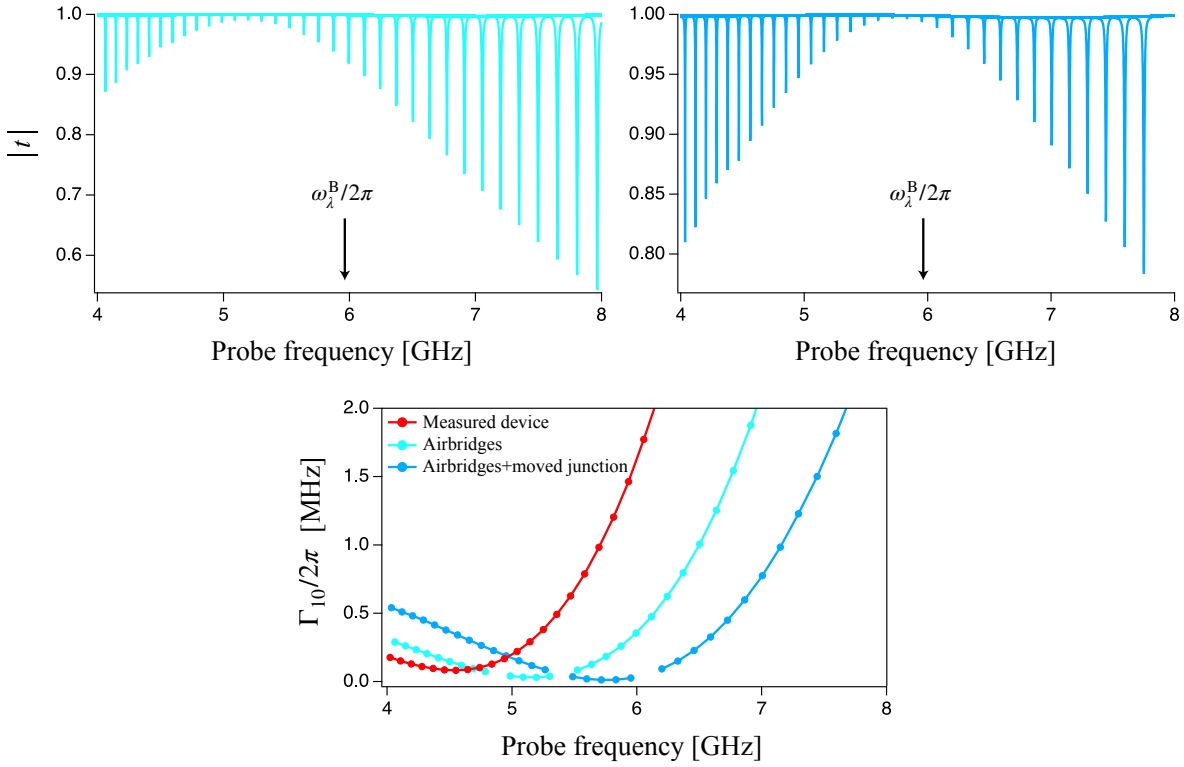

Figure 3.8: (a) Layout simulation for the BGT device showing $|t|$ as a function of probe frequency for a high density of airbridges. We immediately see that the simulated decoupling frequency moves closer to $\omega_\lambda^B/2\pi$. (b) As a final check, we move the position of the junction in the simulation to the center of the transmon structure, which connects to the capacitance electrodes symmetrically. The decoupling frequency is now very close to $\omega_\lambda^B/2\pi$, which supports our hypothesis about stray coupling of the junction to ground currents in its vicinity to be the main cause of the deviation of the simulation decoupling frequency from theory. (c) Simulated $\Gamma_{10}/2\pi$ as a function of probe frequency for different L_J^A extracted using Eq. (2.39). The different curves are labelled according to the nature of the layout simulation. In all three cases, we see the asymmetric dependence of Γ_{10} with probe frequency, strongly deviating at lower frequencies. The probable cause for this is explained in the main text.

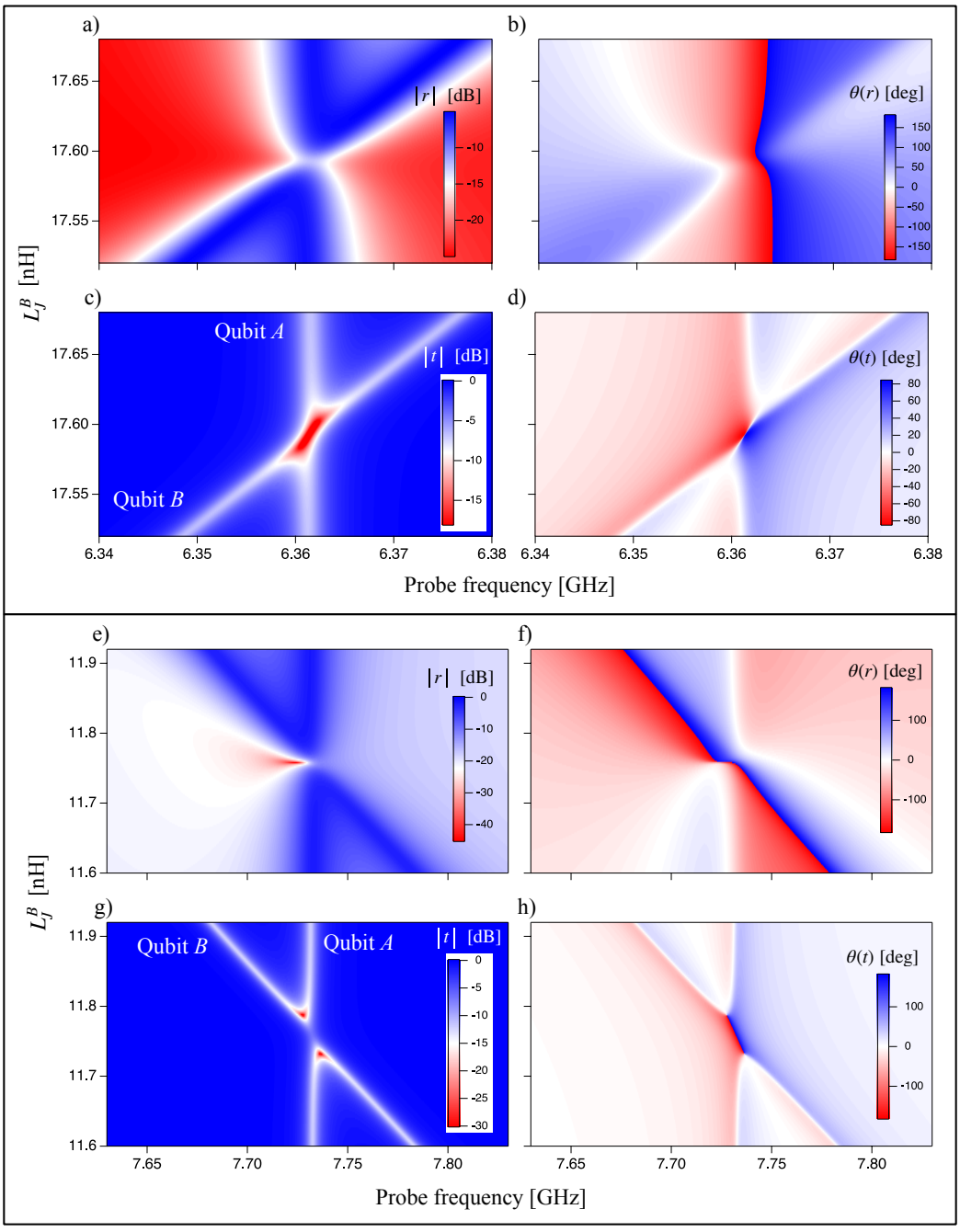

Figure 3.9: Simulation results showing magnitude and phase of r and t for the measured BGT device layout when the giant transmons are brought into resonance with each other. We do this at two frequencies, i.e, near 6.36 GHz and 7.73 GHz.

simulations are motivated by experimental results discussed in Chapter 6 where we observe non-standard resonant behavior of the qubits when measuring the transmission co-efficient at one of the frequency bias points. In Chapter 6, we compare the qubit-qubit resonant behavior by measuring the transmission coefficient at two different frequency points. So our goal here is to simulate both the reflection and the transmission coefficient of the measured device in HFSS near these points. In the simulations, qubit A has a fixed resonance frequency by keeping L_J^A constant and the frequency of qubit B is changed by varying L_J^B in order to bring both qubits into resonance with each other.

To simulate the response of the measured device we use the layout shown in Fig. 3.7(a). The simulated magnitude, $|r|$, and phase, $\theta(r)$, of the reflection coefficient (S11) together with $|t|$ and $\theta(t)$ of the transmission coefficient (S21) of the TL are shown in Fig. 3.9. This is done at 6.36 GHz (Fig. 3.9(a-d)) and 7.73 GHz (Fig. 3.9(e-h)). Although we do not measure r in the experiment, the simulated t qualitatively matches the measured results discussed in Chapter 6. We do not see an avoided level splitting signature of the qubits on resonance which is expected if the qubits are interacting through the TL. However from the transmission spectrum at 6.36 GHz, the qubits on resonance seem to merge as one effective qubit both in $|t|$ and $\theta(t)$ showing the strongest extinction in $|t|$ when compared to their off-resonant behavior. The interesting behavior is seen near 7.73 GHz where the qubits on-resonant show the strongest transmission with a disappearing $|t|$ but with a strong phase signature in $\theta(t)$. Understanding this in the context of giant artificial atoms remains an ongoing effort.

3.3 Parametrically-coupled superconducting cavities

We will now focus on the design aspects of parametrically coupled cavities which implement an optomechanical-like interaction discussed in Chapter 2. To implement this, we consider a high frequency quarter-wave ($\lambda/4$) resonator where one of its end is capacitively coupled to an input TL and the other end is shorted to ground via a SQUID. This forms a quasi-short boundary condition due to the low impedance of the SQUID which is $\sim$ 10-20 Ω from 4-8 GHz. The length of the $\lambda/4$ resonator dictates its resonance frequency which is chosen to be $\sim$ 5.5 GHz. The SQUID of the $\lambda/4$ resonator is placed near the current antinode of a low frequency half-wave ($\lambda/2$) resonator whose fundamental frequency is chosen to be $\sim$ 250 MHz.

In order to implement a photonic piston engine with this device, the main design goals are (a) to make the bandwidth of the $\lambda/4$ resonator to be equal to the fundamental frequency of the $\lambda/2$ resonator; (b) low bandwidth and thus high external Q factor for

the $\lambda/2$ resonator as it is used for photon storage; (c) frequency tunability of the $\lambda/4$ resonator which is achieved by the SQUID which also implements tunable coupling to the $\lambda/2$ resonator; and (d) prevent higher-order harmonics of the $\lambda/2$ resonator to interfere with the $\lambda/4$ resonator. The first two requirements are easily achieved by designing the coupling capacitors for the two resonators appropriately which sets the external Q factor discussed in Chapter 2. We use Q3DExtractor to design the inter-digitated geometry of the coupling capacitors. The third requirement is satisfied by fabricating a high-critical current SQUID which galvanically connects the $\lambda/4$ resonator to ground thereby implementing a tunable boundary condition as discussed in Chapter 2. However, achieving the fourth design goal needed a new approach to designing the low frequency $\lambda/2$ resonator where we integrate a band stop filter into the resonator itself.

3.3.1 Integrated microwave bandstop cavity

In Chapter 2, we discussed the $\lambda/2$ resonator using a TL which is capacitively coupled to the environment at its ends. By having sections of the TL with alternating low and high impedances, we can suppress the higher order modes of the cavity where the center frequency of the stop band is determined by the length of the alternating sections. The roll-off of the stop band is controlled by the number of sections, which also is bounded by the total length targeted to achieve the fundamental resonance frequency of the cavity. To develop these ideas further, we will simulate the cavity using ideal CPW TL components in ADS and the final layout simulation in HFSS.

Circuit simulation

We model the $\lambda/2$ resonator by constructing CPW TL components with alternating characteristic impedances. A unit cell comprises of a low impedance section with characteristic impedance Z_l which tapers into a high impedance section with characteristic impedance Z_h. A wide range of impedances can be designed by simply changing the width W and gap S of the CPW section. Each of these impedance sections is of length $\lambda_c/4 = 5$ mm where λ_c is the wavelength corresponding to center frequency f_c of the stop band which is chosen to be 6 GHz in our measurement band of 4-8 GHz. The resonator is coupled to the external environment using inter-digitated coupling capacitors C_c on either of its ends thus forming a $\lambda/2$ cavity. The equivalent circuit used for simulation in ADS is shown in Fig. 3.10(a). The effect of modulating the characteristic impedance of the cavity is shown in Fig. 3.10(b-c). Without modulation, i.e, when $Z_l = Z_h = Z_0 = 50\ \Omega$, we see the full spectrum of modes of the resonator. But when the modulation is turned on by setting

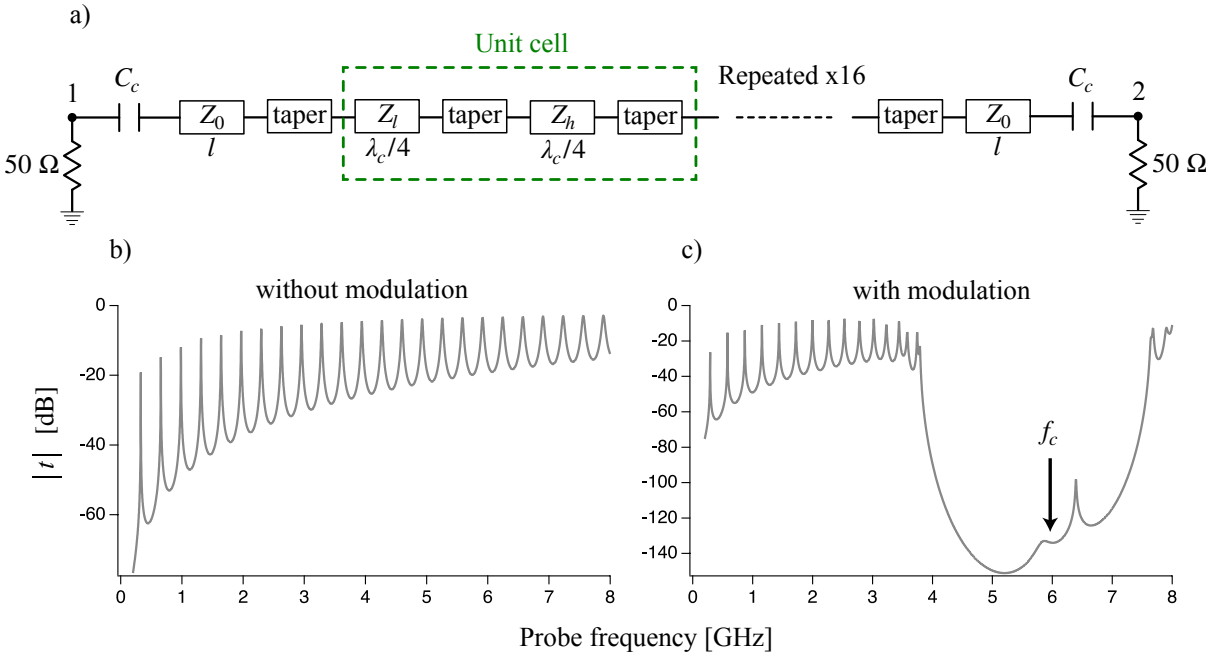

Figure 3.10: (a) Model of a band stop filter integrated as a $\lambda/2$ resonator for ideal circuit simulation. A unit cell consists of a low impedance section of length $\lambda_c/4$ and impedance Z_l and a high impedance section of length $\lambda_c/4$ and impedance Z_h. λ_c is the wavelength corresponding to the center frequency f_c of the stop band where the suppression of modes must occur. A taper section is added to transition the Z_l and Z_h sections, for matching the geometry of the center conductors. The total length of the resonator is divided into unit cells to achieve the desired total length of the $\lambda/2$ resonator. The bandstop behavior arises due to the modulating nature of the characteristic impedance of the $\lambda/2$ resonator. (b) Simulated t in dB units as a function of probe frequency without modulation, i.e, the characteristic impedance of the resonator is fixed at 50 Ω. We can see all the harmonic modes of the resonator in the simulation band. (c) When the modulation is applied by appropriately choosing $Z_l = 31$ Ω and $Z_h = 90$ Ω, we see a bandstop opening around $f_c = 6$ GHz, which was chosen for this simulation.

$Z_l = 31\ \Omega$ and $Z_h = 90\ \Omega$, we see a stop band around the designed frequency $f_c = 6$ GHz with excellent attenuation performance. The choice of Z_l and Z_h is determined by the minimum resolution that can be achieved in lithography during the fabrication process. The total length of the $\lambda/2$ resonator $l_{\lambda/2} = 178$ mm which should give us a fundamental frequency $f_{\lambda/2} = 332$ MHz which is achieved when there is no modulation. However the simulated fundamental frequency when the modulation is turned on is 290 MHz. We attribute this change to mode dispersion arising due to the modulation of the characteristic impedances as well as the loading from the coupling capacitors. For the simulations, we use $C_c = 130$ fF, which is simulated for the inter-digitated geometry using Q3DExtractor. Motivated by these results, we move on to the device layout simulations where a high frequency $\lambda/4$ resonator is parametrically coupled to the low frequency $\lambda/2$ bandstop resonator.

3.3.2 Device layout simulations

For the device layout simulations, we integrate the SQUID terminated $\lambda/4$ resonator with the $\lambda/2$ bandstop resonator. The interdigitated coupling capacitors for both resonators are included in the HFSS layout. Their geometry was optimized in Q3DExtractor to target a desired capacitance value. For resonator, we simulate $C_c = 160$ fF and for resonator B, $C_c = 130$ fF using their respective capacitor geometries. The SQUID is modelled as a lumped inductor whose value is set based on the target $E_j^{\max}$ which is calibrated during fabrication. A typical inductance value for the SQUID used in our coupled-resonator devices is ~ 500 pH. The resonators are coupled via coupling capacitors to the input and output feedlines using lumped 50 Ω excitation ports. The HFSS layout and the measured device are shown in Fig. 3.11(a-b). The measured device has a local flux line which was never used in the experiment. The layout simulation does not take this into consideration.

To characterize resonator A, we plot the phase, $\theta(r)_A$, of its reflection coefficient obtained from the single port S-parameter simulation in Fig. 3.11(c). The phase shows a strong overcoupled behavior, an intentional design choice motivated earlier. The resonance frequency is ~ 5.1 GHz, much lower than its bare frequency which is determined by its length. This is due to the strong capacitive loading of the resonator from its coupling capacitor as it is extremely overcoupled. The finite impedance of the SQUID also lowers the resonance frequency further. Resonator B is characterized by simulating its transmission coefficient obtained from a two port S-parameter simulation. Figure 3.11(d) shows $|t|_B$ as a function of probe frequency showing the fundamental resonance frequency of resonator B. The wideband nature of the bandstop behavior, which is seen in Fig. 3.10(c), is difficult to capture in HFSS as the convergence requirements are difficult to meet and hence is not shown here.

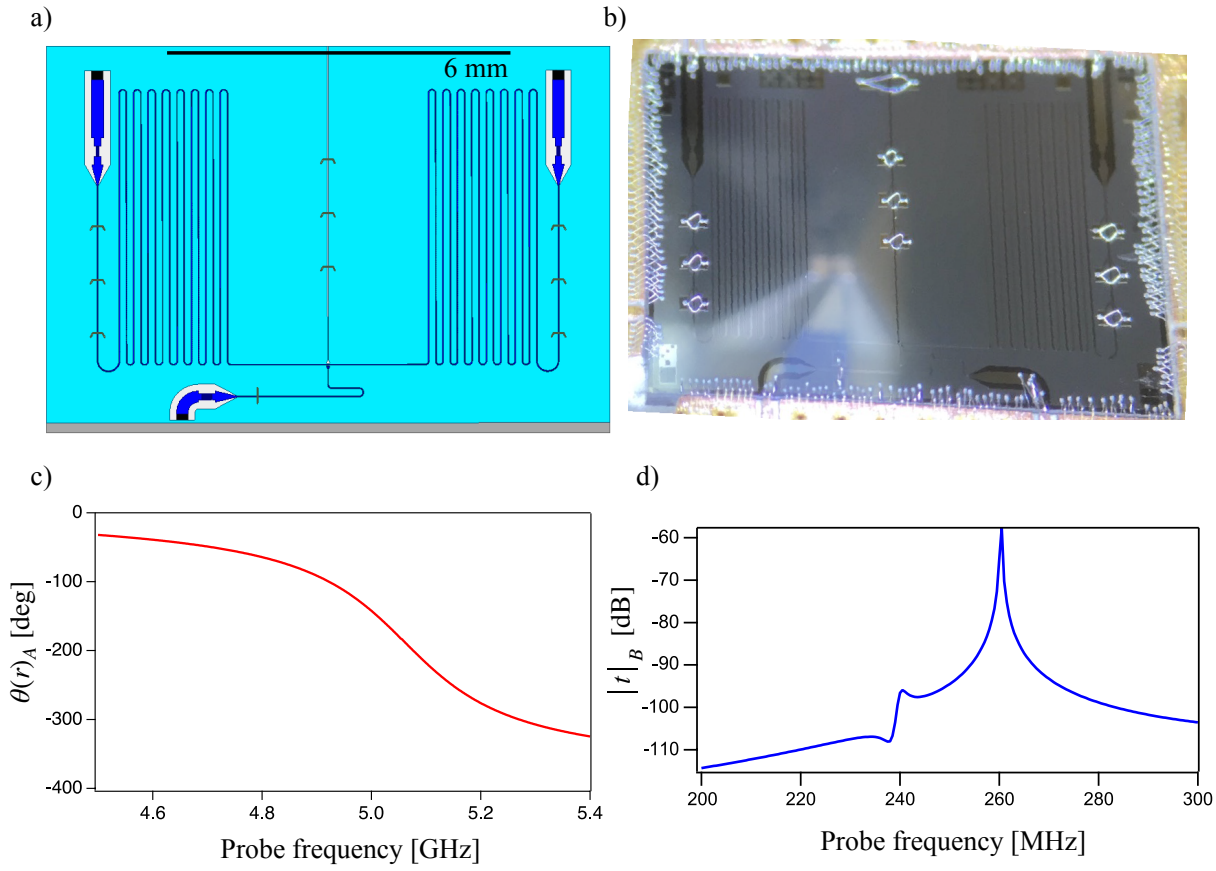

Figure 3.11: (a) HFSS model of the measured coupled-resonator device. (b) Optical micrograph of the measured 3CP device. (c) Characterization of resonator A by plotting its $\theta(r)_A$ as a function of probe frequency. The phase shows an overcoupled behavior of the resonator, necessary design choice for implementing a photonic piston. (b) $|t|_B$ as a function of probe frequency using the simulated transmission coefficient for resonator B. The plot shows its fundamental resonance frequency.

Chapter 4

Device fabrication and Measurement challenges

This thesis is based on work conducted on four devices which were studied in detail using simulations in the previous chapter. We now come to the part where these designs are realized into measurable entities using standard micro/nanofabrication techniques borrowed from the silicon IC manufacturing industry, but adapted to suit our needs. The advantage of working with superconducting circuits these days is that a lot of the processing involves fabrication techniques and recipes which are mature. The work presented in this thesis involved building on existing recipes and some which were newly developed to address the design challenges. In this chapter, we discuss the most relevant fabrication steps and the measurement challenges involved in characterizing the fabricated devices. For detailed fabrication recipes, please see Appendix A.

4.1 Fabrication process overview

Once the designs are validated using simulations, we proceed with transferring the CAD layout into a mask pattern which is encoded in a GDS file, a commonly used format in many lithography tools that will be used to transfer the pattern onto a substrate. Our devices are fabricated on a high-resistivity, intrinsic 4-inch silicon substrate with resistivity $\rho >$ 20 kΩ-cm and processed in a class 100-1000 cleanroom setting. Aluminum (Al) is our superconducting metal. We use the standard Dolan-bridge technique [82], to fabricate the Josephson junctions in an ultra-high vacuum (UHV) evaporator with a dedicated oxidation chamber. A typical fabrication run involves $\sim$ 25 steps and processes, all aimed at

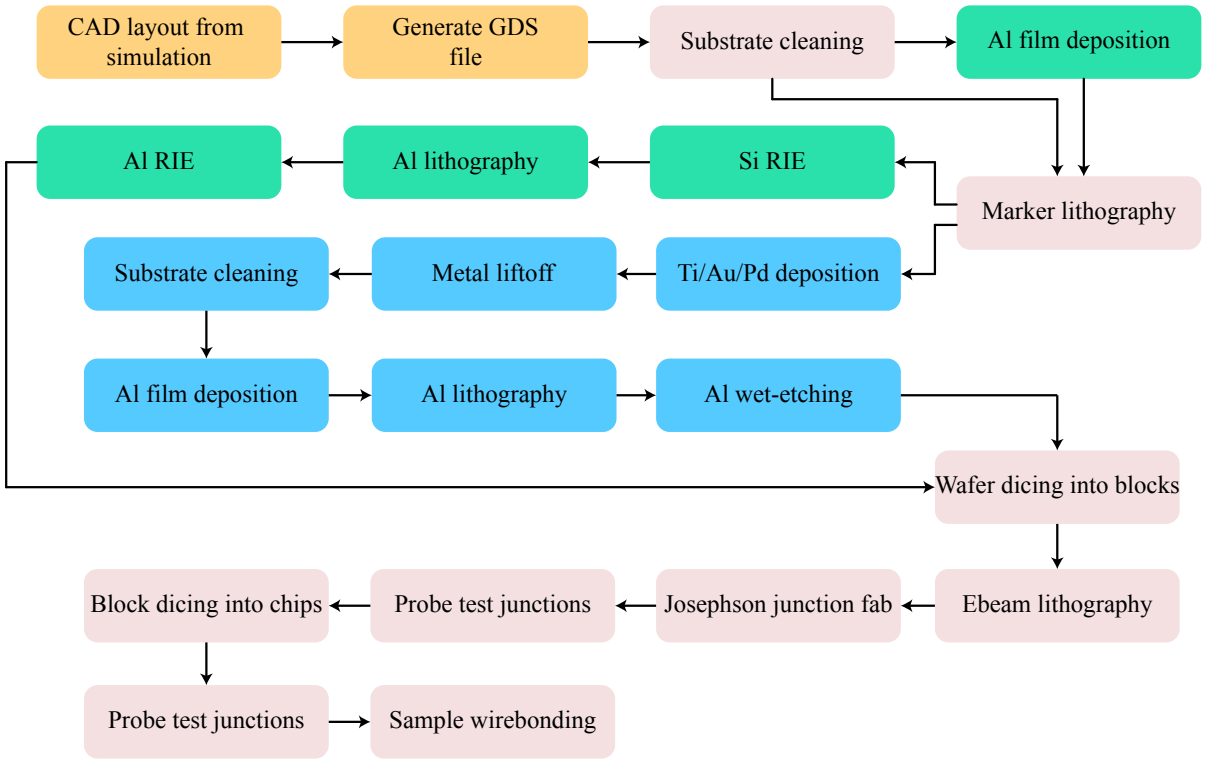

Figure 4.1: Fabrication process flow for the giant transmon and parametrically-coupled resonator devices highlighting the crucial steps. We begin fabricating devices once a design has been finalized and a CAD layout has been generated. The fabrication process typically starts with cleaning the wafer using a combination of acids to remove organic contaminants and the native oxide layer. This is followed by series of resist processing for lithography, metal film deposition, wet and dry processing steps, all aimed at transferring the CAD patterns into physical metal patterns on the wafer. Once the processing is complement on the wafer, it is then diced into smaller manageable blocks for ebeam lithography and Josephson junction fabrication. Once the junctions are successfully fabricated, the blocks are diced into individual chips, where a likely candidate is selected and wirebonded onto a PCB for measurements, thus completing its fabrication journey.

producing a reliable yield of devices based on the set design goals. We begin processing on a full wafer and then transition to a smaller, more manageable form factor (referred to as a block). Finally, the blocks are diced into individual chips which serve as potential candidate devices. Dedicated cleanroom wet-bench glassware are allocated where ever required to avoid cross-contamination with other cleanroom users. Figure 4.1 shows the overall process flow we adopt to fabricate devices. The detours in the flow are color coded separately to delineate between the giant transmon device (green) and the coupled-cavities device (blue) with the common shared fabrication steps indicated by pink. Fabrication recipes are prone to process variations that can arise due to changes in the cleanroom environment such as temperature, humidity, etc or it could originate in the equipment used to fabricate devices. At every step, careful inspection of the wafer/block/chip was done using an optical microscope to identify any potential issues with fabrication.

4.2 Wafer-level processing

Here, we will address key fabrication steps carried out at the wafer level. When working with these processes, we use a p-doped silicon wafer, a conventional, inexpensive wafer, as a test wafer alongside the high-resistivity process wafer. The fabrication steps are first performed on a test wafer, carefully inspected and when satisfied with the results, we repeat them on the process wafer. Over time, process variations on recipes can lead to variations in the obtained results. Using a test wafer helps to account for these variations in the actual process wafer.

4.2.1 Substrate preparation

Silicon forms a native oxide (SiO_x) on its surface which is detrimental to the devices we work with as it is a source of loss in the form of two-level systems (TLS) [69]. Several studies have modelled the various interfaces involved in a typical superconducting device, i.e, substrate-metal, substrate-vacuum and metal-vacuum interfaces. The results show that the substrate-metal and substrate-vacuum interfaces play a dominant role in the activation of TLS which amounts to decoherence [83,84]. Hence, obtaining a clean surface is the starting point in our fabrication process flow. We use a combination of acid chemical treatments on the process wafers as a first step. To remove any organic contaminants residing on the surface of the wafer, we use a piranha acid solution which is a combination of sulphuric acid (H_2SO_4) and hydrogen peroxide (H_2O_2). The piranha solution aggressively removes the organic contaminants and the resulting vapor products are highly dangerous

which demands extreme care in handling them. However, it does not remove the native oxide on silicon. For this we use diluted Hydrofluoric acid (HF) in a controlled-timed etch to remove the native oxide. To benchmark the efficacy of the cleaning procedure, we have separately measured superconducting resonators with low-power internal quality factor $Q_{\text{int}} \sim 1 \times 10^5$ and $Q_{\text{int}} > 1 \times 10^6$ at high-power. HF is easily the most deadly wet chemical in the cleanroom. Appropriate handling and disposing the chemical is paramount.

An easy way to find out if the oxide has been removed with HF is the de-ionized (DI) water test. Silicon oxide is hydrophilic but bare silicon is hydrophobic. When the etch is complete, it is useful to put droplets of DI water on the surface to see if they easily slide off. If they leave a trail behind, the etch is not complete. Although there isn't enough experimental studies detailing the time it would take the oxide to grow back, care should be taken to proceed to the next step quickly on a time scale of a couple of minutes. From the Fig. 4.1, for the giant transmon case, we immediately load the wafer into the loadlock of the evaporator which pumps down to 5×10^{-7} Torr within 10 min. This helps us to achieve a clean silicon surface prior to Al deposition. For the coupled-cavities device, we perform substrate cleaning again with HF eventually prior to Al deposition.

4.2.2 Alignment markers and ground plane crossovers

Alignment markers play an important role as a lithography guide when multiple patterns have to be written which require good alignment between the layers. They are usually patterned at the beginning so that all subsequent lithography patterns can be aligned to these marks. Therefore, a robust alignment mark that adheres well to the silicon substrate is desirable. Also, when patterns are written using electron-beam (ebeam) lithography, Josephson junctions for instance, additional requirements must be satisfied. For patterning the junctions, we use a 100 kV ebeam writer which is discussed later. Although Al works well for optical lithography, it cannot be used as an ebeam-alignment marker as the metal is largely transparent to the electron flux. Hence, the typical choice of metals for ebeam markers are high-Z metals like gold (Au), palladium (Pd) and platinum (Pt), which are visible under the electron beam due to their high atomic weight which increases their scattering cross section. However, the contrast of visibility depends on the thickness of the marker metal and the energy of the electron beam. For our giant transmon devices, we use alignment marks etched in the silicon substrate using a standard Bosch RIE process. We find that a 4 μm etched silicon trench works well as an ebeam alignment mark. For the coupled-cavity device, we developed a trilayer marker recipe consisting of titanium (Ti), Au and Pd.

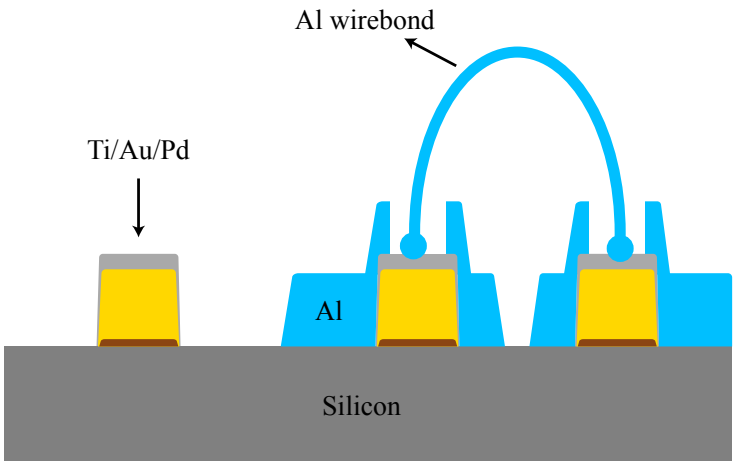

Figure 4.2: Ti/Au/Pd trilayer process for alignment marks and for connecting floating grounds for the coupled-cavities device

The trilayer process specific to the coupled-cavities device has three advantages. Firstly, Ti is added to improve adhesion of the metal stack with the substrate. Secondly, it is used to fabricate the markers required for optical and ebeam lithography which is shown in Fig. 4.2 as an isolated metal stack. Thirdly, Au has a higher atomic weight than Pd and so adding it as an intermediate layer reduces the effective metal thickness required to achieve a good contrast during ebeam lithography. Without Au, the Pd required would be ~ 2 times the thickness of Au. This also helps in bringing down the thickness of the metal stack to values similar to the Al film, which we do not change in the recipe. The use of a capping layer of Pd is motivated below.

Finally, in the design of the $\lambda/4$ cavity, the SQUID galvanically contacts the ground plane in order to have the strongest coupling with the $\lambda/2$ cavity. This presents an issue when we have to electrically connect the different floating ground planes on chip using Al wirebonds as they would result in superconducting ground loops of which the SQUID is part of. The circulating currents generated in the ground planes as a result of flux biasing the SQUID would interact with it resulting in undesired parasitic tuning of the SQUID. One could use Au wirebonds instead but this would result in the formation of "purple plaque", an intermetallic Au-Al compound, resulting in poor-ohmic contacts [85]. In order to break these prospective superconducting loops, we use the trilayer stack as a normal metal pad to connect the different floating ground planes for the coupled-cavities device. The disconnected Al ground planes are shown pictorially in Fig. 4.2 as blue islands which

are connected together using Al wirebonds. The bonds contact the Pd top layer of the metal stack through a pocket patterned during Al lithography. The Al film is evaporated at an angle with rotation which gives a good conformal coverage on the trilayer pad. For the giant transmon devices, the SQUID is electrically isolated from all the ground planes and hence Al wirebonds were directly used to connect the floating ground planes.

4.2.3 Choice of optical resists

The choice of resist for optical lithography depends on the how the resist pattern would be transferred to the metal layer. Typically, this is done using additive or subtractive transfer techniques. In the additive process, popularly known as the lift-off process, the metal is deposited on a patterned resist. The metal film adheres to the substrate in places where the resist has been developed away. The undeveloped resist, which is coated with the metal film, is then washed off using a suitable solvent, leaving behind a patterned metal layer. In order to aid this process, a typical choice is to use a bilayer resist stack, which in our case is formed by S1811 as the top layer and PMGI SF7 as the bottom layer as shown in Fig. 4.3(a). The top layer is sensitive to light and hence serves as an imaging layer defining the pattern. The bottom layer, being more sensitive, is overexposed to mainly provide an undercut which helps the metal film to liftoff easily. Without the undercut, the film would deposit on the resist sidewall making liftoff difficult. For the subtractive process, the patterned resist is on top of a metal film. The metal is then etched using wet or dry processes in places where the resist has been developed away. The remaining resist serves as a physical mask to prevent the metal underneath it from being etched away. In this case, a single layer of S1811 is used as an etch mask as shown in Fig. 4.3(b).

For the coupled-cavities device, we use a liftoff-process to pattern the trilayer alignment markers/crossovers and pattern the Al metal film by wet etching it using Transcene's Al Etchant type-A solution. For the giant transmon devices, we use a dry metal RIE technique to etch the Al film.

4.2.4 Wafer lithography

To pattern the resist for optical lithography we use a maskless aligner (MLA) from Heidelberg Instruments which directly writes the desired pattern onto a resist-coated substrate. In the past, we used mask aligners for fabricating devices but switched to the MLA after it was commissioned in the cleanroom. The advantage with MLA over traditional mask aligners is the absence of a physical mask, which needs to be fabricated separately by

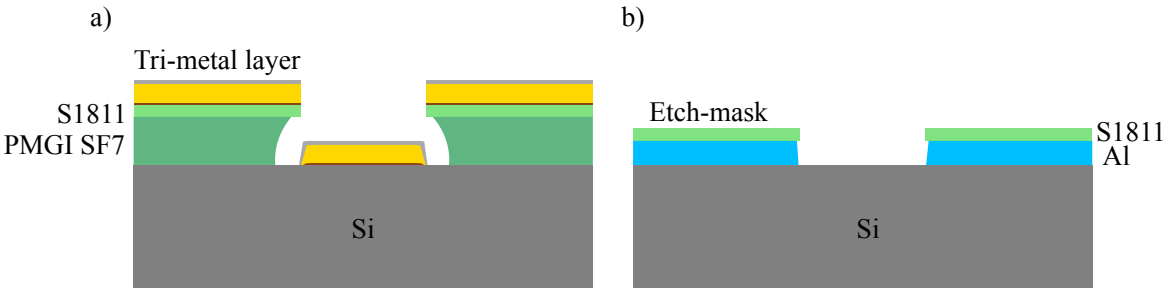

Figure 4.3: Choice of resist for optical lithography for (a) liftoff and (b) wet/dry etch processes. The illustration is not drawn to scale.

a third party. This helps with iterating designs on the fly. The MLA also offers better resolution ($\sim$ 800 nm) with minimal offsets ($\sim$ 500 nm) during overlay exposures using automated alignment mark detection routines. The machine converts the GDS layout into a proprietary format which is then written at a dose which was optimized to minimize over development of the resist after exposure. A typical exposure time on a 4-inch wafer is 18 min. The alignment marks and the Al film for all devices discussed in this thesis were patterned using the MLA.

4.3 Block-level processing

Once the markers and the Al film are patterned, the wafer is diced into 24x24 mm^2 blocks. A process wafer yields a total of 9 blocks and each block has an array of 6 chips. A block is used to fabricate Josephson junctions for all the 6 chips using ebeam lithography. We will briefly discuss the details of junction fabrication in this section.

4.3.1 Ebeam-lithography

We use the JEOL JBX-6300FS ebeam lithography system to pattern the Josephson junctions. This is a 100 kV system with capabilities of writing over a full 6-inch wafer or on arbitrarily small samples using appropriate holders. The block-level GDS pattern file is converted to job files for the JEOL which has additional information such as ebeam dose, beam step size during exposure, proximity error-corrected dose factors for the pattern, coordinates of the global and local alignment marks, etc. Prior to exposing the resist

with this tool, several calibration routines are manually run in order to account for beam alignment, drift, electromagnetic interference in the beam deflector coils, alignment mark detection etc. Once the calibration routines are done for every beam current that will be used for writing, the exposure is begun by running the appropriate job files. We use a lower current ($\sim$ 2 nA) for writing small features such as the SQUID and a larger current ($\sim$ 4 nA and $\sim$ 20 nA) for the larger features such as the transmon's capacitance electrodes and the resonator's coupling capacitors. Any alignment offset we observe from the MLA exposure discussed earlier between the marker pattern and the Al film pattern is taken into account during the ebeam exposure of the junction patterns.

4.3.2 Josephson-junction fabrication

The Josephson junctions are fabricated using a lift-off process. We choose a bilayer resist stack to aid the lift-off process. We use MMA-MAA EL11 copolymer or PMGI SF11 as an underlayer resist depending on the device being fabricated. The top layer which is the imaging resist should offer high resolution to ebeam exposure. PMMA or ZEP (diluted in Anisol) is used as the imaging layer. For the coupled-cavity device, we use PMGI SF11 and PMMA A3. For the giant transmon devices, we use MMA-MAA EL11 and ZEP. The resist stack in our devices also benefit from being selective to the developer solution.

Once the pattern is written and the resists developed, the block is loaded to a UHV Plassys evaporator. This equipment has a separate loadlock, evaporation chamber and an oxidation chamber. The loadlock is able to pump down from atmosphere to 5×10^{-7} Torr in 10 min. The base pressure of the evaporation and oxidation chamber is $\sim 5 \times 10^{-9}$ Torr and $\sim 6 \times 10^{-10}$ Torr respectively. Robot arms can move the sample between the chambers without having to break the vacuum. The ultra-high vacuum environment enables us to make high quality devices and junctions. The loadlock chamber has an ion gun which is used to etch the native oxide on Al in order to make galvanic contacts. The tiltable sample holder stage in the evaporation chamber enables double-angle evaporation of Al to make junctions.

The shadow evaporation technique, also known as the Dolan-bridge technique, is used to fabricate the Al Josephson junctions in our devices [82]. The technique is illustrated in Fig. 4.4(a-b). The resist stack is patterned in a way such that a part of the top layer is suspended, forming a shadow mask. When evaporating Al at two angles as shown, an overlap, o, between the metal layers is formed which to first order can be written as:

$$o = 2t\tan(\theta) - w, \tag{4.1}$$

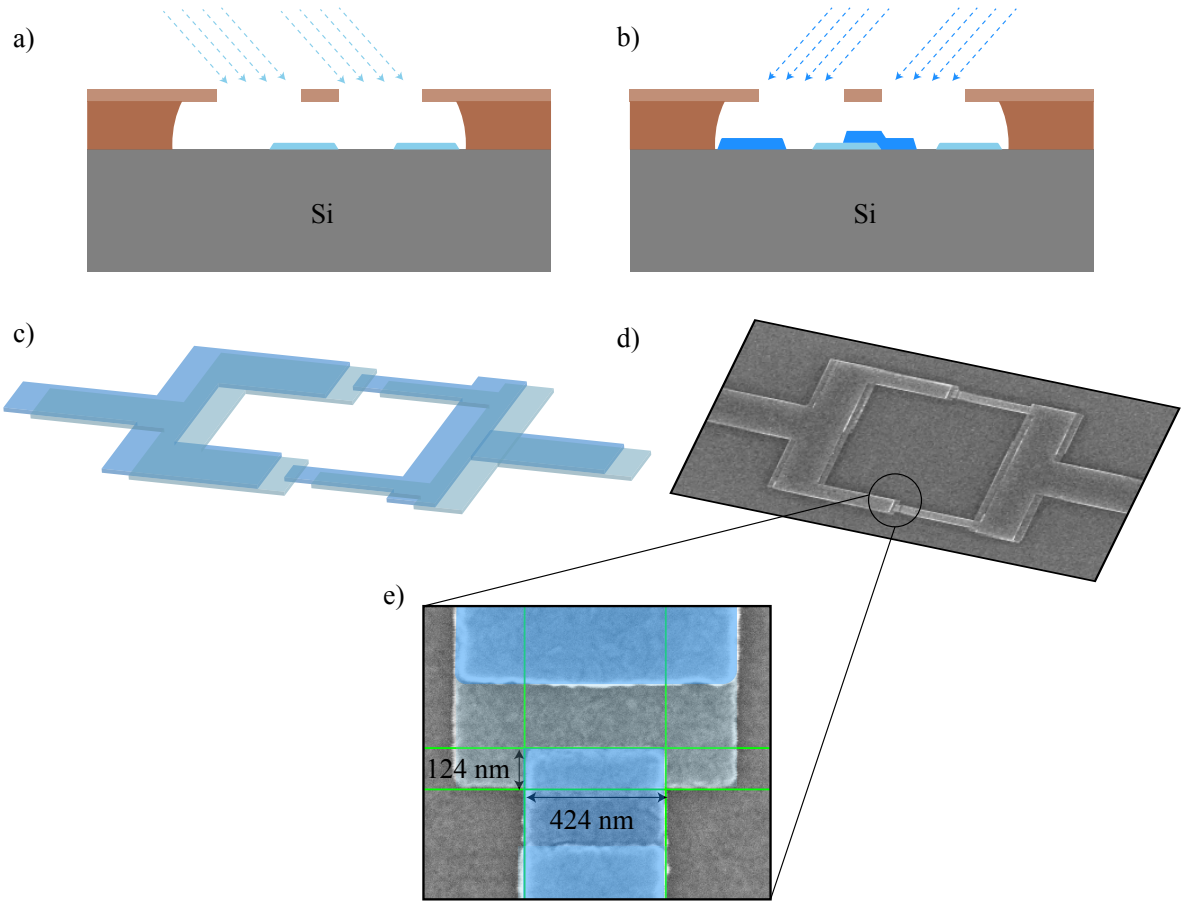

Figure 4.4: (a) and (b) showing the double angle evaporation for fabricating Josephson junctions using the Dolan-bridge technique. (c) A cartoon of a typical SQUID showing the overlapping metal layer which form the junctions. (d) A scanning electron micrograph of a SQUID fabricating using the Dolan bridge technique. (e) False-colored close up of the SQUID showing the junction with typical dimensions for fabricating qubits.

where t is the thickness of the bottom resist, θ is the tilt angle of the substrate holder with respect to the horizontal and w is the width of the suspended resist. This expression is true when the thickness of two metal layers is small when compared to t.

When a controlled oxidation step is introduced between the two evaporation steps, we get a Josephson junction. The rate of oxide growth on the Al film depends on the oxidation pressure and the oxidation time [86]. This is done by moving the sample from the evaporation chamber to the oxidation chamber after the first angle evaporation. We use static and dynamic oxidation depending on the device being fabricated. For static oxidation, oxygen is bled into the chamber up to a certain target pressure. In the dynamic case, the flow is continuously monitored to maintain a fixed pressure in the chamber while it is also continuously pumped. Dynamic oxidation is more reproducible when lower pressures are desired, thus helps with achieving a thinner oxide for making high critical current junctions. The sample continues to stay in the oxygen environment for a calibrated time before it is brought back to the evaporation chamber for the second angle evaporation. Typically the thickness of Al for making our junction is 40+60 nm from the two evaporation steps. Once the oxide barrier is capped by the second evaporation, we transfer the sample back to the oxidation chamber where a final high pressure oxidation forms a self-limiting oxide layer on Al. We believe that creating this oxide in a clean environment is better than having it form in ambient conditions when the device is removed from the evaporator. Finally, the evaporated block is left overnight (10-12 hours) in solvent for lift-off under cleanroom ambient temperature conditions. We find that this process gives us better lift-off than doing it in a hot solvent for a few hours. Fig. 4.4(c) shows a illustration of a SQUID pattern that is obtained following double-angle evaporation. A scanning electron microscope (SEM) image of a fabricated SQUID device with a false-colored close up of the Josephson junction is shown in Fig. 4.4(d-e).

4.3.3 Measuring junction resistance

Once the lift-off is complete, we probe test junctions by measuring their room-temperature resistance. The test junctions are exact copies of the device junctions in the chip designs. These are placed across the chip and measuring the resistance of all of the test junctions in the block helps us to benchmark the process variation in the junction fab. We observe that our junctions are quite uniform with about $2-5$ % variation in the measured resistances. The room-temperature resistance gives us an estimate of the critical current of the junction, as discussed in chapter 2. After the resistance checks, we spin-coat the block with $3-4$ μm of SPR, a UV resist which is used to protect the block when dicing.

4.4 Chip-level processing

After the block has been diced into individual chips, we remove the protective resist from them using Acetone and IPA. During the spin coating step of SPR, we bake the block at 110^0 C for 90 s. We noticed that the resistance of our junctions increased during this step by $\sim 8 - 10$ %. We can factor this change by modifying the junction geometry accordingly. However, for the devices discussed in this thesis, this change is insignificant. Finally, the chips are inspected in an optical microscope and the best candidate is selected for cooldown.

4.4.1 Sample preparation and wire-bonding

To prepare the sample for cooldown, first it has to be wirebonded to the PCB which is housed in a sample box made out of Au-plated oxygen-free copper (Cu). A pocket is milled in the PCB such that the sample is flush to the top of the board. To glue the sample in place, we use a dab of Apiezon N-grease, which is cryogenic and vacuum compatible and thermally conducting. Once this has dried, we proceed to wirebonding the sample. We use a semi-automatic bonder with calibrated bond settings to place a high density of Al wirebonds across the chip and the PCB. Optical micrographs of the wirebonded devices are shown in chapter 3. The sample is now ready for low-temperature characterization.

4.5 Challenges with low temperature measurements

In this section, we present the details of the measurement setup implemented to characterize the devices presented in this thesis. The challenges associated with probing superconducting devices are plenty. These mainly fall under the category of device operating temperature, employing better thermal and noise filtering techniques, routing signals to and from the cryostat, shielding from electromagnetic interferences (EMI), protecting the device from stray magnetic fields, among many others. We discuss some of these issues and the measures taken to improve the general microwave hygiene of our setup.

4.5.1 Printed circuit board (PCB)

We work with Rogers 3010 laminate as our PCB material, which has a dielectric constant of 10.2 and a low dissipation factor in our measurement band. The high dielectric constant of the PCB, ensures close matching of phase velocity of microwaves with the silicon substrate.

The ground planes on the front and back of the PCB are connected using copper-plated through holes. The PCB is coated with a soft gold finish without a nickel (Ni) intermediate layer during the electroplating process. This ensures the absence of magnetic impurities that could have been present if Ni was used. The soft gold also improves the adhesion of the wirebonds on the surface of the PCB. The CPW launches on the PCB are geometrically matched to those on the chip to ensure a smooth 50 Ω transition. To minimize reflections due to the wirebonds connecting the two CPW center conductors on the PCB and the chip, its length is kept as short as possible. A general rule of thumb for wirebond inductance is 1 nH/mm, and typical wirebond length in our devices is $\sim 0.5 - 1$ mm. In preparation for the measurements that follow, we highlight some of the main challenges of low-temperature characterization and the steps taken to address them.

4.5.2 Operating temperature and device thermalization

The devices must be cooled down to temperatures below the critical temperature T_c of the metal for superconductivity to persist. Aluminum, which is the choice of metal in our devices, has a $T_c = 1.2$ K. However, to operate devices in the quantum regime, the average thermal energy $k_B T$, where k_B is the Boltzmann constant and T is the temperature, has to be much lower than the energy of the photons $\hbar\omega$ used to probe the devices, typically in the $4 - 8$ GHz band. To achieve $k_B T \ll \hbar\omega$, we use a commercially available dilution refrigerator from Bluefors, capable of achieving a base temperature of ~ 8 mK. The wirebonded device encapsulated in a sample box, made out of gold-plated oxygen-free high-conductivity copper (OFHC), is then mounted onto the base plate of the dilution refrigerator using an OFHC mounting bracket as illustrated in Fig. 4.5(a). Operating devices at such low temperatures ensures that the residual thermal excitations from the background are suppressed, leading to a lower probability of quasi particle formation, a known source of loss in superconducting circuits [87].

Achieving a low operating temperature with the dilution refrigerator does not guarantee that the sample is also thermalized to the same temperature. The efficiency of cooling the sample depends on many factors. The bulk of the cooling comes from the wirebonds that connect the sample and the PCB. Apiezon N-grease, which glues the sample to the PCB, also aids in this cooling. The PCB gets cooled by the sample box and the edge-mounted SMA connectors, which is discussed later when reviewing the sample-box design. As the sample box is directly mounted onto the OFHC bracket of the base plate, the contact areas of the two surfaces needs to be well-polished. To further improve the thermal conductivity across these areas, a dab of N-grease is applied to fill out any gaps created by micro ridges in the surface profile.

4.5.3 Sample box design

The first level of electromagnetic shielding for the device is provided by the sample box, which acts as a Faraday cage. For the devices studied in this thesis, a new sample box was designed, combining the simplicity of machining and assembly while providing efficient thermalization of the sample. The CAD layout, together with the machined sample box prior to gold plating, is shown in Fig. 4.5(b-e). The box has access to six ports, which are connectorized using edge-mountable female SMA bulkhead connectors from Fairview Microwave, which are rated from DC-18 GHz. The connector dimensions are chosen such that the diameter of its center pin matches the PCB center trace width with the edge-mount gap allowing the PCB to fit snuggly with the connectors, as shown in Fig. 4.5(e). A small pedestal, separately machined, holds the PCB in place while providing the necessary thermalization with the rest of the sample box. Once the parts are assembled, the center pin and the ground prongs of the connectors are soldered to the PCB. The lid of the box is machined with lips to ensure that the volume of the hollow cavity inside the box is mostly set by the PCB's lateral dimensions and the height controlled by the gap between the lip and the PCB. The Eigenmode simulation in HFSS (not shown here) of the inner rectangular cavity confirms that the lowest TE101 mode is outside the measurement band. The simulation also includes the effect of the PCB, which tends to bring down the mode frequency resulting from dielectric loading.

Finally, to generate an external magnetic field, the sample box is mounted with a custom made solenoid coil which helps in tuning the resonance frequency of the qubits and the $\lambda/4$ cavity in our experiments. The leads of the coil extend up to room temperature, properly thermalized at each temperature stage of the dilution refrigerator, in a twisted-pair configuration to minimize the pickup of flux noise. At room temperature, we current-bias the coil using a suitable series resistor ($1 - 10$ kΩ) at the output of a voltage source. The series resistor is housed in a metal box with capacitors (10 μF) connected across the coil leads in a π network to implement a low pass filter which results in a cut-off frequency of a few Hz. This further helps in reducing noise riding on the coil leads, for instance digital noise emanating from the voltage source.

4.5.4 Thermal, superconducting and Mu-metal shielding

The microwave frequency range used in superconducting circuit experiments ($4 - 8$ GHz) also supports other communication channel bandwidths, mobile phones for instance. Hence, shielding from these signals is important. The sample box does well protecting the device as the first level of defense against unwanted EMI in a practical experimental setting.

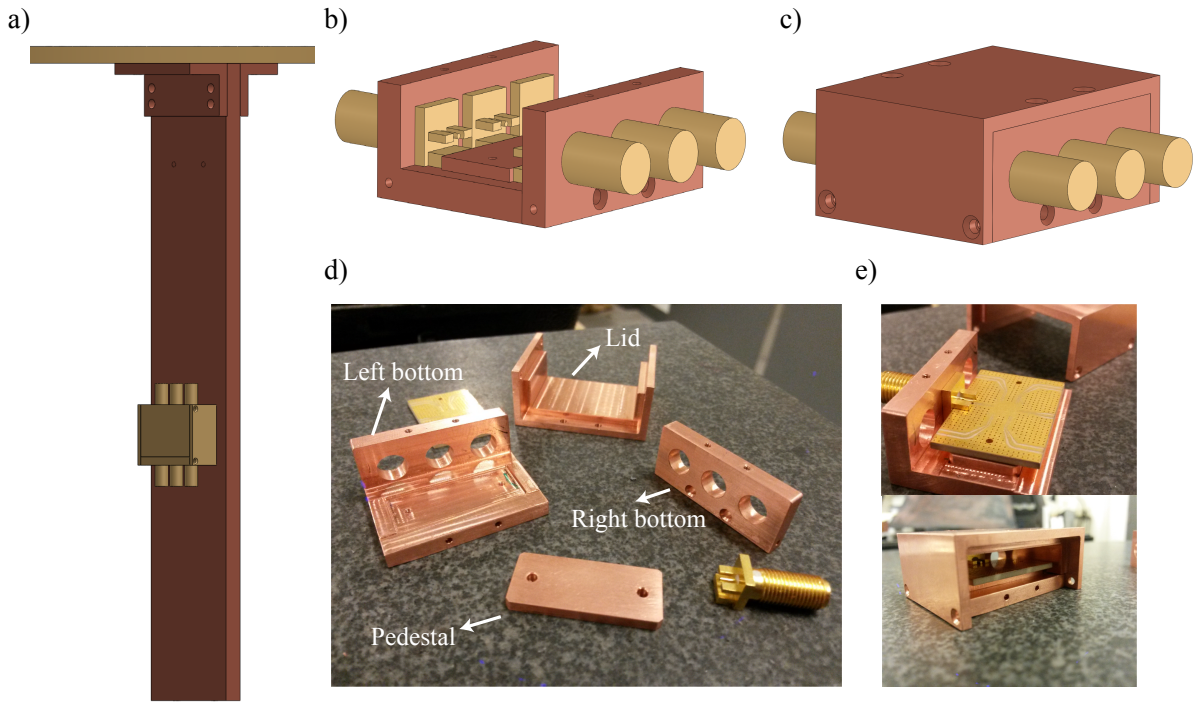

Figure 4.5: (a) CAD drawing of the sample box used in this thesis. The box is mounted to a cold finger which in turn is attached to the base plate of the dilution refrigerator. (b) and (c) shows the sample box design with assembles parts. The SMA edge-mountable female connectors for the box are shown for illustration purposes. (d) Parts of the sample box after machining. (e) The PCB is edge mounted and sits on top of a pedestal which cools the PCB from the bottom. The bottom image shows the cross-section of the box without the right bottom part.

Objects also emanate thermal black-body radiation given their physical temperature, a detrimental effect to superconductivity. The higher the temperature, greater is the probability of breaking Cooper pairs, thus creating quasi particles in the device. The sample box also protects the device from black-body radiation emanating from higher temperature stages in the dilution refrigerator. The fridge also comes with its own set of shielding cans which are attached to different temperature stages at the time of a cooldown which helps in minimizing the level of thermal radiation reaching the base temperature stage. Also, care is taken to cover up any line of sight ports, holes in the different stages with copper tape to prevent radiation from seeping into the sample box. In the next, section we will see how thermal management is performed on the coaxial cables used to route signals to and from the device.

We will now discuss another shielding issue especially when dealing with superconducting devices. The Meissner effect (see Chapter 2), can be used to shield devices against external magnetic fields by surrounding them with a superconducting material. We use a cylindrical can made of Al, mounted directly to the base plate or through the OFHC copper bracket, surrounding the sample box. The devices presented in this thesis all contain a SQUID, which is extremely sensitive to magnetic fields. We use an external coil mounted to the sample box to flux bias the SQUID which ideally should only be sensitive to the field generated by the coil. Without proper magnetic shielding, the SQUID becomes sensitive to spurious fields generated by everyday metal objects, magnetic components inside the dilution refrigerator, nearby lab infrastructure or even the earth's magnetic field. When the Al can goes superconducting, it expels any magnetic field lines external to it thus preventing them from reaching the device. Since the coil is inside the shield, its field lines are minimally distorted and the SQUID is now only sensitive to the coil as preferred.

A caveat to using superconductors as magnetic shields is related to their thermal conductivity. Superconductors are perfect electrical conductors but poor conductors of heat. The situation is better understood by considering the moment when the Al shield goes superconducting. The part of the shield which goes superconducting first, usually the surface contacting the OFHC copper bracket, now becomes a bad thermal conductor effectively decoupling the rest of the shield from the cryostat. We address this issue by fitting a copper mesh around the Al can with copper braids which connect to the base plate. These help cool down the Al shield evenly. Once the can is fully superconducting, any stray fields penetrating the can will be frozen. However, if the fields are non-uniform, this can result in a field gradient inside the can which the SQUID can be sensitive to. A complementary solution to this problem is to allow the superconducting can to cool down in a low-magnetic background in the first place. This is achieved by a mu-metal shield.

A mu-metal is a soft ferromagnetic alloy composed of nickel and iron, usually known

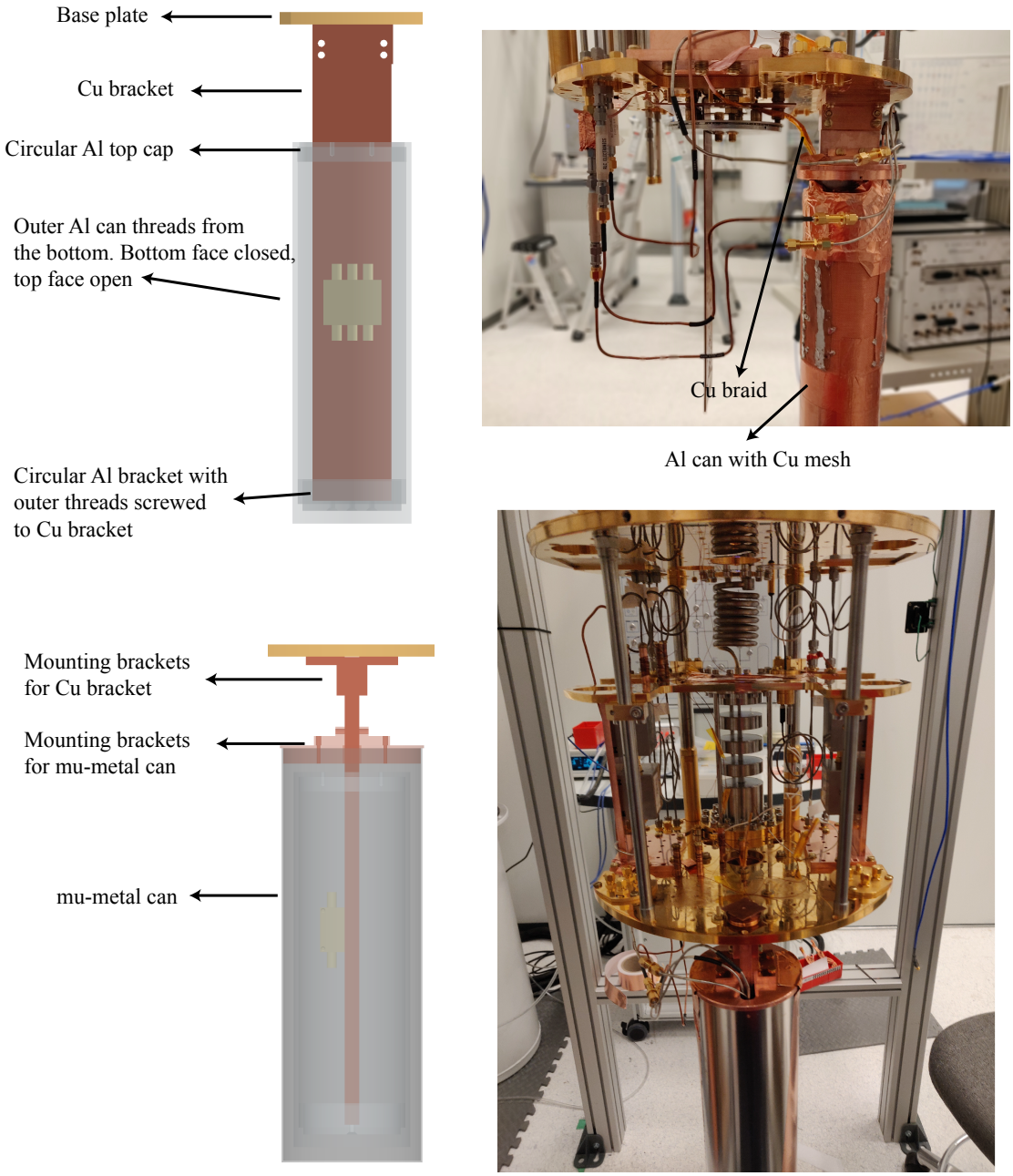

Figure 4.6: Details of magnetic shielding at the base temperature using superconducting Al and cryoperm cans

for its very high permeability often in the range of $50,000 - 100,000$, thereby providing an extremely low reluctance path for magnetic field lines. Unlike the superconducting shield which works by expelling the field lines around the sample box, mu-metal shields work by drawing the field lines into them. We use a Cryoperm shield, custom designed and fabricated by the company MuShield. Cryoperm offers the highest permeability at cryogenic temperatures. The shield is designed in the shape of a cylinder, with one of its ends opened, designed to fit around the superconducting Al shield by mounting it to the OFHC copper bracket. The Cryoperm shield drastically reduces any background field present near the Al can, allowing it to transition into the superconducting state in a low-field environment. Figure 4.6 illustrates the mounting of the superconducting and the Cryoperm shields. An additional mu-metal shield was provided by Bluefors which is snug fitted to the vacuum can of the dilution refrigerator. Adding the Cryoperm can around the Al shield improved the dephasing time of our qubits.

4.5.5 Wiring the dilution refrigerator

The situation gets even more challenging when the different stages are connected by coaxial cables which bring signals to and from the device. There are two main issues with coaxial cables. Firstly, each cable forms a direct thermal link between the stages due to the material's finite thermal conductivity. Hence, choosing the appropriate cable material for the different temperature stages is important to prevent heat leakage between the stages. Secondly, the black-body radiation of the different temperature stages of the dilution refrigerator making its way down through the cables into the device.

To promote thermal isolation between the stages, we use beryllium copper (BeCu) cables between room temperature and 50 K stage and subsequently between 50 K stage and 3 K stage for both input and output lines. BeCu has a lower thermal and electrical conductivity than copper. For the stages below 3 K, we use niobium (Nb) cables everywhere on the output line. Nb is superconducting below $\sim$ 7 K which offers the best thermal isolation while maintaining perfect electrical conductivity. For the input lines, we use stainless steel (SS) cables between the 800 mK and 100 mK stages and Nb cables for the rest. SS offers higher attenuation and better thermal isolation. Copper (Cu) cables are used for connecting components within the same stage. The SMA connectors on the SS and Nb cables are crimped while the rest are hand soldered. EZ form flexible cables with nonmagnetic SMA connectors are used to connect to the sample box.

To attenuate the black-body radiation from room temperature and the subsequent stages from reaching the device through the cables, cryo-compatible microwave attenuators

from XMA Corporation are installed at every stage for all the input cables. The choice of attenuation between the different temperature stages depends on the ratio of their respective thermal photon occupancies and the cooling power of each stage. This can be understood by considering the average thermal photon occupation $\langle n \rangle_{\text{th}}$ for each stage, which is given by the Plank distribution as,

$$\langle n \rangle_{\text{th}} = \frac{1}{\exp(\hbar\omega/k_B T) - 1}. \tag{4.2}$$

For a given frequency, when $\hbar\omega \ll k_B T$, $\langle n \rangle_{\text{th}} \sim T$. The attenuation required between each stage would then be proportional to the ratio of the stage temperatures. However, when $\hbar\omega \sim k_B T$ which for a 20 GHz photon is ~ 1 K, below this temperature the attenuation required depends exponentially on the ratio of the stage temperatures. Although, it is not possible to fully attenuate the thermal photons using attenuators alone, additional microwave filters (low-pass and band-pass filters) from RLC Electronics were used on the input and output lines to filter out the stray thermal photons outside the measurement band. The combination of attenuators and filters reduce the overall background radiation to acceptable levels so that the device operates in the quantum regime. The attenuators also aid in thermalizing the center conductor of the cable to the respective stage temperatures.

Typically, the device operating power is at the level of an average single photon which is ~ -140 to -160 dBm. The total attenuation required to achieve such low power is distributed at room temperature and across the different stages inside the refrigerator. Typically, we have 70 dB of attenuation at room temperature. The remaining attenuation is distributed accordingly between the stages as discussed earlier. Figure 4.7 shows the attenuation between different stages inside the refrigerator.

4.5.6 Measurement setup

A detailed description of the wiring scheme for the dilution refrigerator is shown in Fig. 4.7. The setup on the left is for the coupled-cavities device with the right used for the single and braided giant transmon devices. Devices are typically characterized by measuring the reflection or the transmission coefficient.

Since the output signal at the device is extremely low, typically at single-photon power levels, it is amplified to levels which can be measured at room temperature (~ -30 to -60 dBm). The first stage of amplification is done using a cryogenic high electron mobility transistor (HEMT) obtained from Low Noise Factory. The HEMT has a high gain ($\sim$ 40 dB) and a low noise temperature ($\sim 1.5 - 3$ K). Subsequent amplification is done

at room temperature. For the coupled-cavities device, the $\lambda/4$ cavity was measured in reflection. Circulators were used in this case to separate the input and the reflected fields. They also help with absorbing thermal radiation emanating from the HEMT. To measure the higher harmonic modes of the $\lambda/2$ cavity simultaneously using the same amplifier, a microwave switch from Radiall was installed at the base plate to shift between the outputs of the two cavities.

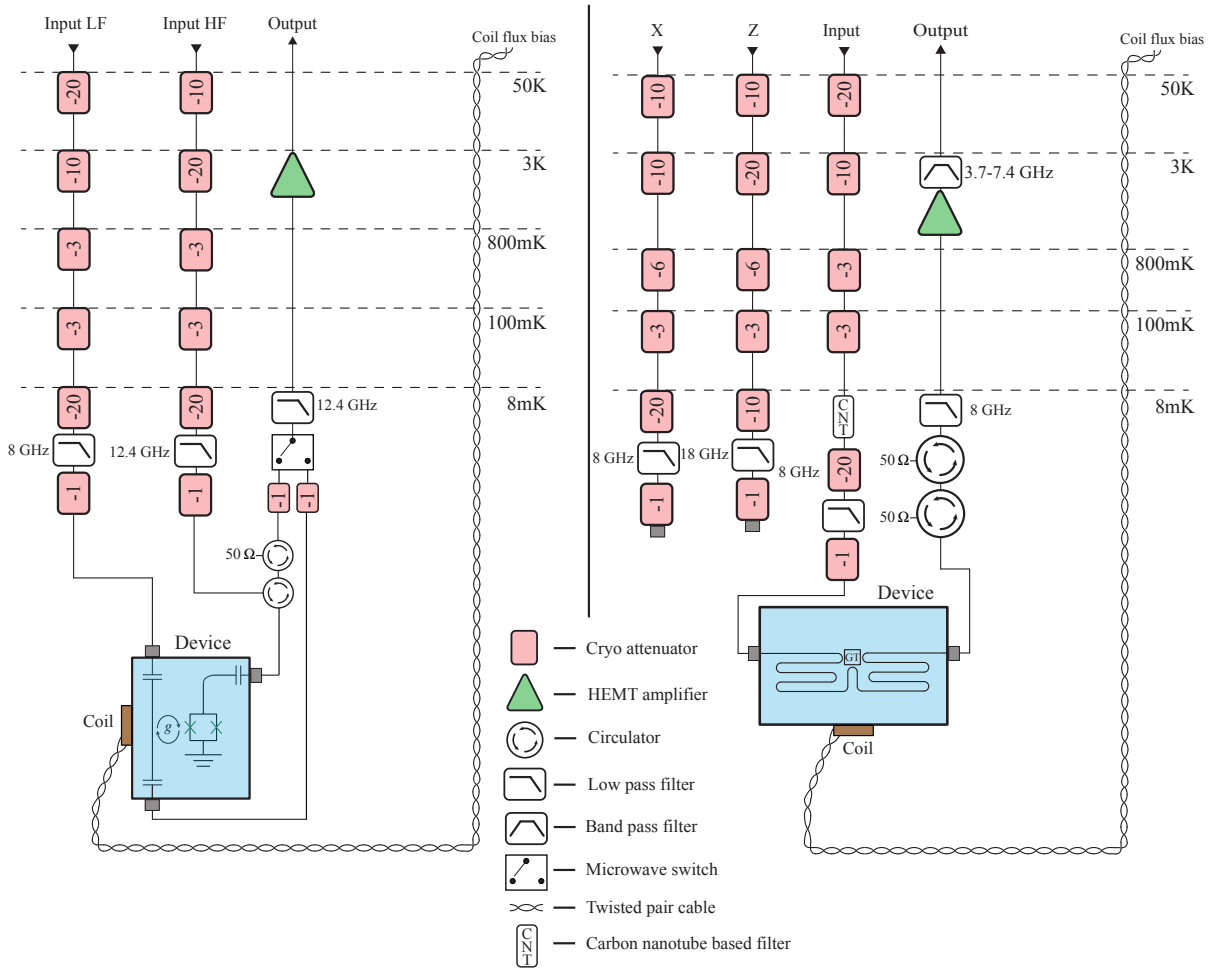

Figure 4.7: The wiring diagram inside the fridge used for the characterization of the coupled-resonator device (left) and the giant transmon devices (right).

For the giant transmon devices, the circulators are on the output side as they are characterized by measuring the transmission coefficient. To block high-frequency thermal

radiation (which are several tens of GHz to THz) on the input line, we use a carbon nanotube-based filter described in more detail in [88]. In the setup shown on the right, the X (voltage) and Z (flux) lines were used for the braided giant transmon device and are wired appropriately during the experiment.

For measuring the reflection and the transmission coefficient, we use a vector network analyzer (VNA) E5071C from Agilent at room temperature. Additional microwave sources from PhaseMatrix were used for performing two-tone spectroscopy.

Chapter 5

Level structure of a single-giant artificial atom

In this chapter, we will focus on the characterization of our single-giant transmon devices using continuous frequency-domain techniques. We present experimental data of two giant transmon devices, each with three (3CP) and six coupling points (6CP) to a 1D open TL. We will compare our experimental data to electromagnetic simulations presented earlier which brings out several different insights on how future devices can be designed.

5.1 Scattering from an artificial atom

Consider an illustration of an artificial atom coupled to a TL as shown in Fig. 5.1(a). When the atom is probed by injecting a weak probe field, V_P, into the TL as shown, the excited atom emits field in both directions, V^- and V^+, into the TL. The left-propagating emitted field of the qubit, V^-, constructively interferes with V_P, resulting in full reflection on resonance, whereas, the right-propagating emitted field destructively interferes with V_P resulting in zero transmission [13]. The reflection and the transmission coefficient can be written as,

$$r = \frac{V^-}{V_P} \quad t = \frac{V^+}{V_P}.$$

For an artificial atom coupled to 1D TL, t for the $|0\rangle - |1\rangle$ transition is given by Eq. (2.39). In the absence of dephasing, for a weak probe ($\Omega_p \ll \gamma_{10}$) of frequency ω_p on resonance with the $|0\rangle - |1\rangle$ transition of the atom, i.e, $\delta\omega_\mathrm{p} = 0$, the scattering from the

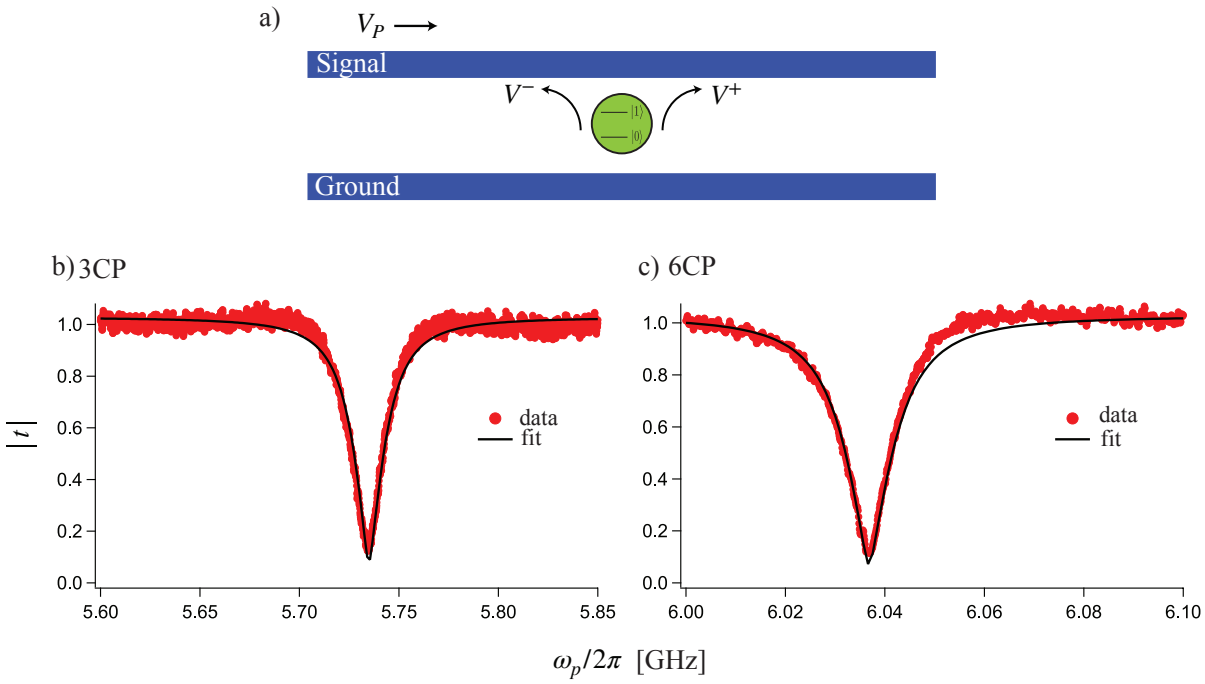

Figure 5.1: (a) Model of a an artificial atom coupled to a TL. The atom when excited by a weak resonant probe V_P will emit fields in both directions. V^- constructively interferes with V_P leading to full reflection of the probe field whereas V^+ destructively interferes with V_P leading to full extinction of the probe field. (b) Transmission spectrum showing $|t|$ as a function of probe frequency for the 3CP device and (c) for the 6CP device. We see extinction in $|t|$ (symbols) when a weak probe field is resonant with the $|0\rangle - |1\rangle$ transition frequency. The solid lines are fits using Eq. 2.39 under weak probing conditions.

atom will lead to full extinction i.e, $|t| = 0$. However, experimentally there is always a finite dephasing of the atom. The residual transmission at resonance is then, $t = \Gamma_\phi/(\Gamma_\phi + \Gamma_{10}/2)$, such that strong extinction implies $\Gamma_{10} \gg \Gamma_\phi$ and, conversely, weak extinction implies $\Gamma_{10} \ll \Gamma_\phi$. The strength of extinction hence quantifies the coupling strength of the $|0\rangle - |1\rangle$ transition.

Figure 5.1(b-c) shows the magnitude of the measured transmission co-efficient, $|t|$, for the 3CP and 6CP devices at a flux bias point when the $|0\rangle - |1\rangle$ transition is near ω_λ^S (see section 3.1.1). We use Eq. (2.39) to fit the measured transmission spectrum and extract the various rates. From the measured transmittance, $T = |t|^2$, at the qubit's resonance

frequency, we obtain a maximum extinction of 98.45% and 98.69% for the 3CP and 6CP devices respectively.

5.1.1 Background subtraction for qubit measurements

The transmission coefficient t_{meas} of a qubit coupled to a TL, measured by the VNA, is in the form of $|t_{\text{meas}}|$ (dB) and θ_{meas} (degrees) with a background level as set by the physical attenuation in our input line and the output gain of our amplifiers (see Chapter 4). This background also contains ripples due to reflections which might arise due to impedance mismatches from cables, connectors etc. In order to normalize this background level in our qubit measurements, we bias the qubit frequency away from the measurement band and obtain a background transmission coefficient trace, t_{bg}, using $|t_{\text{bg}}|$ (dB) and θ_{bg} (degrees). The normalized transmission coefficient, t, is then obtained by dividing the complex (linear) coefficients, i.e, $t = t_{\text{meas}}/t_{\text{bg}}$. In dB units, this is equivalent to,

$$\begin{aligned} |t| \text{ (dB)} &= |t_{\text{meas}}| - |t_{\text{bg}}|. \\ \theta \text{ (degrees)} &= \theta_{\text{meas}} - \theta_{\text{bg}}. \end{aligned}$$

To convert $|t|$ (dB) into linear units,

$$|t| = 10^{(|t| \text{ (dB)}/20)}.$$

We use this background subtraction method for normalized data presented in this thesis. We also note that the quality of fit generally improved after subtracting the background in our qubit experiments.

5.1.2 Considerations for fitting data

When dealing with resonance features studied using spectroscopy techniques, it is important to note that the resonance lineshape can sometimes be distorted. This asymmetric lineshape, often a result of a Fano resonance, has its origin resulting from an interference between the feature under study and its electromagnetic environment [89]. In typical setups such as ours, Fano resonances can also occur due to spurious microwave modes. In an experiment, we measure the transmission coefficient t, which can be written in complex form as $t = a + ib$, where a and b represent the real and imaginary parts. To account for the asymmetric lineshape due to Fano resonance, we add a rotation term as a fitting parameter to the data by rewriting t as,

$$t = (a + ib)e^{i\phi} = (a\cos\phi - b\sin\phi) + i(a\sin\phi + b\cos\phi).$$

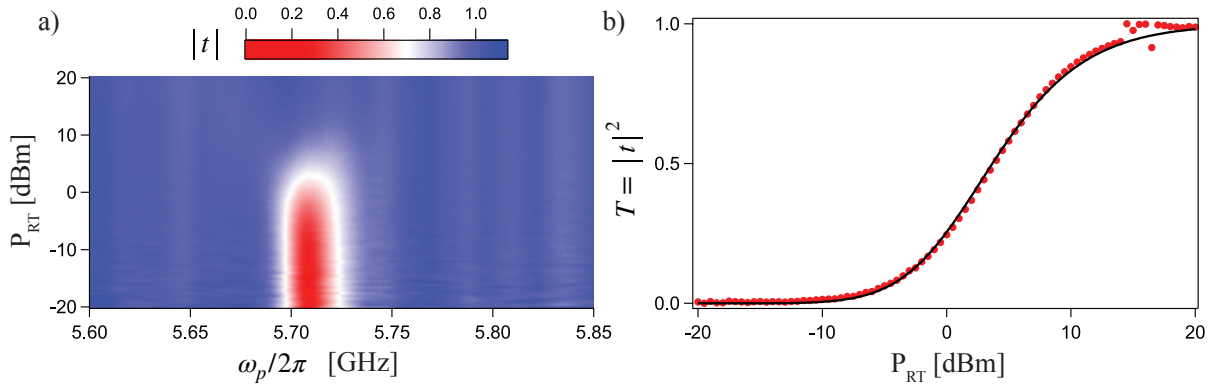

Figure 5.2: Probe-power dependent saturation of a giant transmon in our 3CP device. (a) 2D color plot showing $|t|$ for different room temperature (RT) probe powers as a function of probe frequency. As the probe power increases, due to the nonlinearity of the qubit, we see strong saturation. (b) We plot the measured transmittance (symbols) of the probe field, $T = |t|^2$, extracted on resonance with the qubit as a function of RT probe power. The solid line is a fit using Eq. 2.39 by substituting $\Omega_p = \sqrt{2}k_{10}\sqrt{P_{\mathrm{RT}}}$. The plot shows almost zero transmission at low probe powers and full transmission at high powers.

where ϕ is the rotation angle. Near resonance we can rewrite $\phi = \phi_{\mathrm{offset}} + (\omega - \omega_{10})t_{\mathrm{delay}}$, where ϕ_{offset} fixes the asymmetry and t_{delay} accounts for the slope in the transmission response which arises due to electrical delay. We use these additional two parameters in the fitting function for t given by Eq. (2.39).

5.2 Saturation of an artificial atom

An interesting physical effect is the strong saturation of the qubit as a function of probe amplitude. In the section above, we analyzed the qubit's transmission properties using a weak probe field, i.e, the Rabi frequency induced by the probe, Ω_p, is weak, thus neglecting its effect. When $\Omega_p \gg \gamma_{10}$, the nonlinearity of the qubit saturates due to the large influx of the probe photons. Since the qubit can only absorb or emit a single photon at a time, a majority of the probe photons will be transmitted without interacting with the qubit where $|t| = 1$ at higher probe amplitudes. Figure 5.2(a) shows a 2D color plot of $|t|$ for different probe powers as a function of ω_p for the 3CP device. Specifically, we control the probe power by varying the power of the VNA source, P_{RT}, at room temperature (RT). We can see strong nonlinear saturation of the atom at higher powers. From this, we can

then extract T measured on resonance with the $|0\rangle - |1\rangle$ transition for the different probe powers and is plotted it in Fig. 5.2(b).

For an artificial atom coupled to 1D vacuum, such as the case studied here, the Rabi frequency Ω_{ji} of any atomic transition, $|i\rangle - |j\rangle$, is given by [21]:

$$\Omega_{ji} = \sqrt{2} k_{ji} \sqrt{P_{ji}} \tag{5.1}$$

where, k_{ji} is the atom-field coupling constant for the $|i\rangle - |j\rangle$ transition, P_{ji} is the absolute probe power as seen by the atom which includes the attenuation in the input line. The solid line in Fig. 5.2(b) is a fit using Eq. (2.39) by substituting $\Omega_p = \Omega_{10} = \sqrt{2} k_{10} \sqrt{P_{\mathrm{RT}}}$ and using k_{10} as the fitting parameter. It is important to note here that the value of k_{ji} we extract using this method, here and in our later measurements, combines the fundamental coupling constant along with experimental effects such as loss in the TL. We instead use Ω_{ji} as an absolute self-calibrated measure of our probe power as seen by the atom.

5.3 $|0\rangle - |1\rangle$ transition spectroscopy

In this section, we will first characterize the frequency tunability of the $|0\rangle - |1\rangle$ transition of our giant transmon devices. Following this, we will extract the coupling rate of the $|0\rangle - |1\rangle$ transition as a function of the transmon resonance frequency.

5.3.1 Frequency-dependent coupling of $|0\rangle - |1\rangle$ transition

As discussed in Chapter 2, one of the major advantages of using artificial atoms over natural atoms is that, their transition frequencies can be tuned over a wide range in the measurement bandwidth. The $|0\rangle - |1\rangle$ transition frequency of the transmon qubit, f_{10}, is given by [34]:

$$f_{10} \approx \frac{\sqrt{8 E_J(\Phi) E_c} - E_c}{h}, \tag{5.2}$$

where $E_J(\Phi)$ is the flux dependent Josephson energy of the SQUID and $E_c = q^2/2C_\Sigma$ is the charging energy of the transmon with C_Σ representing the total capacitance of the transmon structure. We use a small coil which is attached to the sample box in order to generate an external flux, Φ. The coil is excited using a voltage source with a bias resistor at room temperature with integrated low pass filters.

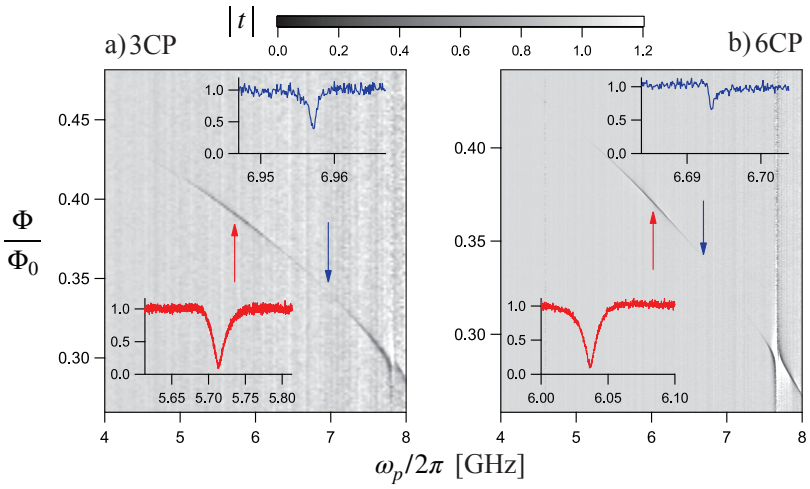

Figure 5.3: Transmission spectroscopy of the giant transmon for the (a) 3CP and (b) 6CP devices for a weak probe at ω_p. We tune the transition frequency of the giant transmon by changing the external magnetic flux, Φ. The color scale indicates the magnitude of the transmission coefficient, t. When the transmon is biased close to ω_λ^S (indicated by red arrows), we see strong extinction of the probe, suggesting that the qubit is strongly coupled to the TL. We also observe frequency regions where the probe's extinction is weak (indicated by blue arrows), implying that the coupling of the transmon to the TL is suppressed. The insets in (a) and (b) are linecuts taken at the flux bias points indicated by the corresponding colored arrows. The background has been subtracted for clarity in both figures.

By using transmission spectroscopy data as discussed above, we probe our giant transmon for different flux bias conditions under weak probing conditions. Figure 5.3 shows a 2D color plot of $|t|$ as a function of probe frequency for various flux biases for both 3CP and 6CP devices. We calibrate the flux quantum, Φ_0, by measuring many periods of this flux bias curve (not shown here). As we tune the frequency of the giant transmon, we observe that the on-resonant extinction of the qubit is strongly modulated. We show this at two flux bias points, where we observe maximum and minimum coupling of the $|0\rangle - |1\rangle$ transition of the giant transmon to the TL as indicated by the red and blue arrows respectively. The maximum coupling happens near ω_λ^S as predicted by theory [27] (see section 3.1.1) whereas the minimum coupling frequency disagrees with the theoretical prediction.

A key feature of the giant artificial atom is the predicted frequency dependence of its coupling to its electromagnetic environment. Here, we will use high resolution transmission

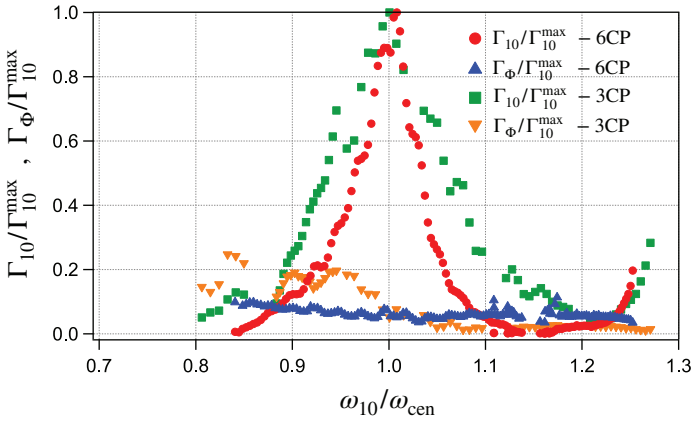

Figure 5.4: By fitting transmission spectroscopy data similar to Fig. 5.3 using Eq. (2.39), we can extract the relevant rates for different qubit frequencies. The rates are normalized to the maximum Γ_{10}^{max} (see Table 5.1). The transmon frequency ω_{10} is normalized to the center frequency ω_{cen} of the rate profiles (extracted from a Lorentzian fit to the profiles). The 6CP device has a sharper relaxation-rate profile, consistent with the theoretical prediction of stronger interference resulting from the larger number of coupling points. The profiles that we extract for the two devices are narrower than the theoretical prediction [27] by a factor of approximately 2. However, we see that the FWHM of the 6CP device is approximately half that of the 3CP device, which agrees with the predicted scaling.

spectroscopy data, similar to Fig. 5.3, and extract the various rates, Γ_{10}, Γ_ϕ and γ_{10} for both 3CP and 6CP devices as a function of the $|0\rangle - |1\rangle$ transition frequency. We use Eq. (2.39) to fit the transmission spectrum for every frequency bias point of the $|0\rangle - |1\rangle$ transition. We do this under weak probing conditions as mentioned above. Figure 5.4 shows the extracted rates, Γ_{10} and Γ_ϕ, as a function of ω_{10}. The rates are normalized to the maximum relaxation rate, Γ_{10}^{max}, and ω_{10} is normalized to the center frequency, ω_{cen} of the rate profile for the respective device. We obtain ω_{cen} from a Lorentzian fit to the rate profiles (not shown here).

The 6CP device shows a stronger modulation of the coupling rate when compared to the 3CP device as expected due to the higher number of coupling points which results in stronger interference effects as discussed in Chapter 2. A typical figure of merit which characterizes the maximum and the minimum coupling of the $|0\rangle - |1\rangle$ transition is the on-off ratio, $\alpha = \Gamma_{10}^{max}/\Gamma_{10}^{min}$, where Γ_{10}^{min} is measured at ω_{min}. We measure $\alpha > 300$ for the 6CP device. To our knowledge, this is a record high on-off ratio measured for a superconducting waveguide QED device at the time of writing this thesis. Table 5.1 summarizes the various

Device	$E_J^{\max}/h$	E_c/h	$\omega_{\max}/2\pi$	$\omega_{\min}/2\pi$	$\Gamma_{10}^{\max}/2\pi$	$\Gamma_{10}^{\min}/2\pi$	α	$\beta_{\max}$	$\beta_{\min}$
3CP	32.13	0.460	5.734	6.936	25×10^{-3}	1.1×10^{-3}	23	13	0.26
6CP	32.13	0.429	6.036	6.827	17×10^{-3}	44×10^{-6}	380	62	0.29

Table 5.1: Parameters for the 3CP and 6CP devices. All values are expressed in GHz except for α, $\beta_{\max}$, and $\beta_{\min}$, which are dimensionless. The quantity α is the ratio of the maximum to the minimum coupling strength of the $|0\rangle - |1\rangle$ transition. The quantity β is the ratio of the $|1\rangle - |2\rangle$ to the $|0\rangle - |1\rangle$ coupling strength. The ratios $\beta_{\max}$ and $\beta_{\min}$ are measured at two different flux biases, one which maximizes and one which minimizes β.

parameters extracted using this method for both devices.

A key point to note here is that although the maximum coupling of the $|0\rangle - |1\rangle$ transition occurs at $\sim \omega_\lambda^{\mathrm{S}}$, we observe that our minimal-coupling points occur at frequencies different from those predicted by theory [27]. Generally, we find that the experimental curves are narrower when compared to the theoretical predictions. However, we observe that the full width at half maximum (FWHM) of the 6CP device, $\mathrm{FWHM}_{\mathrm{6CP}} = 377$ MHz is narrower than that of the 3CP device, $\mathrm{FWHM}_{\mathrm{3CP}} = 687$ MHz, by approximately a factor of 2, which is consistent with the scaling predicted by theory [27]. The theoretical FWHM of the 3CP and 6CP devices are 1.78 GHz and 853 MHz, respectively.

To study the cause of this discrepancy in the absolute FWHM, we simulate the microwave transmission of the full-chip layout of the 3CP and 6CP devices using HFSS by Ansys. The results of the simulations are discussed in Chapter 3. The results of the simulation show a qualitatively similar deviation from theory, but the narrowing is not as large as in our experimental results. If we add more wirebonds to the simulation (beyond what is possible to replicate in experiment), we do, however, find a good agreement with theory. Based on these simulation results, and others discussed in Chapter 3, we attribute the experimental deviation to parasitic microwave effects such as slot-line modes, radiation effects, etc. We expect that future device designs, for instance, incorporating air bridges between the ground planes, would eliminate these effects.

5.4 $|1\rangle - |2\rangle$ transition spectroscopy

So far, we looked at single-tone spectroscopy characterization of the $|0\rangle - |1\rangle$ transition and convincingly demonstrated its frequency-dependent coupling. The transmon also has higher transitions due to the weakly-anharmonic behavior of its ladder structure. We

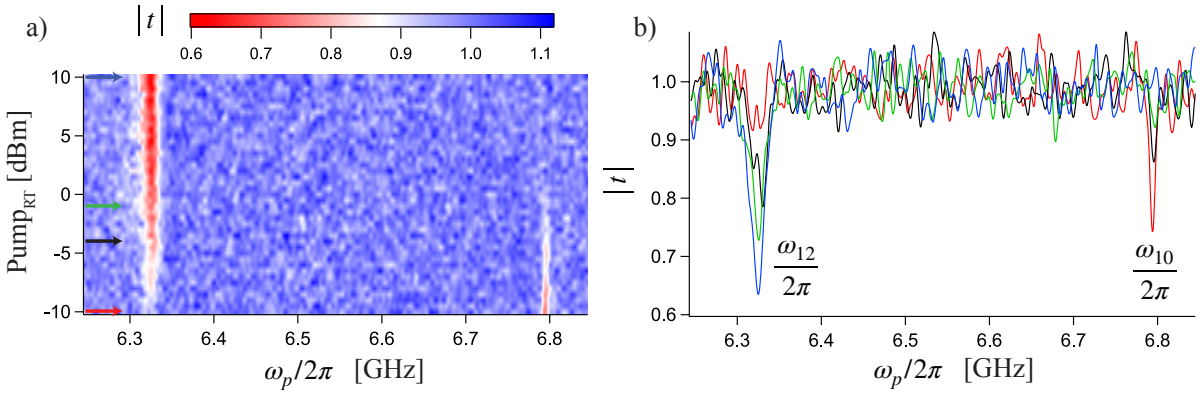

Figure 5.5: Two-tone spectroscopy measurements for the 3CP device to measure the anharmonicity of the giant transmon. (a) To find the $|1\rangle - |2\rangle$ spectroscopy line, we resonantly pump the $|0\rangle - |1\rangle$ transition and weakly probe around the expected frequency for the $|1\rangle - |2\rangle$ transition. The 2D plot shown here shows $|t|$ for different pump powers of a room temperature microwave source. At low pump powers, we see strong scattering from the $|0\rangle - |1\rangle$ transition as expected. As the pump power increases, the $|0\rangle - |1\rangle$ transition saturates and we now see scattering from the $|1\rangle - |2\rangle$ transition, which becomes stronger with pump power. (b) Linecuts from (a) for different pump powers which are color coded corresponding to the position of the colored arrows in (a).

expect these higher levels to also have a frequency-dependent coupling. In this section we will explore on how to extract the coupling strength for the $|1\rangle - |2\rangle$ transition. The frequency-dependent coupling of the $|1\rangle - |2\rangle$ transition also gives us the ability to tune its behavior relative to that of the $|0\rangle - |1\rangle$ transition. This novel feature of the giant transmon will be explored later to demonstrate an effective lambda system, something which is not possible with an ordinary transmon.

5.4.1 Two-tone spectroscopy

In order to observe the $|1\rangle - |2\rangle$ transition, we use a two-tone spectroscopy technique where we strongly pump the $|0\rangle - |1\rangle$ transition on resonance and weakly probe around the $|1\rangle - |2\rangle$ transition which is at $\omega_{21} \approx \omega_{10} - E_c/\hbar$ [34]. The pump tone transfers population to the $|1\rangle$ level and by probing the $|1\rangle - |2\rangle$ transition we see coherent scattering from this transition, which appears as a dip in $|t|$ near ω_{21}. As the pump power increases, the dip in $|t|$ increases up to a point when the $|0\rangle - |1\rangle$ transition is fully saturated by the pump. Figure 5.5(a)

shows a 2D color plot of $|t|$ for various pump powers as a function of the probe frequency for our 3CP device. Although, this technique helps us identify ω_{21}, extracting Γ_{21} is not straightforward. Alternatively, the relaxation rate of higher transitions of the transmon can be measured using time-domain techniques [90].

5.4.2 Mollow triplet and Autler-Townes Splitting

We saw earlier in Section. 5.2 that we can use single-tone spectroscopy of the probe-power dependent saturation of the $|0\rangle - |1\rangle$ transition in order to calibrate Ω_{10} for the giant transmon. In this section, we will look at two more physical effects which can be observed using two-tone spectroscopy techniques which will help us to calibrate Ω_{10} and Ω_{21}. The Mollow triplet [91] and the Autler-Townes Splitting (ATS) [92] are two popular effects in quantum optics which were also demonstrated in superconducting circuits [93, 94]. We observe these effects in both 3CP and 6CP devices. Here, we present the results using the 6CP giant transmon device.

Mollow triplet

As an alternative method to calibrate Ω_{10}, we use the Mollow Triplet. To observe this effect, we use a pump-probe spectroscopy technique where we strongly pump the $|0\rangle - |1\rangle$ transition on resonance and weakly probe around ω_{10}. As the pump power increases, this begins to dress the $|0\rangle - |1\rangle$ transition resulting in the splitting of the $|0\rangle$ and $|1\rangle$ levels by an amount equal to Ω_{10} as shown in Fig. 5.6(a). When probing around ω_{10}, we then observe three different spectroscopic lines as shown in Fig. 5.6(b), corresponding to the four transitions out of which two are degenerate (see Fig. 5.6(a)). The data shown in the figure comes from the 6CP device at a certain flux bias point.

Autler-Townes Splitting

The Autler-Townes Splitting is another spectroscopic signature which depends on the dressing of the $|1\rangle - |2\rangle$ transition. We will use it to calibrate Ω_{21}. In order to observe this feature, we strongly pump the $|1\rangle - |2\rangle$ transition on resonance and weakly probe around the $|0\rangle - |1\rangle$ transition as depicted in the driving scheme in Fig. 5.6(c). The pump tone dresses the $|1\rangle$ and $|2\rangle$ levels causing them to spilt by Ω_{21}. When probing around ω_{10} as a function of power, we see this splitting as a doublet in the spectroscopic signature, as shown in Fig. 5.6(d).

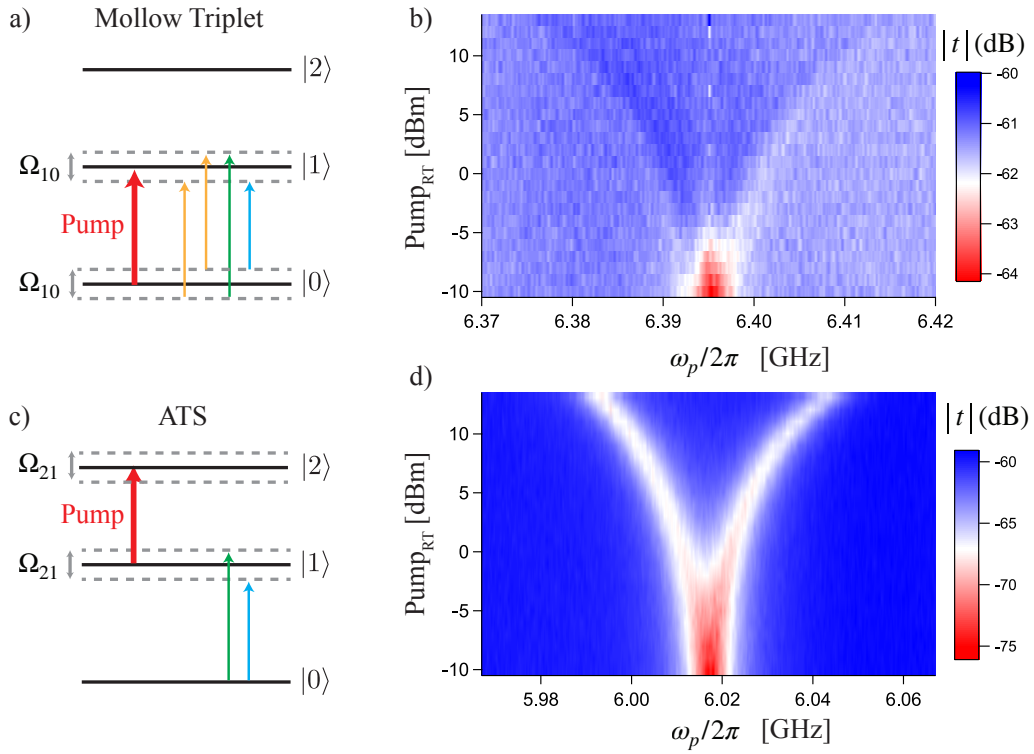

Figure 5.6: Observation of the Mollow triplet and Autler-Townes Splitting (ATS) in the 6CP device. (a) Driving scheme for observing the Mollow triplet. The $|0\rangle - |1\rangle$ transition is resonantly driven by a strong pump tone which dresses the $|0\rangle$ and $|1\rangle$ levels. The levels split where the frequency of the separation is given by the Rabi frequency Ω_{10}. On probing the $|0\rangle - |1\rangle$ transition weakly, we observe three spectroscopic lines, corresponding to the four lines shown, two of which are degenerate. (b) Experimental signatures of the Mollow triplet. The 2D plot shows t as a function of the probe frequency for different pump powers, clearly showing the Mollow triplet. (c) Driving scheme for observing ATS. A strong pump tone which is on resonant with the $|1\rangle - |2\rangle$ transition, dresses the $|1\rangle$ and $|2\rangle$ levels, where the splitting is given by Ω_{21}. Upon weakly probing the $|0\rangle - |1\rangle$ transition, we observe a doublet in the spectroscopy signature. (d) Experimental signature of ATS showing t as a function of probe frequency for different pump powers.

5.4.3 Frequency-dependent coupling of $|1\rangle - |2\rangle$ transition

The two-tone spectroscopy technique discussed above helps us identify ω_{21} but does not give us Γ_{21} directly. In order to characterize the frequency-dependent coupling, $\Gamma_{21}(\omega)$, we will make use of the probe-power dependent saturation of the $|0\rangle - |1\rangle$ transition and the ATS, both of which are discussed earlier.

General procedure to extract $\Gamma_{21}(\omega)$

To extract $\Gamma_{21}(\omega)$ for our giant transmon, we start by observing that the relaxation rate of the $|i\rangle - |j\rangle$ transition, $\Gamma_{ji}(\omega)$, depends on two quantities: the spectral density of environmental fluctuations, $S(\omega)$, and the atom-field coupling constant, $k_{ji}(\omega)$ [95]. The specific relation is:

$$\Gamma_{ji}(\omega) = k_{ji}^2(\omega) S(\omega). \tag{5.3}$$

Here we make the implicit choice to absorb the effects of interference into k_{ji}. Since we can directly measure $\Gamma_{10}(\omega)$ (see Section. 5.3), we see that we can infer $\Gamma_{21}(\omega)$ by only further measuring the ratio $k_{21}(\omega)/k_{10}(\omega)$. This gives us:

$$\Gamma_{21}(\omega) = [k_{21}^2(\omega)/k_{10}^2(\omega)]\Gamma_{10}(\omega) \tag{5.4}$$

In section 5.2, we saw that the Rabi frequency Ω_{ji} for a given transition $|i\rangle - |j\rangle$ relates to the same atom-field coupling constant k_{ji} as shown in Eq. 5.2. Measuring Ω_{ji} for the two transitions at the same frequency and drive power allows us to immediately calculate $k_{21}(\omega)/k_{10}(\omega) = \Omega_{21}(\omega)/\Omega_{10}(\omega)$. Note that to measure Ω_{21} and Ω_{10} at the same frequency implies measuring them at two different flux bias points, since $\omega_{21} \approx \omega_{10} - E_c/\hbar$.

Experimental details

Figure 5.7 shows the ATS and probe-power dependent saturation measurements for the 3CP device. To measure Ω_{21}, we use ATS by manually extracting the splitting in the spectroscopic doublet signature. To measure Ω_{10}, we use the probe-power saturation of the $|0\rangle - |1\rangle$ transition of the transmon. The effect is fully described by the presence of the probe Rabi frequency $\Omega_p = \Omega_{10}$ in Eq. 2.39. As described in Fig. 5.7, we measure both Ω_{21} and Ω_{10} at many values of the pump and probe power respectively, and use the ratios of the slopes to give a more accurate value of $k_{21}(\omega)/k_{10}(\omega)$. We convert the room temperature pump and probe power [dBm] of the microwave source into an effective amplitude [V] by assuming a 50 Ω load at its output. In both measurements, we see that the extracted Ω_{ji}

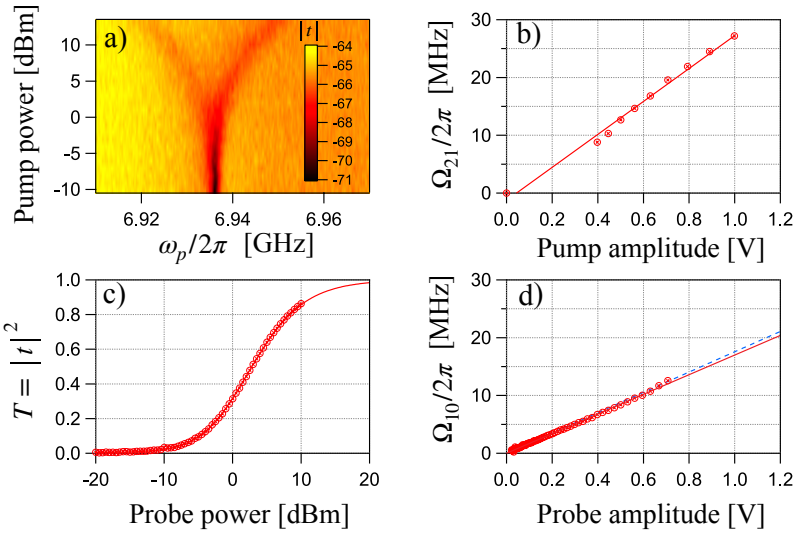

Figure 5.7: Extracting $\Gamma_{21}(\omega)$ by measuring the atom-field coupling constants. (a) To calibrate the coupling constant k_{21}, we use the Autler-Townes splitting (ATS) by pumping the $|1\rangle - |2\rangle$ transition on resonance and probing the $|0\rangle - |1\rangle$ transition. The pump tone dresses the $|1\rangle - |2\rangle$ transition and we observe the familiar spectroscopic doublet with a splitting given by Ω_{21}. The color scale indicates $|t|$ in dB. (b) We manually extract Ω_{21} at each power and plot the extracted values (symbols) as a function of pump amplitude. Recalling that $\Omega_{ji} = \sqrt{2}k_{ji}\sqrt{P}$ (see text), we extract $k_{21}(\omega)$ from a straight line fit (solid line). (c) To calibrate k_{10}, we use the strong saturation of the transmon's $|0\rangle - |1\rangle$ transition as a function of probe power. This is described by the presence of the probe Rabi frequency $\Omega_p = \Omega_{10}$ in Eq. (2.39). After changing the flux bias such that the $|0\rangle - |1\rangle$ transition is at the same frequency as the $|1\rangle - |2\rangle$ transition above, we measure t as a function of the probe power. To characterize the saturation, we plot the transmittance $T = |t|^2$ on resonance, i.e., $\omega_p = \omega_{10}$ (symbols). We fit T using Eq. (2.39) (solid line), substituting $\Omega_p = \sqrt{2}k_{10}\sqrt{P}$ and then extract k_{10} as a fitting parameter (solid line). (d) As a second method to extract k_{10}, we fit the full transmission curve at each power and extract an independent value of Ω_{10}. The extracted values are plotted versus probe amplitude (symbols). We then extract k_{10} from a straight-line fit to this data (red, solid line). For reference, we also plot the line (blue, dash line) corresponding to the value of k_{10} extracted in panel (c). There is an obvious agreement between the two values of k_{10}. (For subsequent calculations, we use the value of k_{10} extracted from panel (d).) By using k_{21}, k_{10}, and Γ_{10} (measured independently from low-power spectroscopy), we can infer $\Gamma_{21}(\omega)$ as described in the main text.

for both transitions is directly proportional to the pump/probe amplitude as validated by a straight line fit to the data where the constant of proportionality quantifies k_{ji} as given by Eq. 5.2. Since the measurements are done at the same bias frequency for both the $|0\rangle - |1\rangle$ and $|1\rangle - |2\rangle$ transitions and knowing Γ_{10} at this bias frequency, we can calculate $\Gamma_{21}(\omega)$ by substituting the extracted ratio $k_{21}(\omega)/k_{10}(\omega)$ and $\Gamma_{10}(\omega)$ in Eq. 5.4 directly giving us our answer.

Quantifying modulation of Γ_{21} relative to Γ_{10}

In order to quantify the relative modulation of Γ_{21} and Γ_{10}, we define a relaxation-rate ratio,

$$\beta = \frac{\Gamma_{21}(\omega_{21})}{\Gamma_{10}(\omega_{10})}. \tag{5.5}$$

Our results clearly demonstrate that we can modulate β by either enhancing or suppressing Γ_{21} relative to Γ_{10} depending on the chosen operating flux bias point. Table 5.1 shows both the maximum and minimum values of β, which strongly deviate from 2. We also see that increasing the number of connection points can result in stronger modulation of β. For the 6CP device in particular, we achieve a maximum β of 62 and a minimum of 0.29, a modulation by more than a factor of 200. An alternative approach to modulating β in an ordinary transmon is by making use of impedance-mismatching elements to alter the density of states seen by the qubit, resulting in a frequency-dependent Purcell decay [96]. The frequency-dependent relaxation rates of the giant transmon, complemented by the freedom in engineering the rates relative to each other, adds a new flavor to the existing waveguide-QED toolbox.

5.5 Giant transmon as a Lambda system

A Lambda system, more popularly known as Λ system, belongs to a class of optical three-level systems where one of the level is metastable. Due to this metastability, coherence can be built under external driving conditions, enabling a variety of quantum interference. These effects include electromagnetically induced transparency (EIT), coherent population trapping (CPT), dark state, lasing without inversion, optical memories and slow light [9].

The success of the transmon qubit in the quantum computing industry has largely been attributed to its robust design complemented by its frequency-tunability, freedom to engineer anharmonicity between its levels, low susceptibility to charge and flux noise,

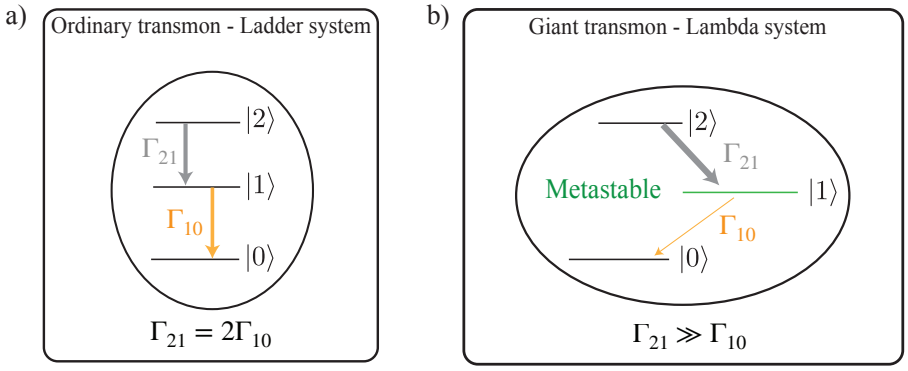

Figure 5.8: Ladder vs. Lambda system. (a) An ordinary transmon qubit has a ladder configuration of its multiple levels which ensure that the relaxation rate of its many transitions are on the same order of magnitude indicating the absence of a metastable state. (b) By appropriately flux biasing the giant transmon, it can be used as an effective lambda systems where $\Gamma_{21} \gg \Gamma_{10}$ thus making the $|1\rangle$ level metastable. In this configuration, we use the giant transmon qubit to demonstrate EIT.

and long coherence times. However, the transmon has a ladder configuration of its many levels [72], irrespective of the operating bias frequency. For the $|0\rangle - |1\rangle$ and the $|1\rangle - |2\rangle$ transitions, $\beta = 2$ (see Fig. 5.8(a)). Due to this, there is an absence of a metastable state in the inherent transmon design which limits its versatility.

With our giant transmon device, due to its tunable relaxation rates and large modulation of β, we can engineer a metastable state thereby turning it into an effective lambda system where $\Gamma_{21} \gg \Gamma_{10}$ (see Fig. 5.8(b)). We do this simply by biasing the transmon at the flux that maximizes β (see Table. 5.1). As a benchmark demonstration of Λ system physics, we demonstrate EIT in our giant transmon.

5.5.1 Electromagnetically Induced Transparency (EIT)

EIT is a process in which absorption at a given atomic transition is suppressed due to destructive interference between two different excitation pathways enabled by the presence of a metastable state in a three-level system [97]. Our claim to demonstrate EIT, as opposed to ATS, is supported by a detailed master-equation calculation as well as an analysis based on Akaike's information criterion, as suggested in Ref. [98].

EIT-Theory

The theory presented in this section, has been worked out by our collaborators Andreas Ask and Anton Frisk Kockum.

We consider a three-level system with energy levels $|0\rangle, |1\rangle$ and $|2\rangle$, where $\Gamma_{21} \gg \Gamma_{10}$ such that a Λ system is formed with level $|1\rangle$ being metastable. The system is driven by a control field at the $|0\rangle - |2\rangle$ transition with amplitude Ω_c and frequency ω_c, and a weak probe field is applied to the $|1\rangle - |2\rangle$ transition with amplitude Ω_p and frequency ω_p. Note that we model the $|0\rangle - |2\rangle$ transition as a single-photon process in our theory calculations, although the transition is induced via a two-photon process experimentally. The system is described by the following Hamiltonian:

$$\begin{aligned} H = &\omega_2\sigma_{22} + \omega_1\sigma_{11} + i\frac{\Omega_c}{2}\left(e^{-i\omega_c t} + e^{i\omega_c t}\right)(\sigma_{02} - \sigma_{20}) \\ &+ i\frac{\Omega_p}{2}\left(e^{-i\omega_p t} + e^{i\omega_p t}\right)(\sigma_{12} - \sigma_{21}), \end{aligned} \tag{5.6}$$

where we have set the $|0\rangle$ state to have zero energy, and we have defined $\sigma_{ij} \equiv |i\rangle\langle j|$. The time dependence can be removed by going into a rotating frame by applying the unitary transformation,

$$U(t) = e^{it(\omega_c\sigma_{22} + (\omega_c - \omega_p)\sigma_{11})}. \tag{5.7}$$

The rotated Hamiltonian is then given by

$$\tilde{H} = UHU^\dagger + i\frac{dU}{dt}U^\dagger. \tag{5.8}$$

We perform a rotating-wave approximation (RWA) and neglect terms that oscillate at the frequencies $2\omega_c$ and $2(\omega_c - \omega_p)$, which gives us the time-independent Hamiltonian

$$\begin{aligned} \tilde{H} = &\Delta_1\sigma_{22} + (\Delta_1 - \Delta_2)\sigma_{11} + i\frac{\Omega_c}{2}(\sigma_{02} - \sigma_{20}) \\ &+ i\frac{\Omega_p}{2}(\sigma_{12} - \sigma_{12}), \end{aligned} \tag{5.9}$$

where we introduced the two detunings $\Delta_1 = \omega_2 - \omega_p$, and $\Delta_2 = (\omega_2 - \omega_1) - \omega_c$. Note that we drop the tilde on the rotated Hamiltonian in Eq. (5.11).

We calculate the system dynamics by solving the master equation,

$$\begin{aligned} \dot{\rho} = &-i[H, \rho] + \Gamma_{20}\mathcal{D}[\sigma_{02}]\rho + \Gamma_{21}\mathcal{D}[\sigma_{12}]\rho + \Gamma_{10}\mathcal{D}[\sigma_{01}]\rho \\ &+ 2\Gamma_{2\phi}\mathcal{D}[\sigma_{22}]\rho + 2\Gamma_{1\phi}\mathcal{D}[\sigma_{11}]\rho, \end{aligned} \tag{5.10}$$

where Γ_{ji} is the decay rate from state $|j\rangle$ to $|i\rangle$, $\Gamma_{i\phi}$ is the pure dephasing rate of state $|i\rangle$, $\sigma_{ij} = |i\rangle\langle j|$, and we used the notation $\mathcal{D}[X]\rho = X\rho X^\dagger - \frac{1}{2}X^\dagger X\rho - \frac{1}{2}\rho X^\dagger X$ for the Lindblad superoperator [99]. Translating the generalized Hamiltonian given by Eq. (5.9) for the giant transmon, we get,

$$H = \Delta_c\sigma_{22} + (\Delta_c - \Delta_p)\sigma_{11} + i\frac{\Omega_c}{2}\left(\sigma_{02} - \sigma_{20}\right) + i\frac{\Omega_p}{2}\left(\sigma_{12} - \sigma_{12}\right), \tag{5.11}$$

where $\Delta_c = \omega_{20} - \omega_c$ is the detuning of the pump field, $\Delta_p = \omega_{21} - \omega_p$ is the detuning of the probe field, and $\Omega_{c/p}$ is the drive strength of the pump and probe field respectively. To obtain a transmission coefficient, we consider an incoming probe field containing an average number of photons per unit time of $|\alpha|^2$, and use the input-output relation $t = 1 + \sqrt{\Gamma_{21}/2}\,\langle\sigma_{12}\rangle\,/\alpha$. To fit the experimental data, t was multiplied by an additional real scale factor to account for amplification and attenuation along the signal line.

There has been discussion in recent literature about how best to distinguish EIT from other phenomena, in particular, the Autler-Townes splitting (ATS) mentioned above [98]. The question of whether the pump and probe conditions put the system in the ATS or EIT regime can be addressed in a number of ways. From a purely theoretical point of view, the two can be distinguished by examining the poles of the transmission coefficient [100]: t has one pole in the EIT regime and two poles in the ATS regime. The transition between the two regimes can then be parametrized by a threshold pump power, Ω_t, where the number of poles change. By expanding the transmission coefficient to first order in the small parameter Ω_p/Γ_{21}, we can derive $\Omega_t = \gamma_{21} - \gamma_{10} = \Gamma_{21}/2 + \Gamma_{20}/2 + \Gamma_{2\phi}$. For $\Omega_c < \Omega_t$ the system is in the EIT regime, and for $\Omega_c > \Omega_t$ the system is in the ATS regime.

EIT-Experiment

We can transition between the EIT and ATS regime by tuning the pump power. We, therefore, present two sets of transmission measurements for both the 3CP and 6CP device, one with low and one with high pump power. The strength of the pump at the device was extracted from the fits to the master equation calculation, as were the decoherence rates that were not measured independently. We present calculated and measured EIT curves as a function of Δ_c and Δ_p for both 3CP and 6CP devices in Figure 5.9 and Fig. 5.10 respectively. The theory and experiment are both in good agreement and the extracted parameters are presented in Table 5.2.

From the decoherence rates in Table 5.2, we can calculate the threshold drive-strength Ω_t and compare it to the extracted drive strength Ω_c used in the experiment. This suggests

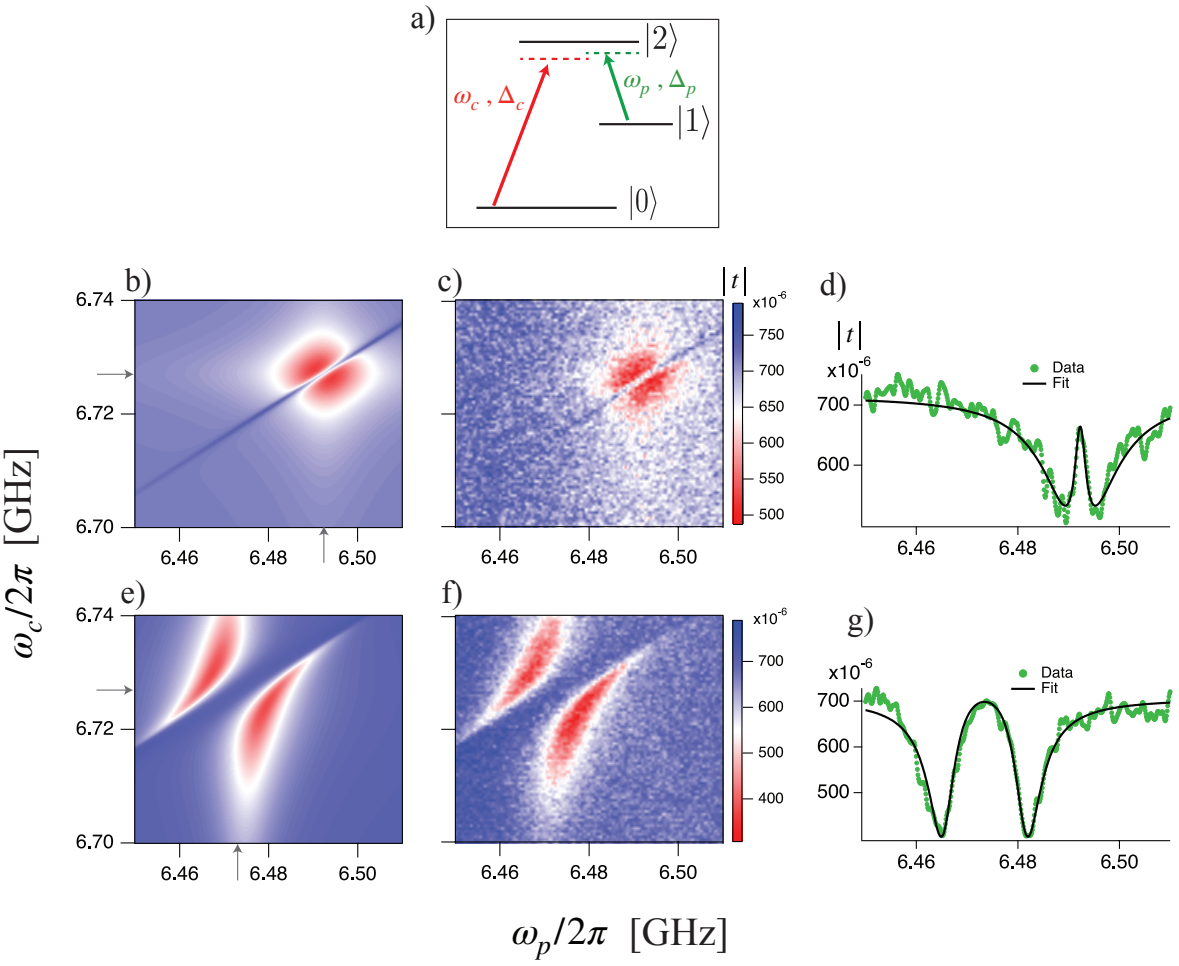

Figure 5.9: EIT vs. ATS in the 3CP device. We study the response of the device in a pump-probe experiment designed to reveal EIT. (a) Shows the three levels of the giant transmon together with the strong pump (control) tone at ω_c and a weak probe tone at ω_p, with detunings Δ_c and Δ_p respectively. (b) and (e) show the numerical calculations for low and high control power, respectively, for the 3CP device. The corresponding experimental data are shown in (c) and (f). The zero-detuning points are indicated by grey arrows on the theory plot axes. The color scale is the magnitude of the transmission coefficient in linear units. The line cuts shown in (d) and (g) are taken at $\Delta_c = 0$ for the two pump power conditions. Where possible, we use independently measured parameters, but the fits also allow us to extract additional parameters (see Table 5.1). For the low control power, we are in the EIT regime, while for the high pump power, we are in the ATS regime.

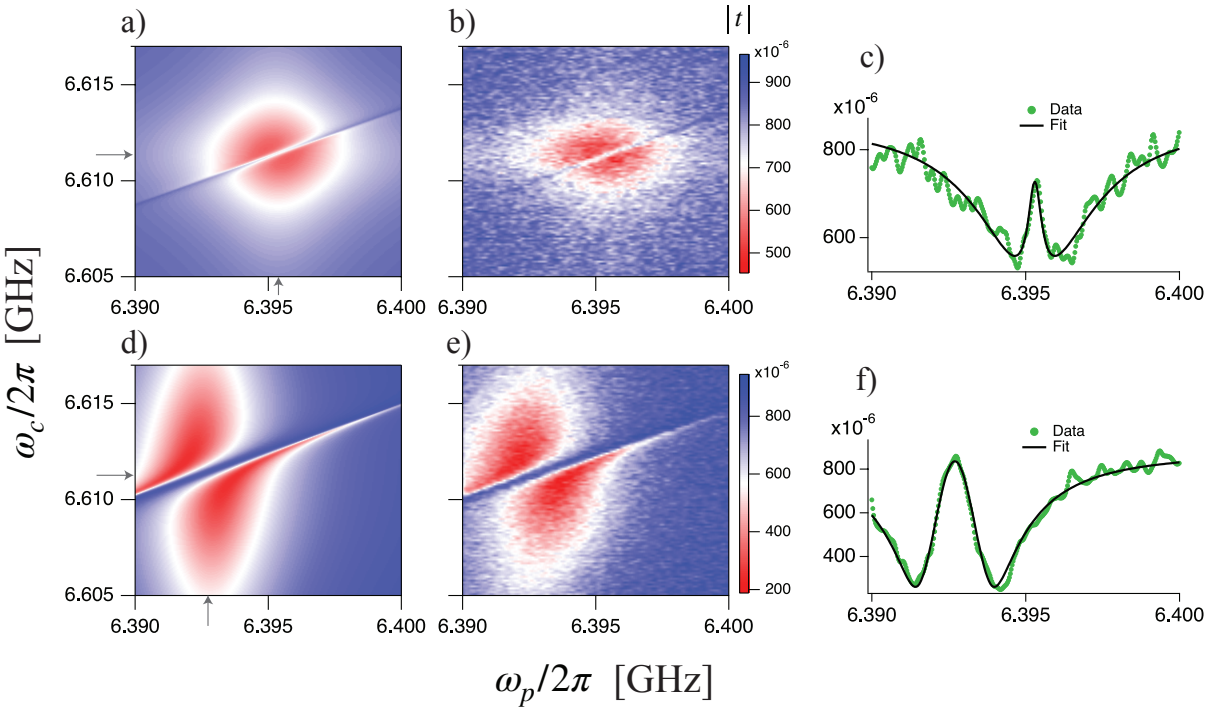

Figure 5.10: EIT in the 6CP device. (a) and (d) show the numerical calculations for low and high control power, respectively. The corresponding experimental data are shown in (b) and (e). The zero-detuning points are indicated by grey arrows on the theory plot axes. The color scale is the magnitude of the transmission coefficient in linear units. The line cuts shown in (c) and (f) are taken at $\Delta_c = 0$ for the two pump power conditions. For the low control power, we are in the EIT regime while for the high pump power, we are in the border between EIT and ATS regime.

Device	Γ_{21}	Γ_{20}	Γ_{10}	$\Gamma_{2\phi}$	$\Gamma_{1\phi}$	Ω_c	β	Regime (Ω_t)
3CP Low power	13.6	0*	1.07	0.94*	0.35	3.59	12.7	EIT (7.72)
3CP High power	8.92	0*	1.07	0.94	0.35	16.6	8.34	ATS (5.40)
6CP Low power	2.50	0.95	0.044	0.67	0.11	1.03	56.8	EIT (2.40)
6CP High power	3.93	0.06	0.044	0.48	0.047	2.50	89.3	ATS (2.48)

Table 5.2: Parameters extracted from fitting the transmission coefficient, obtained from the master equation in Eq. (5.10), to the measured data in Fig. 5.9. All values are in units of MHz. Values in squares were extracted independently from other measurements. Parameters marked by an asterisk were not varied during the fitting procedure.

that the two low-power measurements for both devices are in the EIT regime, the high-power measurement for the 6CP device is just at the border between the two regimes, and the high-power measurement for the 3CP device is in the ATS regime.

Akaike's Infomation Criteria for distinguishability

Anisimov et al. proposed using information-based model selection techniques to distinguish EIT and ATS based on the different predicted absorption profiles for the two processes [98]. The original proposal was to fit two functions: $A_{\mathrm{EIT}} = C_+^2/(\gamma_+^2 + \delta^2) - C_-^2/(\gamma_-^2 + \delta^2)$ and $A_{\mathrm{ATS}} = C^2\,(1/(\gamma^2 - (\delta - \delta_0))^2 + 1/(\gamma^2 - (\delta + \delta_0)^2))$, to the measured absorption spectrum, which is proportional to the real part of the reflection coefficient in our system. We see that the EIT model is formed by the difference of a broad and a narrow Lorentzian centered at the same frequency, whereas the ATS model is the sum of two otherwise identical Lorentzians centered at different frequencies. From the results of the two fits, we then calculate the Akaike information criterion (AIC) for the two models. The AIC is an unbiased estimator of the Kullback-Leibler distance between the proposed model distribution and an (unknown) "true" model distribution [101].

For a least-squares fit, the AIC is defined as $I = N\log(\hat{\sigma}^2) + 2K$ where K is the number of fit parameters, N is the number of data points, and $\hat{\sigma}^2 = \sum \epsilon_i^2/N$ with ϵ_i being the residuals of the fit. While I for a single model compares it to an unknown true distribution and therefore does not have an easy interpretation, the difference of I for two models has the straightforward meaning of the relative distance of the two models from the true one. In particular, the relative likelihood (probability) of two models is simply given by $\exp(-\Delta_{ij}/2)$ where we define the (positive) Akaike difference $\Delta_{ij} = I_i - I_j$ with I_i the AIC of the i-th model. This relative likelihood is often expressed in a normalized

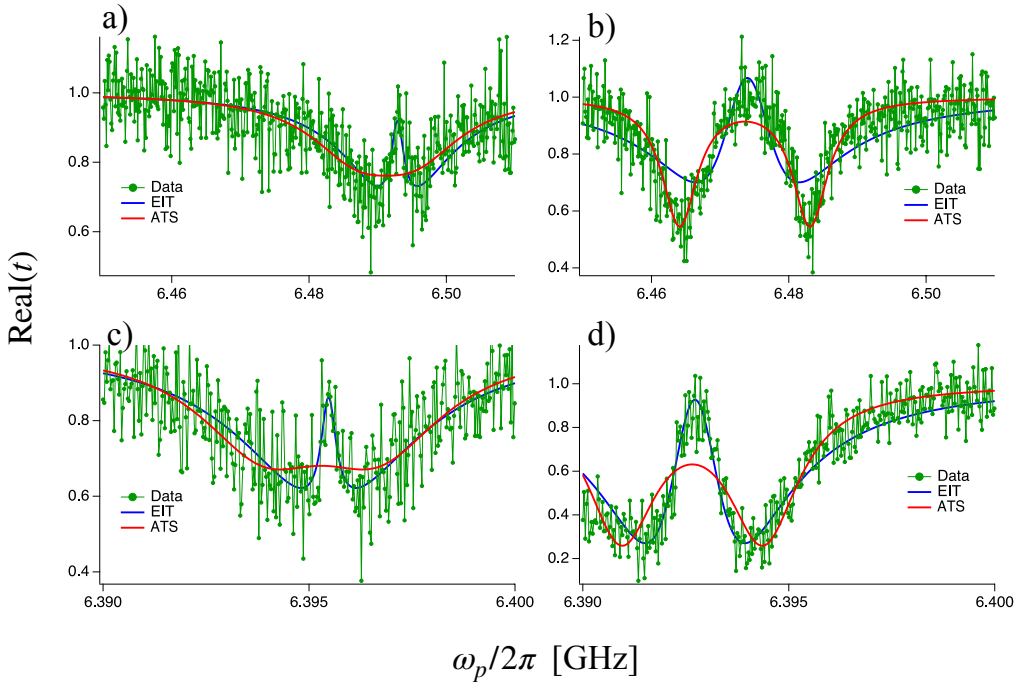

Figure 5.11: Model selection based on Akaike's information criterion. We compare the best fits of an EIT and ATS model to the measured absorption profile, Real(t). In the low-power regime of both (a) the 3CP and (c) the 6CP device, the ATS model does not capture the narrow transparency window which is observed, while the EIT model does. The same is true, although to a lesser extent, for the high-power measurement of the 6CP device shown in (d). This failure is captured in the very small relative likelihood of the ATS model, $< 10^{-7}$ in all three of these cases. The ATS model better captures the broad transparency feature observed in the high-power measurement of the 3CP device shown in (b), with a relative likelihood of 10^{-30} for the EIT model. The data in these figures is unsmoothed, in contrast to Figs. 5.9 and 5.10 above, because the correlations introduced by smoothing violate the assumptions made to derive the maximum-likelihood estimator used in the AIC analysis.

form known as Akaike weights, w_i, such that the ratio of the weights $w_i/w_j = \exp(-\Delta_{ij}/2)$ gives the relative likelihood of the two models.

In the original proposal to use Akaike's information criterion to distinguish between EIT and ATS [98], the fitting functions described the absorption spectrum. Here, the equivalent quantity is the real part of the reflection coefficient. We are not, however, measuring the reflection coefficient directly, but we can still follow the original proposal by using the relation $t = 1+r$. Before we fit A_{EIT} and A_{ATS}, mentioned above, to the measured spectra, we do two things: we apply a rotation of the data in order to account for phase shifts induced by propagation delays, and we normalize the data using the amplitude that was extracted from the master-equation simulation. We use the transmission co-efficient data in the linecuts presented in Fig. 5.9 and Fig. 5.10 to calculate the Akaike weights for each measurement. The data and the fits can be seen in Fig. 5.11.

For the two low-power measurements, Fig. 5.11 (a) and (c), we find that the EIT model clearly fits better with the relative likelihood of the ATS model being $w_{\mathrm{ATS}}/w_{\mathrm{EIT}} = 10^{-7}$ and $w_{\mathrm{ATS}}/w_{\mathrm{EIT}} = 10^{-8}$, respectively. For the high-power measurement of the 3CP device in Fig. 5.11(b), with an extracted drive strength well into the ATS regime, the ATS model was strongly favored with the relative likelihood of the EIT model being $w_{\mathrm{EIT}}/w_{\mathrm{ATS}} = 10^{-37}$. For the high-power measurement on the 6CP device in Fig. 5.11(d), which had an extracted drive strength near the threshold, the EIT model was also strongly favored with $w_{\mathrm{ATS}}/w_{\mathrm{EIT}} = 10^{-30}$. We note that this relative likelihood more strongly favors the EIT model than in the low-power measurements, even though it is near the threshold. Despite this, we can see that the best-fit EIT and ATS curves look qualitatively very similar for this case. The fact that the relative likelihoods are much smaller for the two high-power cases may simply be due to the lower signal-to-noise ratio of the low-power measurements.

5.6 Chapter conclusions

In conclusion, we have demonstrated giant artificial atoms in a superconducting waveguide-QED setting. We demonstrated that the giant-atom effects allowed us to modulate the coupling strength of the $|0\rangle - |1\rangle$ transition with an on-off ratio as high as 380. We also showed that we can enhance or suppress the coupling of the $|1\rangle - |2\rangle$ transition relative to the $|0\rangle - |1\rangle$ transition, with a modulation range greater than a factor of 200. This allowed us to engineer the giant transmon into an effective lambda system with a metastable excited state. To further validate this, we clearly demonstrated EIT in our giant transmon, thus benchmarking the quality of our lambda system. The presence of EIT in our system was verified both by detailed fitting to a master-equation model and by model-selection

techniques based on the Akaike information criterion. Our work helps establish giant artificial atoms as a new paradigm in waveguide QED and microwave quantum optics.

Chapter 6

Two-giant artificial atoms in a braided configuration

In the previous chapter, we saw the characterization of our single-giant transmon qubit with three and six coupling points to a 1D open TL. In this chapter, we will look at some initial first results on characterizing a device with two-giant transmon qubits which are configured in a braided configuration as discussed in Chapter 2. This work, still ongoing at the time of writing this thesis, demonstrates some striking new signatures which are very different from the case of having just two simple artificial atoms coupled to a 1D TL.

So far, majority of the experiments conducted using multiple artificial atoms in waveguide QED have focused on using simple atoms [9]. Among the many interesting effects, these systems have been successful in demonstrating waveguide-mediated interactions between two spatially separated simple qubits coupled to a TL [22]. With the spatial distance, λ_0, between the qubits fixed by design, the authors show that by bringing the qubits into resonance at two specific frequencies corresponding to $3\lambda_0/4$ and λ_0, they could demonstrate two situations where the exchange interaction between the qubits is enhanced while their correlated decay into the TL was suppressed and vice versa. This led to the growing interest of exploring similar multi-qubit waveguide-QED setups [23, 102].

Although, engineering photon mediated interactions between spatially separated simple qubits is interesting from a perspective of quantum optics and quantum communication, the qubits still interact in a decoherence-limited subspace, i.e, while their collective decay can be made zero, their individual decay into the TL is still finite. As we saw earlier in Chapter 2, the braided configuration of giant artificial atoms allows the qubits to interact in a complete decoherence-free space wherein both the individual and collective decay can

be engineered to be zero. Motivated by this, we consider the case of two braided-giant transmon qubits each with two coupling points to a TL, as discussed in Chapter 3. We characterize the qubits using continuous frequency domain techniques, similar to those employed in Chapter 5.

6.1 Scattering properties of two braided-giant transmons

We begin characterizing the braided giant transmons by bringing them into resonance with each other and measuring the transmission coefficient t of a weak probe field propagating along the TL. If the qubits are interacting, we expect to see an avoided-level crossing in the spectroscopy data. In our measurement setup, we have a single coil which is mounted to the sample box. Using this global field, we can tune both our qubits in our measurement band. However, in order to selectively tune one of the qubits into resonance with the other, we make use of an additional on-chip flux bias line. The local field from the flux line together with a global field allows us to resonantly operate the qubits at different frequency bias points.

6.1.1 Effect of screening currents on flux tuning of qubits

In this section, we will explore some possible causes of experimental deviation that we observe in the tuning behavior of the qubits which can be linked to the nature of screening currents generated in the superconducting aluminum film of the CPW ground planes when an external field is generated by the global flux coil. We will compare two design scenarios in two separately measured braided giant transmon devices.

Device 1: Similar $E_J^{\max}$ and E_c, different SQUID loop areas

As discussed in Chapter 3, qubit B has a SQUID loop area which is 1.5 times that of qubit A but the Josephson junctions and the capacitance electrodes for both qubits are nominally identical. The areas were designed this way in order to have their resonance frequencies cross each other near $\omega_\lambda^{\mathrm{B}}$ using the global field alone, where the superscript BGT refers to the braided-giant transmon (see Chapter 2). Ideally, if the flux offsets in both qubits is zero, then the crossing would happen near $\omega_\lambda^{\mathrm{B}}$. However, in the experiment we observe different flux offsets for both qubits with the maximum frequencies at zero flux

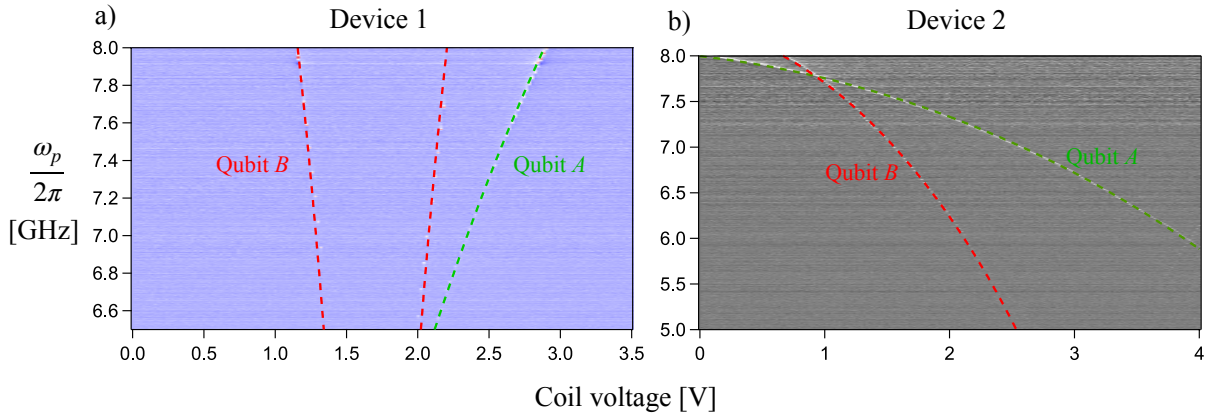

Figure 6.1: Global flux tuning of braided giant transmons in two measured devices. (a) Transmission spectroscopy for device 1, showing $|t|$ of the TL as a function of probe frequency for different coil voltages. Both qubits have similar E_c and $E_J^{\max}$ and tune over a wide range of frequency. The SQUID area of qubit B is 1.5 times larger than that of qubit A. (b) In device 2, the SQUID in both qubits has a lower $E_J^{\max}$ than device 1. Both qubits have similar E_c and $E_J^{\max}$ and the SQUID area in both qubits is the same.

bias being roughly the same. Figure 6.1(a) shows the tuning curve for both qubits using the global field coil with different flux offsets for device 1. It is clear from the figure that our qubits tune with external flux.

The sensitivity of each qubit to the external magnetic flux applied by the global coil depends on the mutual inductance between the coil and the SQUID loop. In order to characterize this, we can write the external flux Φ_i for qubit $i \in (A, B)$ in terms of the coupling matrix K_{ij} for coil j ($j = 1$ as we have a single global coil), the coil voltage V_j and the flux offset Φ_i^0 as:

$$\begin{pmatrix} \Phi_A \\ \Phi_B \end{pmatrix} = \begin{pmatrix} K_{A1} \\ K_{B1} \end{pmatrix} (V_1) + \begin{pmatrix} \Phi_A^0 \\ \Phi_B^0 \end{pmatrix}. \tag{6.1}$$

The dash-color lines for the two qubits in Fig. 6.1 are calculated tuning curves by substituting Eq. (6.1) in the Josephson energy term in Eq. (2.12). The theory curves are appended onto the experimental plot using $E_c/h = 540$ MHz which was separately measured using the two-tone spectroscopy technique as discussed in the previous chapter. The values of $E_J^{\max}$, coupling constants and the flux offsets have been chosen to properly align the theory curves with the experimental data in order to get the best visual match.

We can also define a relative-flux sensitivity for the two qubits as $\kappa = K_{B1}/K_{A1}$. Ideally,

$\kappa = 1.5$ as the sensitivity of the two qubits A and B to the global coil flux is given by the ratio of their respective SQUID loop areas. But experimentally we find that $\kappa = 4.2$, a clear deviation from the factor 1.5. In order to see why this could possibly be the case, let us look at the surrounding geometry of the CPW ground planes near the two qubits which is shown in Fig. 6.2 where (a) shows the fabricated design of qubit A and (b) refers to qubit B. The SQUID arm of the qubit is shown in red and the capacitance electrode of the transmon is shown in green.

Consider an external field $\vec{B}$ (out of the plane of paper) which is applied by the coil as shown in Fig. 6.2. This results in screening currents that are generated in the CPW ground plane as shown by the circular arrows in order to counter $\vec{B}$. Therefore, the net flux seen by the SQUID loop is diluted by these currents. However, the empty pocket seen in the ground plane surrounding qubit B reduces the effect of the screening current by moving it away from the SQUID, thereby making qubit B much more sensitive to flux than qubit A. We believe, this asymmetric geometry of the ground plane around the SQUID loop gives qubit B additional sensitivity to flux which could explain why $\kappa = 4.2$.

Device 2: Similar $E_J^{\max}$ and E_c, same SQUID loop areas

Now, let us consider another device that was measured after the one discussed in the previous section. Both qubits in this device have the same SQUID loop area with identical Josephson junctions designed to give us a lower $E_J^{\max}$ than device 1. Although, the junction geometry is different than device 1, the SQUID areas for both qubits in device 2 are the same as qubit A of device 1. Figure 6.1(b) shows the experimental data and the calculated tuning curves which are appended onto the plot for the best visual match for device 2. Since the zero-bias frequency for both qubits is below 8.5 GHz, we were able to measure it directly. The capacitance electrodes for the qubits and the ground plane geometry are the same as device 1 (see Fig. 6.2) which gives us the same anharmonicity as before. We independently verify this using two-tone spectroscopy discussed in Chapter 5. The flux offsets and the coupling constants are calculated in the same way as discussed before. Since this device was measured in a similar experimental setup with a different global coil, the absolute value of the coupling constant K_{A1} for qubit A differs from that of device 1. We see from the extracted flux coupling constants that $\kappa = 2$ which can be understood in the same way as presented in the previous section. Although, ideally this factor should be 1 as the SQUID loop areas for both the qubits are the same, the deviation we see can be attributed to the effect of the screening currents in the vicinity of the SQUID for qubit B.

The tuning profile of the qubits from this device further strengthens our hypothesis about the effect of screening currents. It also points towards careful layout choices that

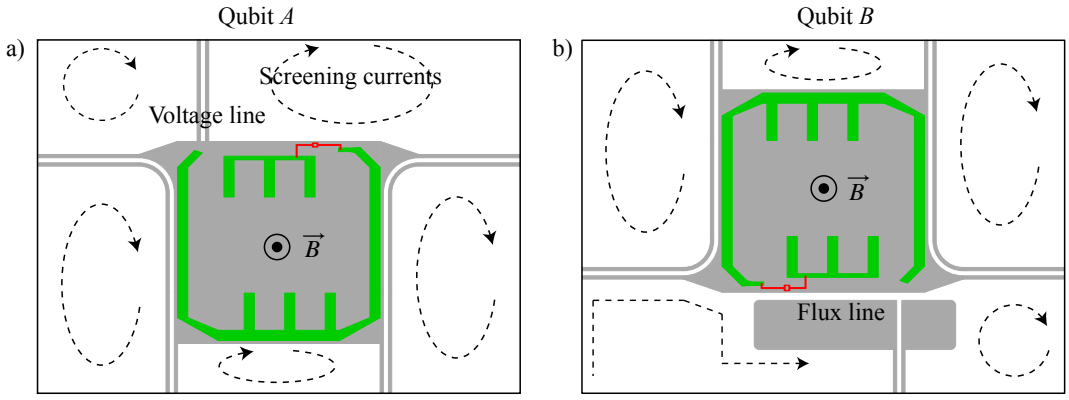

Figure 6.2: Effect of screening currents on flux tuning of the giant transmon qubits. (a) Close up CAD layout of qubit A showing its coupling sites to the TL and a dedicated voltage line (although not used in the measurements). When an external field $\vec{B}$ is applied using the coil, screening currents flow in the superconducting ground planes to counter the applied field. The sensitivity of the SQUID to the applied flux is reduced due to the screening currents in the ground plane near its vicinity. (b) Qubit B has a dedicated flux line, which is used to tune its frequency by applying a local DC field. A pocket is opened in the ground plane of the flux line to ensure that the DC current flows uniformly through the flux branch. Due to the pocket, the screening current in the ground plane flows away from the SQUID. This ensures a larger effective field near the vicinity of the SQUID, making it more sensitive to the applied field. If the SQUID area of both qubits is the same, qubit A has a lower sensitivity to the applied field than qubit B, due to the effect of screening currents.

one must consider to implement whenever global flux biasing using an external coil is required for such experiments. For all subsequent measurements discussed in this chapter, we will be using the data from device 1.

6.1.2 Qubit-qubit spectroscopy using the TL

In Section 3.2.1, we discussed the design parameters for the braided-giant transmon device. To recall, the decoupling-frequency bias point for the qubits is at $\omega_\lambda^{\mathrm{B}}/2\pi \approx 5.91$ GHz. In this section we will look at spectroscopy of the two qubits near 6.3 GHz and 7.7 GHz using device 1 from the previous section. The choice of these frequencies was made by the crossing points of the qubits using the global coil. The local flux line gives us a tuning of

$\sim$ 500 MHz for qubit B at which point the DC current in the line begins to heat up the mixing chamber of our fridge. For the frequency bias points considered, we operate the local flux current well below this threshold.

Qubits near 6.3 GHz

We begin by weakly probing the qubits using single-tone transmission spectroscopy after bringing them close enough using a static global flux. The probe excites both qubits through the TL. Figure 6.3(a-d) shows the simulated and the measured magnitude ($|t|$) and phase (θ_t) of t as qubit B is brought into resonance with qubit A near 6.3 GHz, which is the closest crossing point to $\omega_\lambda^{\mathrm{B}}/2\pi$ in this device. The phase acquired between the coupling points is $\phi = 0.54\pi$. The simulated plots (top row) are added here for clarity and are discussed in Chapter 3 where the resonance frequency of qubit B is varied by sweeping its inductance L_J^B in HFSS. In the measurement, we use the local flux line to tune the frequency of qubit B. We see good qualitative agreement between the simulated and the measured results.

When the qubits are off-resonant as shown by the linecut from the 2D plot (black arrow) in Fig. 6.3(e-f), they behave as individual qubits which are coupled to the TL, each showing extinction in $|t|$ and separate phase signatures. Using Eq. (2.39), we extract the individual relaxation rates $\Gamma_{10}^A/2\pi = 3.42$ MHz and $\Gamma_{10}^B/2\pi = 3.62$ MHz for qubit A and B respectively from the off-resonant linecut data. The extracted dephasing rates for the two qubits are $\Gamma_\phi^A/2\pi = 821$ kHz and $\Gamma_\phi^B/2\pi = 719$ kHz respectively.

For the resonant case, we do not observe an avoided-level crossing in the spectroscopy data as shown by the linecut from the 2D plot (pink arrow) in Fig. 6.3(e-f). Instead, we observe a single resonance feature both in $|t|$ and θ_t which suggests that the resonant qubit-qubit system now behaves like a single qubit. We also observe that the resonant feature exhibits stronger extinction in $|t|$ as compared to when the qubits are off-resonant with a collective relaxation rate, $\Gamma_{10}^{\mathrm{coll}} = 7.2$ MHz. The phase signature also shows a strongly-coupled behavior when compared to the off-resonant case. It is interesting to note here that $\Gamma_{10}^{\mathrm{coll}}$ is twice that of the off-resonant relaxation rate of the two qubits. This behavior was also seen in [22], where their qubit-qubit system was in a superradiant (bright) state, $|B\rangle = (|ge\rangle + |eg\rangle)/\sqrt{2}$.

Qubits near 7.7 GHz

The situation gets more interesting when the qubits are biased $\sim$ 7.7 GHz where the phase acquired between the coupling points is $\phi = 0.65\pi$. We perform similar single-tone

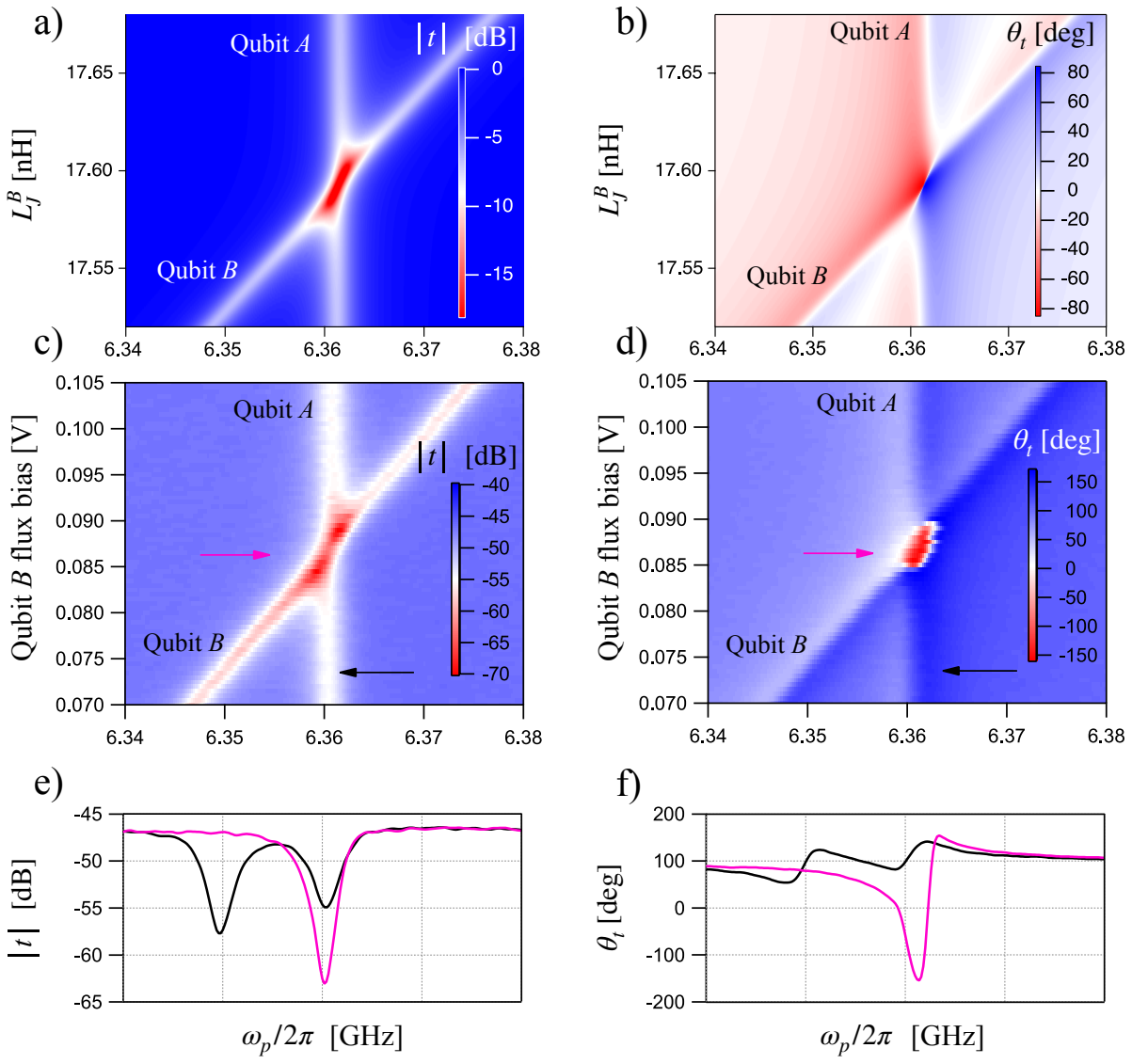

Figure 6.3: (a) $|t|$ and (b) θ_t obtained using an HFSS simulation of the measured device near 6.3 GHz, as discussed in Chapter 3. The plots are added here for clarity. (c) and (d) are the measured $|t|$ and θ_t where qubit B is brought into resonance with qubit A using the local flux line. (e) and (f) are the corresponding linecuts from the measured data at the flux bias locations indicated by the arrows.

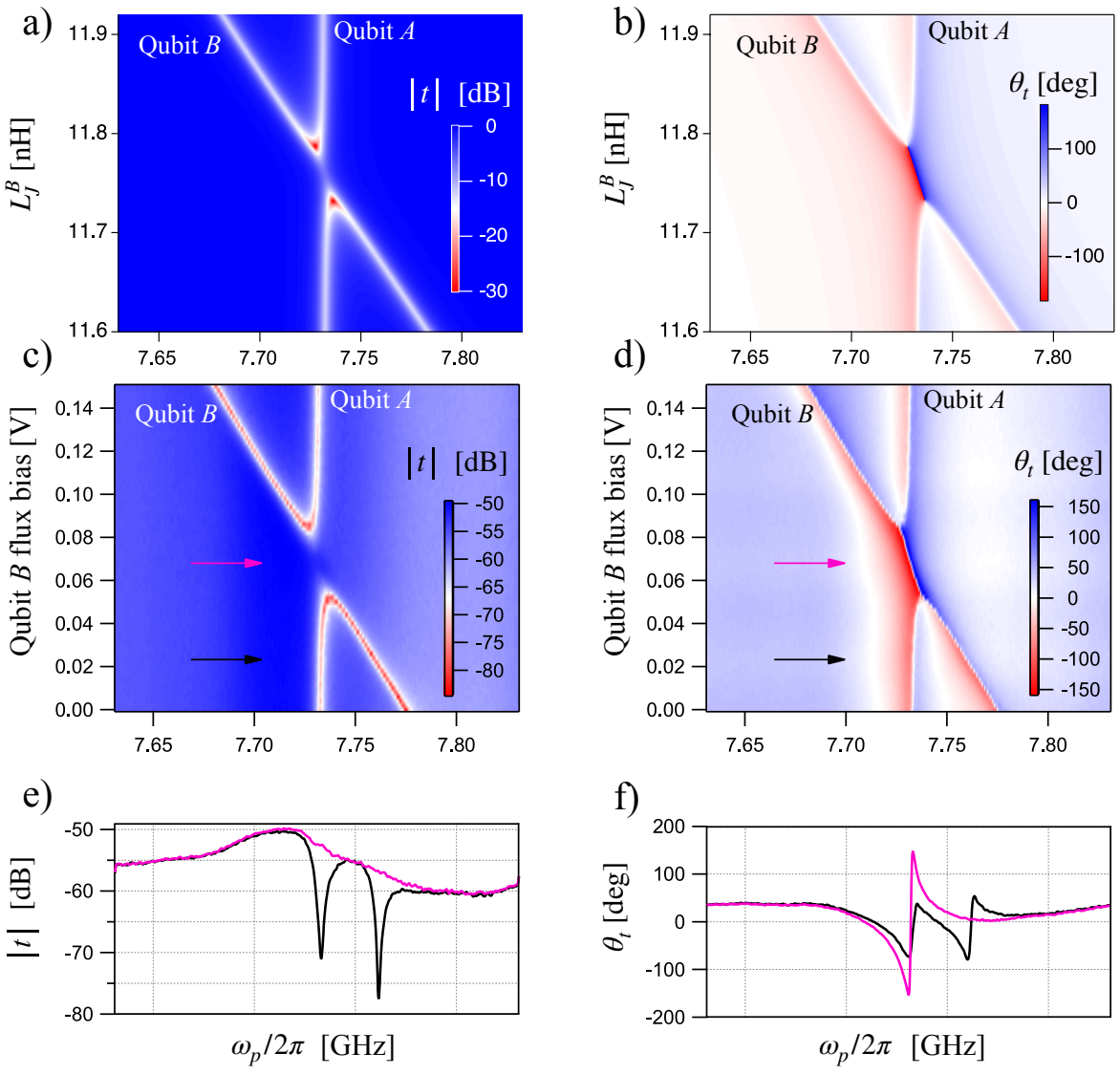

Figure 6.4: (a) $|t|$ and (b) θ_t obtained using an HFSS simulation of the measured device near 7.7 GHz, as discussed in Chapter 3. The plots are added here for clarity. (c) and (d) are the measured $|t|$ and θ_t where qubit B is brought into resonance with qubit A using the local flux line. (e) and (f) are the corresponding linecuts from the measured data at the flux bias locations indicated by the arrows.

spectroscopy measurements as described before using a static global flux to bias the qubits ~ 7.7 GHz and sweeping the local flux on qubit B to bring them into resonance with each other. The simulated and the measured results qualitatively agree well and are shown in Fig. 6.4.

When the qubits are off-resonant, we see a similar behavior as before. But when they are brought into resonance with each other, we observe an interesting effect. From the resonant line cuts in Fig. 6.4(c-d), we observe full transmission in the magnitude response with a single strongly-coupled phase signature. This happens for a range of flux bias values, a situation quite different from when the qubits were biased ~ 6.3 GHz. We extract the individual relaxation rates, $\Gamma_{10}^{A}/2\pi = 10.15$ MHz and $\Gamma_{10}^{B}/2\pi = 13.32$ MHz for qubit A and B respectively using Eq. (2.39). The dephasing rates are $\Gamma_{\phi}^{A}/2\pi = 635$ kHz and $\Gamma_{\phi}^{B}/2\pi = 234$ kHz.

We believe this could be indicating novel physics in the system at this frequency bias point. To explore further, we will have to measure the reflection coefficient, r, along with t. The simulated r is shown in Chapter 3.

6.1.3 Multiple resonances in Autler-Townes Splitting

In Section 5.4.2, we looked at how to observe the Mollow triplet and the ATS, in the context of a single artificial atom coupled to a TL. We recall that, the qualitative signatures are a triplet in the Mollow spectrum and a doublet in the ATS spectrum. In this section, we will explore the same with our braided giant transmons by looking at how these signatures differ for both the resonant and the off-resonant cases. We find some surprising additional resonances in the ATS and not the Mollow triplet, which is interesting and hence we will be focussing on the former.

For the off-resonant case, we bias qubit B near the frequency point of interest and tune qubit A roughly a GHz away from qubit B. For the resonant case, we bias both qubits at the same frequency and perform ATS. To observe ATS, we use the same driving scheme discussed in Section 5.4.2 but instead of pumping the $|1\rangle - |2\rangle$ transition on resonance, we sweep the pump tone near $\omega_{21}/2\pi$ for a fixed pump power and probe the $|0\rangle - |1\rangle$ transition weakly. The pump power chosen is ~ 20 dB stronger than the probe power.

ATS near 6.3 GHz

Similar to the previous section where we compared transmission spectroscopy of the qubits near 6.3 GHz and 7.7 GHz, here we compare the nature of ATS near these frequency

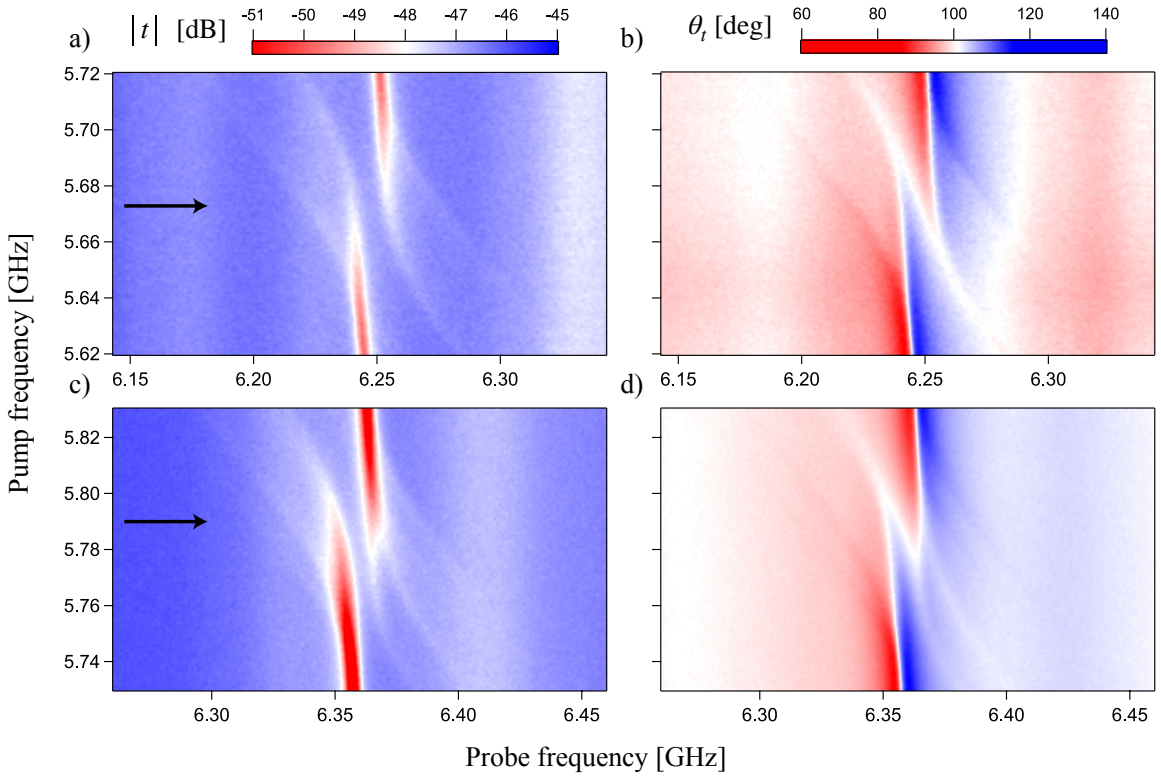

Figure 6.5: ATS for off- and on-resonant cases for the braided giant transmons near 6.3 GHz. (a) ATS for the off-resonant case performed on qubit B when qubit A was biased outside the measurement band. The color in the 2D plot indicates $|t|$ measured as a function of probe frequency. The pump which excites the $|1\rangle - |2\rangle$ transition is held at a fixed power and its frequency is swept on the Y-axis. When the pump tone is on resonant with the $|1\rangle - |2\rangle$ transition (indicated by the black arrow), we see a four resonance feature instead of the familiar doublet. (b) The corresponding θ_t for the off-resonant case. (c) and (d) shows $|t|$ and θ_t for the on-resonant case, where both qubits were biased at the same frequency. The ATS in this case reveals more than four resonance features when the pump tone is at the $|1\rangle - |2\rangle$ transition for both qubits.

bias points. Figure 6.5 shows $|t|$ and θ_t characterizing ATS observed for the off-resonant (Fig. 6.5(a-b)) and the resonant case (Fig. 6.5(c-d)). This frequency bias point, which is closer to $\omega_\lambda^{\mathrm{B}}/2\pi$, shows some surprising spectroscopic features for ATS. For the off-resonant case, i.e, characterizing ATS for qubit B alone, one would expect to see a familiar doublet feature which corresponds to the dressing of the $|1\rangle$ level by the pump tone. However, when the pump frequency is resonant with $\omega_{21}/2\pi$, we clearly see four resonance features instead of the typical two (doublet).

For the resonant case, i.e, when both qubits A and B are at resonance with each other, performing a similar measurement reveals even more resonance features. At first sight, this might seem to be due to differences in the anharmonicity of the two qubits, which when on resonance, could give rise to additional couplings between the levels. However, in a series of separate measurements (not discussed here), we verified that the anharmonicity of the two qubits at different frequency bias points is nearly the same. This is expected as both qubits have the same capacitor design.

ATS near 7.1 GHz

We now compare the ATS measurements for the resonant and off-resonant cases near 7.1 GHz. Figure 6.6 shows $|t|$ and θ_t for both the off-resonant and the resonant case. In the off-resonant case, we see a familiar doublet. When the qubits are on resonance with each other (see Fig. 6.6(c-d)), we see four-resonance features in the spectroscopy signatures. Although, the anharmonicity of the two qubits were measured to be nearly the same, the origin of these multiple resonances here and in the previous resonant case needs to be understood further. Perhaps, in the theoretical model we could consider the anharmonicity to be unequal to rule out the possibility.

6.2 Chapter conclusions

To summarize, we have presented preliminary results of the scattering properties of the braided giant transmons using single-tone transmission spectroscopy. Our results show interesting qubit-qubit resonant behavior at two different frequency bias points, 6.3 GHz and 7.7 GHz.

When the qubits are off-resonant with each other, we observe the typical scattering from a qubit coupled to a TL showing extinction in the magnitude of the transmission coefficient irrespective of the frequency bias point. However, the resonant response shows distinct

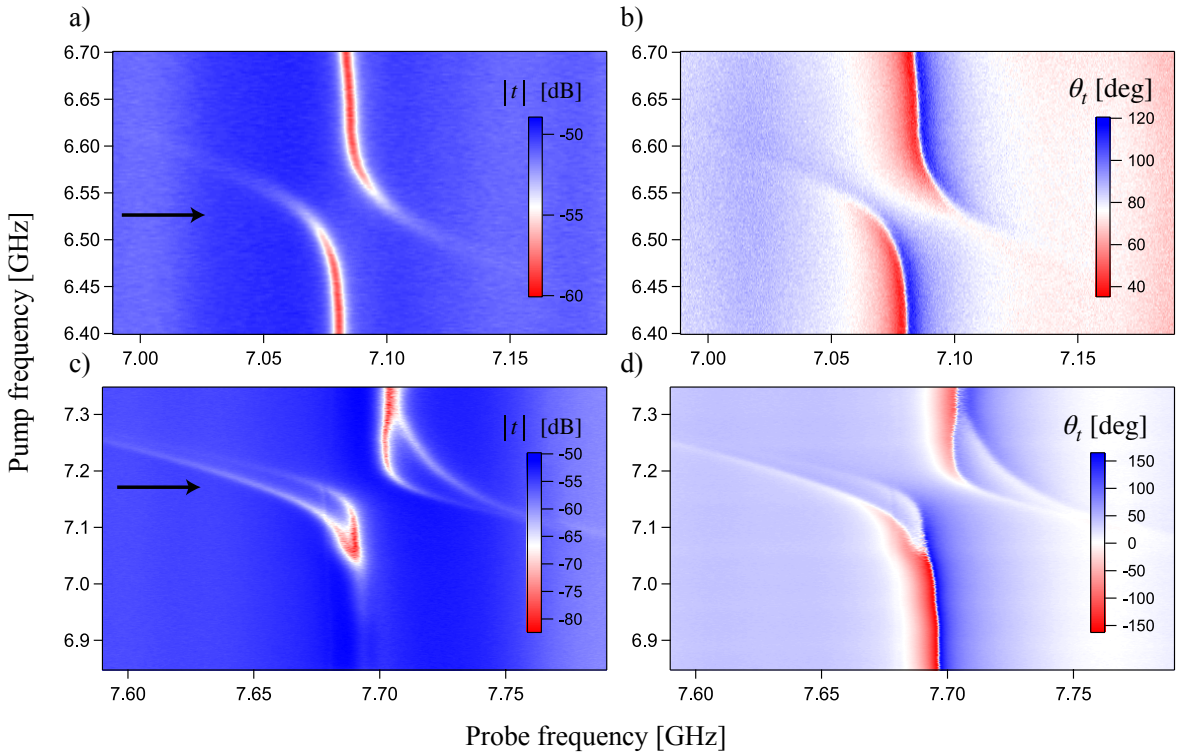

Figure 6.6: ATS for off- and on-resonant cases for the braided giant transmons near 7.7 GHz. (a) ATS for the off-resonant case performed on qubit B when qubit A was biased outside the measurement band. The color in the 2D plot indicates $|t|$ measured as a function of probe frequency. The pump which excites the $|1\rangle - |2\rangle$ transition is held at a fixed power and its frequency is swept on the Y-axis. When the pump tone is on resonant with the $|1\rangle - |2\rangle$ transition (indicated by the black arrow), we see a familiar doublet in ATS measurement, unlike the four resonance features seen before. (b) The corresponding θ_t for the off-resonant case. (c) and (d) shows $|t|$ and θ_t for the on-resonant case, where both qubits were biased at the same frequency. The ATS in this case reveals four resonance features when the pump tone is at the $|1\rangle - |2\rangle$ transition for both qubits.

features, i.e, we observe strong extinction near 6.3 GHz and full transmission near 7.7 GHz. Although, we do not observe resonant scattering from the qubits near 7.7 GHz, we see a distinct signature of the qubit-qubit joint state in the phase response of the transmission coefficient. Our HFSS simulation of the measured device successfully captures the features we observe in the transmission spectroscopy. We also observe additional resonance features when characterizing the ATS for the off-resonant qubit near 6.3 GHz which we don't see near 7.7 GHz for the same qubit. For the resonant case, we again see multiple resonances in the ATS at both the frequency bias points.

Going forward, we plan to simultaneously measure both the reflection and the transmission coefficient for the device which will help us better understand the observed features. Ongoing theoretical investigation with our collaborators also indicate the possibility of the existence of exceptional points in this system. Exceptional points are singularity points in the system Hamiltonian with degenerate Eigenstates where the system is critically damped.

The challenges we faced due to flux biasing of qubits can also be solved by making the CPW ground plane topology identical for both qubits. In hindsight, we feel that it is easier to access more frequency crossing points by simply making the qubits degenerate and using the local flux line on one of the qubits to tune them into resonance with each other. Incorporating dedicated readout resonators for the qubits also provides a way to characterize them in the time domain.

Chapter 7

Parametrically-coupled superconducting cavities

We summarize the main results of the experiment involving two parametrically-coupled superconducting cavities in this chapter. The device is composed of a high frequency $\lambda/4$ resonator whose frequency can be tuned using a SQUID. The SQUID magnetically couples to a low-frequency $\lambda/2$ resonator, which has a fundamental frequency of ~ 280 MHz. The $\lambda/2$ resonator is implemented as a novel band-stop filter, where its higher-harmonic resonant modes are suppressed in the 4-8 GHz measurement band. The interaction Hamiltonian, discussed in Chapter 2, is that of an optomechanical-like coupling where the current in the $\lambda/2$ resonator couples to the energy of the $\lambda/4$ resonator. We demonstrate signatures of this coupling behavior, where we indirectly read out the $\lambda/2$ cavity using the $\lambda/4$ resonator.

7.1 High-frequency SQUID-terminated $\lambda/4$ resonator

We begin by characterizing the $\lambda/4$ resonator by measuring its single-port reflection coefficient r using a VNA at room temperature. The circulators used in the setup, shown on the left in Fig. 4.7, separates the input and the reflected fields of the $\lambda/4$ resonator, which can then be used to measure r. The resonator's bare resonance frequency calculated from its CPW length alone is 7.875 GHz. In our experiment, the resonance frequency is affected by the input coupling capacitor C_c and the finite inductance L_{sq} of the SQUID. If the SQUID inductance is not taken into consideration, the large coupling capacitor loads

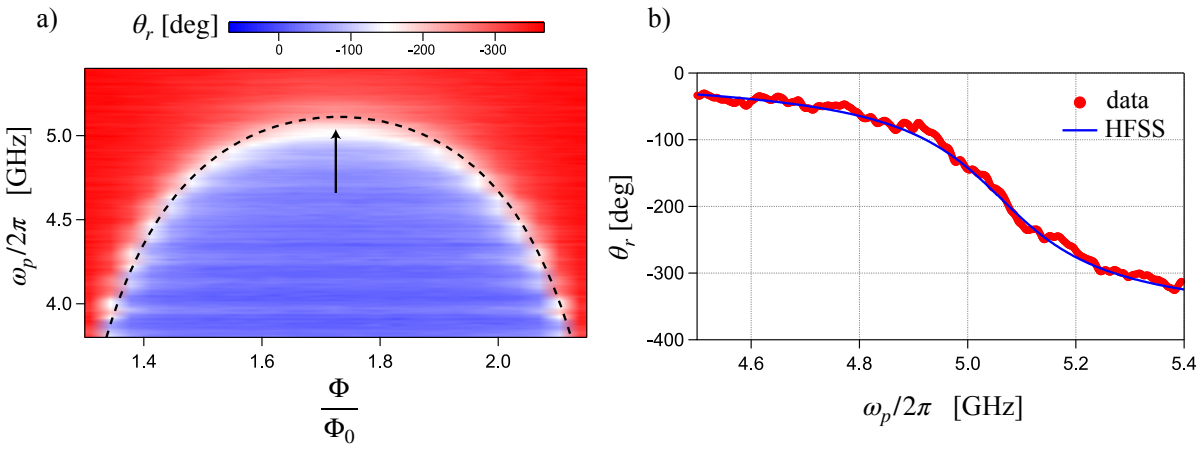

Figure 7.1: Frequency tunability of the $\lambda/4$ resonator, which is terminated by a SQUID. (a) Phase, θ_r, of the reflection coefficient r as a function of probe frequency (Y-axis) for every external flux bias Φ/Φ_0 (X-axis). The value of Φ is changed using an external coil attached to the sample box. Φ_0 is calibrated in terms of coil voltage from multiple multiple periods of the tuning curve (not shown here). There is a background flux offset which is not accounted for. The dashed line is a numerically calculated using Eq. (2.34) and is added on top of the 2D plot. (b) A line cut at the indicated flux bias point (arrow) shows an over-coupled phase response of the resonator.

the resonator, bringing its resonance frequency further down to 6.4 GHz, which is observed in both numerical and HFSS simulation. If the SQUID inductance is considered, the resonator has an even lower resonance frequency of ~ 5.1 GHz. Using the coil attached to the sample box, we can tune the resonance frequency of the $\lambda/4$ resonator in our measurement band.

Figure 7.1(a) shows the frequency tuning characteristics of the resonator for every normalized flux bias Φ/Φ_0 with a maximum frequency of ~ 5.1 GHz. The color indicates the phase of the reflection coefficient $\theta(r)$. We use multiple periods of the tuning curve to characterize Φ_0 with a flux offset ($\sim 0.25\Phi_0$) at zero bias condition. The solid dashed-line is a manual fit using Eq. (2.34), which considers the effect of both the inductive and capacitive loading from the SQUID and the coupling capacitor, respectively. For the fit, we use $C_c = 160$ fF (obtained from Q3DExtractor), resonator length $l_{\lambda/4} = 3.75$ mm (obtained from CAD layout), the maximum SQUID inductance $L_{\rm sq}^{\rm max} = 507$ pH (obtained from room temperature resistance of the SQUID) and $Z_0 = 50\ \Omega$. Figure 7.1(b) shows the linecut at the flux bias condition, which corresponds to the maximum resonance frequency as

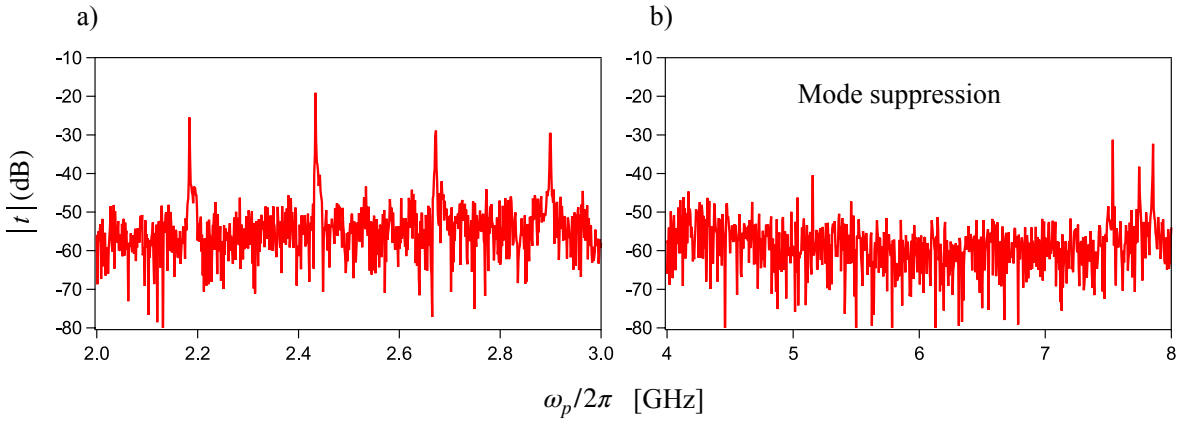

Figure 7.2: Mode characterization of $\lambda/2$ resonator. (a) $|t|$ of the transmission coefficient of the $\lambda/2$ resonator showing the higher harmonics of its fundamental mode. The separation between the modes is $\sim$ 250 MHz. (b) Due to the bandstop nature of the resonator, we see active mode suppression in the $\sim$ 4-8 GHz as designed.

indicated by an arrow in Fig. 7.1. The solid line is the result of the HFSS simulation of the $\lambda/4$ resonator using the same parameters discussed above, showing good agreement with the measured data. Both data and simulation results show the unwrapped phase with a swing of 360° at resonance, a typical signature for an over-coupled $\lambda/4$ resonator measured in reflection. We choose to show the phase response in Fig. 7.1 as we do not observe a signal in the magnitude response due to this over-coupled behavior. The simulated loaded quality factor, $Q_{\mathrm{L}} = 17.6$, is obtained from the frequency points corresponding to the $\pm 90°$ of the phase response giving us a bandwidth $\Delta f = 290$ MHz. Our results satisfy the design goals for the bandwidth requirement of the $\lambda/4$ resonator and its frequency-tunability, intended for its role as a photonic piston described in Chapter 2.

7.2 Low-frequency bandstop $\lambda/2$ resonator

To characterize the low-frequency bandstop $\lambda/2$ resonator, we measure its two-port transmission coefficient t using a VNA. We employ a microwave switch at the base temperature stage to share the output line of our measurement chain with both the $\lambda/2$ and $\lambda/4$ resonator, as shown in Fig. 4.7. The HEMT amplifier used in this measurement has a bandwidth of 4-8 GHz. Due to this constraint, we were able to directly measure the higher

harmonics of the $\lambda/2$ resonator from 2-8 GHz. Although this is outside the lower-cutoff frequency of the amplifier, the finite roll-off of its gain is still sufficient to see the modes below 4 GHz up to a frequency where the signal is visible.

Figure 7.2(a) shows the measured t (dB) of the higher harmonic modes of the $\lambda/2$ resonator from 2-3 GHz. The spacing between the modes is $\sim$ 250 MHz, which gives us an approximate likelihood of its fundamental resonance frequency. Due to the stepped-impedance design of the $\lambda/2$ resonator (see Chapter 3), the modes are not equally separated, an attractive feature to implement multi-mode anharmonic circuits. Another striking feature of this design, which is more relevant to our design goal, is the active suppression of the modes in the 4-8 GHz band. This is shown in Fig. 7.2(b), where the modes are absent to a large extent. The center frequency for the bandstop filter action was designed to be at 6 GHz. The bandstop nature of the $\lambda/2$ resonator ensures that its higher-order modes in the vicinity of the $\lambda/4$ resonator are actively suppressed. The experimental data clearly validates our design methodology. By exploring different design variations, the bandstop $\lambda/2$ resonator has the potential for complementing other multi-mode cavity experiments, where both anharmonicity and filtering is desired. Our simulations (not discussed in this thesis) also suggests that the same bandstop action is apparent even when the resonator is replaced by a transmission line with the appropriate length.

7.3 $\lambda/2$ resonator readout using parametric swap drive

The amplifiers in our measurement chain cannot be used to directly measure the fundamental frequency $\omega_{\lambda/2}$ of the $\lambda/2$ resonator. For this, we make use of the parametric coupling between the $\lambda/2$ and the $\lambda/4$ resonators. To implement this coupling scheme, the SQUID is galvanically connected to the ground plane, which is shared by both resonators. The nonlinear nature of this coupling, discussed in Chapter 2, allows an indirect readout of $\omega_{\lambda/2}$ using the $\lambda/4$ resonator. We achieve this by applying a strong swap drive, $\omega_s = \omega_{\lambda/4} - \omega_{\lambda/2}$, at the red-detuned frequency between the two modes, injected directly at the input of $\lambda/4$ resonator. In the rotating frame of the drive field, the interaction Hamiltonian, described by Eq. (2.44), takes the form of the standard Jaynes-Cummings model,

$$H_{\text{int}}/\hbar = g(\tilde{a}^\dagger b + \tilde{a} b^\dagger) \tag{7.1}$$

where $a^\dagger(b^\dagger)$ and $a(b)$ represents the creation and annihilation operators of the $\lambda/4(\lambda/2)$ resonator, $g = g_0\alpha_s$ is the enhanced coupling strength due to the swap drive amplitude α_s and $\tilde{a} = a - \alpha_s$ is the field operator describing the fluctuations of the coherent swap drive field such that $\langle a \rangle = \alpha_s$. The amplitude of the swap drive, $\alpha_s = \sqrt{n_s}$, where n_s is the

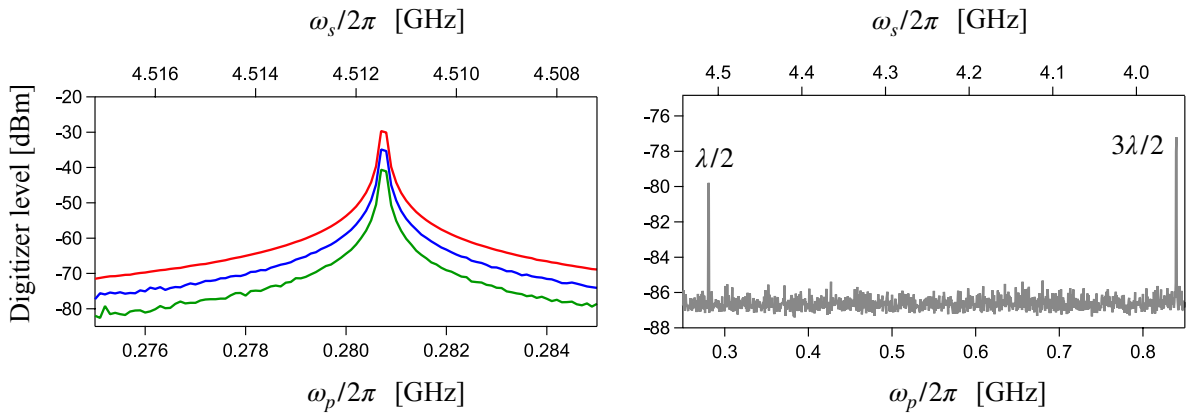

Figure 7.3: Readout of $\lambda/2$ resonator using parametric swap. (a) Two tone spectroscopy showing a weak probe tone ω_p (bottom axis) applied to the input of the $\lambda/2$ resonator and a strong parametric swap drive tone ω_s (top axis) applied to the input of the $\lambda/4$ resonator. The frequencies are chosen such that $\omega_s = \omega_{\lambda/4} - \omega_p$. Due to the nonlinear interaction between the resonators, when the probe photon is resonant with the $\lambda/2$ resonator, it absorb a swap photon and is upconverted to a high frequency photon in the $\lambda/4$ resonator. The plot shows this upconversion where the Y axis is the digitizer power level at $\omega_{\lambda/4}$. (b) Same measurement as above, but for a wider range of probe frequency. The SQUID is sensitive to the current antinode of the $\lambda/2$ resonator. Therefore, we observe the $\lambda/2$ and the $3\lambda/2$ modes of the resonator and not the λ mode. This also verfies the physical nature of the coupling between the two resonators.

number of drive photons. In the rotating frame of the swap drive, Eq. (7.1) suggests that the two resonators are coupled resonantly. Therefore, a low-frequency photon in the $\lambda/2$ resonator can be up-converted to the high-frequency $\lambda/4$ resonator by absorbing a drive photon. Similarly, a high frequency photon can be down-converted to a low frequency photon by emitting a drive photon. This forms the basis of our readout strategy for measuring $\omega_{\lambda/2}$.

The measurement involves sweeping a probe tone ω_p sent to the $\lambda/2$ resonator near its expected resonance frequency. The swap tone at ω_s is swept simultaneously at the input of the $\lambda/4$ resonator such that $\omega_s = \omega_{\lambda/4} - \omega_p$, where $\omega_{\lambda/4}/2\pi = 4.8$ GHz is set by the flux bias on the coil. The output of the $\lambda/4$ resonator is sent directly to an Aeroflex 3035C digitizer to monitor the power level of the received signal at $\omega_{\lambda/4}$. Figure 7.3(a) shows the power level of the digitizer as the two tones are swept. When $\omega_p = \omega_{\lambda/2}$, the swap

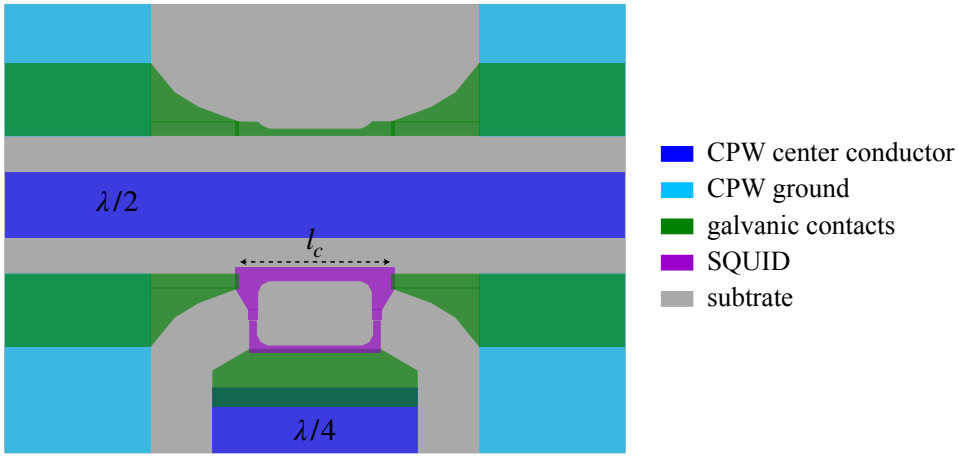

Figure 7.4: CAD layout of the SQUID design for parametric coupling.

tone ω_s mediates frequency conversion resulting in a strong up-conversion of photons at $\omega_{\lambda/4}$ which appears as a peak in the measured power of the resonator. We show this for a varying probe power (in steps of 5 dBm) but keeping the swap power constant. For the measurement shown in Fig. 7.3(a), we use strong excitation powers for both the drives to obtain a good signal to noise ratio. Using this method, we measure $\omega_{\lambda/2}/2\pi = 280.7$ MHz. After converting the digitizer power level from dBm to V, we extract a full width at half maximum (FWHM) of 131 kHz from a Lorentzian fit to the amplitude data (not shown here).

Another check that was performed to validate the measurement was to measure the SQUID's sensitivity to higher modes of the $\lambda/2$ resonator. As the SQUID is galvanically connected to ground at the current anti-node of the $\lambda/2$ resonator, it is sensitive to n$\lambda/2$ modes of this resonator, where n is an odd integer. Repeating the same measurement over a wide band, Fig. 7.3(b) captures the SQUID's sensitivity to the odd modes while being insensitive to the even mode λ. The choice of the powers for the two tones for this measurement was significantly lower than the one shown in Fig. 7.3(a).

7.4 Effect of flux bias on coupling strength

To understand the mechanism of parametric coupling, consider the Fig. 7.4, which shows the CAD layout of the SQUID and its physical connections to the two resonators as in

the measured device. The coupling arm of the SQUID of length l_c shares the microwave ground of the $\lambda/2$ resonator. As a result, the current flowing in the $\lambda/2$ resonator generates a dynamic flux $\Delta\Phi = L_{\rm tot} I_{\rm rms}$ which couples to the SQUID thereby causing a small change in $\omega_{\lambda/4}$. Here, $L_{\rm tot}$ is the total inductance of the SQUID's coupling arm, which is a combination of the geometric and kinetic inductance and $I_{\rm rms}$ is the root-mean-square of the current in the $\lambda/2$ resonator. The total flux that the SQUID is now sensitive to is $\Phi_{\rm tot} = \Phi + \Delta\Phi$, where Φ is the static flux from the coil. To measure an observable frequency change in $\omega_{\lambda/4}$ due to $\Delta\Phi$, the resonator needs to be biased at a point where $\partial\omega_{\lambda/4}/\partial\Phi$ is large. By differentiating the theoretical tuning curve from Fig. 7.1(a) with respect to Φ/Φ_0, we can calculate the expected flux sensitivity for the $\lambda/4$ resonator in the measured device. We plot this in Fig. 7.5(a). By biasing the SQUID further down the tuning curve, we can enhance the coupling strength.

As discussed in Chapter 2, the single-photon coupling strength between the two resonators, $g_0 = (\partial\omega_{\lambda/4}/\partial\Phi)\Delta\Phi_{\rm zpf}$, where $\Delta\Phi_{\rm zpf}$ is the flux due to the zero-point-fluctuations of the current in the $\lambda/2$ resonator. For this device, we estimate $g_0/2\pi = 82$ kHz at $\omega_{\lambda/4}/2\pi = 4$ GHz, where $\partial\omega/\partial\Phi = (2\pi)10$ GHz/Φ_0. We use $L_{\rm tot} = L_0 l_c = 10$ pH, where L_0 is the geometric inductance/length of the $\lambda/2$ resonator. The value of $L_{\rm tot}$ can be increased by many orders of magnitude by engineering the kinetic inductance of the coupling arm. An alternative way to enhance the coupling strength is by using a strong swap drive as discussed earlier. The modified coupling strength $g = g_0\sqrt{n_s}$ depends on the number of swap drive photons. The parametric coupling we see in the measurements is due to g.

The effect of g on the $\lambda/4$ resonator bias frequency is shown in Fig. 7.5(b). We perform the same measurement discussed before to read out the $\lambda/2$ resonator using a swap drive for different flux bias conditions. As we go down the bias curve, we see a stronger signal amplitude at the digitizer from the up-converted photons in the resonator. We plot the maximum amplitude as a function of the flux bias corresponding to the measured resonance frequency in Fig. 7.5(c). We see a qualitative agreement of the profile with that of Fig. 7.5(a).

7.5 Chapter conclusions

Our results demonstrate the essential elements required for exploring the ideas of a quantum heat engine discussed in Chapter 2. We present a large bandwidth, frequency-tunable $\lambda/4$ resonator parametrically coupled to a high quality factor $\lambda/2$ resonator. The nature of this parametric coupling allowed us to measure $\omega_{\lambda 2}$ using the $\lambda/4$ resonator by employing a swap drive. To prevent the higher harmonic modes of the $\lambda/2$ resonator from interacting

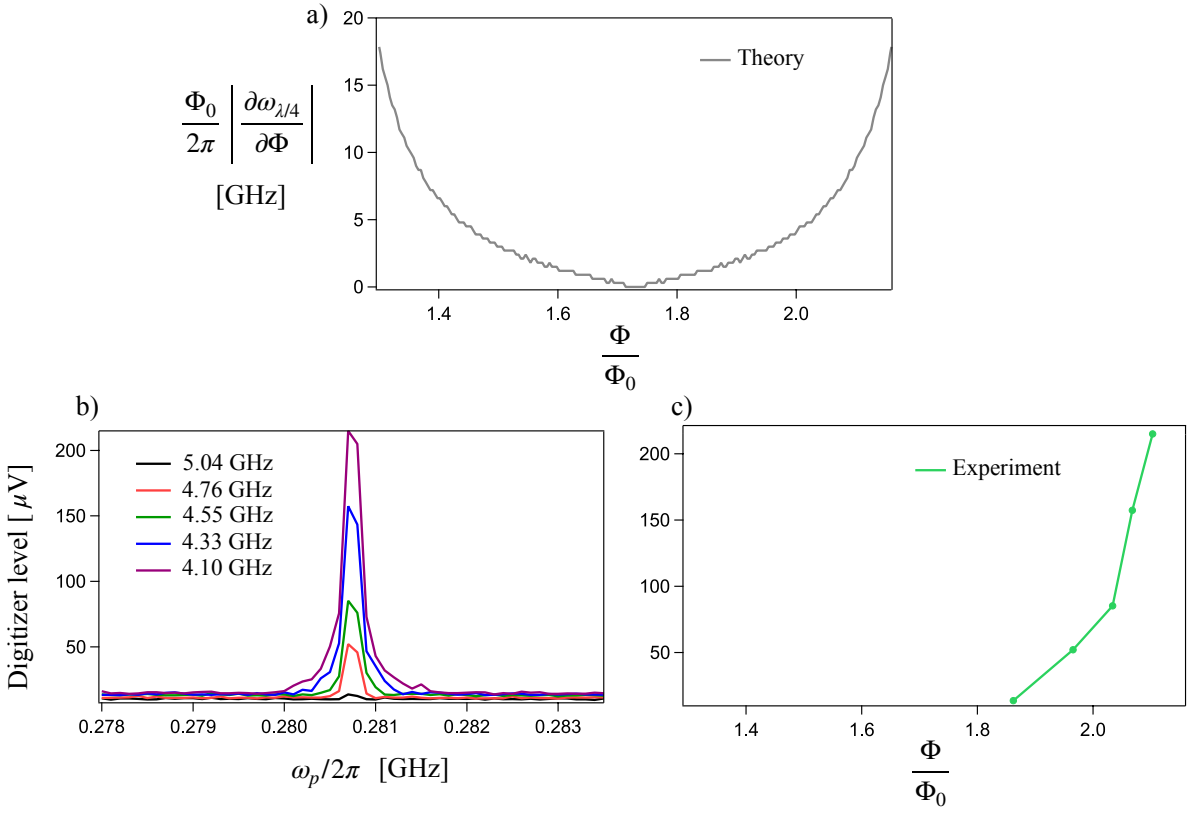

Figure 7.5: Effect of flux bias on coupling strength. (a) Theoretical flux sensitivity, $\partial\omega_{\lambda/4}/\partial\Phi$, in units of GHz/$\Phi_0$ as a function of normalized external flux, calculated using Eq. (2.34) for the experimental tuning curve in shown in Fig. 7.1. We achieve high single photon coupling strength when working near flux bias points where the slope is large. (b) We use the swap drive technique to readout out the $\lambda/2$ resonator. The Y-axis shows the digitizer amplitude level at $\omega_{\lambda/4}/2\pi$. The curves are for different $\omega_{\lambda/4}/2\pi$ obtained by changing Φ/Φ_0. For a fixed swap photon and probe photon powers, we see that by biasing the $\lambda/4$ resonator at different frequencies along the tuning curve, the coupling strength increases, evident from the higher digitizer amplitude levels from the upconverted photons in the $\lambda/4$ resonator. (c) The maximum digitizer power level from (b) is plotted against the corresponding flux bias operating points. We observe a similar qualitative trend in the coupling strength as expected from theory, shown in (a).

with the other resonator, we implemented a novel stepped impedance based band stop filter as an intrinsic feature. We also show that the coupling strength can be enhanced by flux biasing the SQUID. The large bandwidth of the $\lambda/4$ resonator made it difficult to directly quantify g in our device. By using a suitable low frequency amplifier to measure the $\lambda/2$ resonator directly, signatures of resonant interaction such as an avoided level crossing due would be easier to observe which would help in directly quantifying g. Future device designs can improve g_0 by enhancing the kinetic inductance of the coupling arm of the SQUID. By using suitable time-domain pulsing techniques, the action of the heat engine can be studied.

Chapter 8

Conclusions

8.1 Summary

This thesis is a result of work that studies: a) giant artificial atoms, formed from a transmon qubit, in superconducting waveguide-QED architecture and b) parametrically-coupled superconducting resonators which implements an optomechanical-like interaction. At the heart of these devices is a SQUID, formed using Josephson junctions, which provides the essential nonlinearity to explore the rich physics that describes these devices.

We developed a theoretical framework based on existing original results, which implements the necessary interaction in our devices. We then derived the necessary equations from microwave transmission-line theory to help us model their behavior and numerically calculate the response. We used a classical model to study the scattering of a artificial atom coupled to a transmission line. We then discussed a theoretical proposal to build a heat engine using the coupled resonator system, where the dynamics is simulated using classical Langevin equations. The framework that we developed, provided valuable input to the design methodology for implementing the devices under study.

Building on the theoretical models, we designed the chip layouts using circuit and electromagnetic simulations on commercially available simulation packages. In depth simulations were performed, involving design variations, to feedback on the measured results and to explain observed experimental signatures and features that deviated from theoretical predictions. During this process, several observations were made, which provides valuable input for designing future devices. The finalized layouts were then translated to physical devices using micro/nano fabrication techniques. Proceeding to their characterization, low

temperature measurements presents several challenges which are discussed in the context of our measurement setup. Steps taken to improve the general microwave health of our setup is also discussed. The importance of shielding and thermal management is impressed upon.

An artificial atom coupled to 1D vacuum is one of the most basic prototype systems in superconducting-waveguide QED. We have added another important addition to the existing waveguide-QED toolbox, a giant artificial atom. Due to its multipoint coupling nature, the qubit's absorption/emission amplitudes interfere, resulting is a strong frequency-dependent coupling rates of its multiple transition levels, which is clearly demonstrated by our results. We observed large on/off ratios, as high as 380, for the $|0\rangle - |1\rangle$ transition. The giant transmon also has higher transition levels. We show that we can tune the coupling rate of the $|1\rangle - |2\rangle$ transition relative to the $|0\rangle - |1\rangle$ transition by a factor greater than 200. To our knowledge, these numbers are a record high for a superconducting waveguide-QED setup. The relative modulation of the coupling rates allowed us to engineer the giant transmon as a lambda system with a metastable state, one of the most commonly studied three-level systems in quantum optics. To validate this, we demonstrate electromagnetically-induced transparency (EIT), a typical signature for a lambda system. Unlike other EIT demonstrations using superconducting circuits, we achieved this in a cavity-free setup. Our claim to observing EIT is confirmed by a master equation solution, with excellent agreement between theory and experiment.

We also studied a device with two giant artificial atoms, connected in a braided configuration. The nature of braided topology allows an existence of a special frequency point where the qubits are theoretically shown to interact in a decoherence-free environment. Although, we were not able to operate the qubits at this special frequency bias point, we observed interesting resonant behavior of the qubits at two other frequency bias points, one closer to the special point and one away. Near these frequency points, when the qubits are resonant and off-resonant, we also observed multiple resonances when probing for Autler-Townes splitting (ATS), which is surprising as the qubits are nominally identical. We believe our experimental signatures could be an indication of novel physics, which is currently being understood theoretically.

The quest for a quantum heat engine to test the ideas of quantum thermodynamics is an ongoing one. The problem is being tackled using different implementations. The "photonic piston" engine we propose to build, is a system with two coupled-superconducting resonators. The nonlinear interaction between the resonators, mediated by a SQUID, couples the current in one resonator to the photon number in the other, thus implementing an optomechanical-like interaction. Upon suitably driving the system with noise, a limit cycle is established, which results in the build up of a coherence in the system. We fabricated

such a device in a regime that is suitable for its operation. We demonstrated the crucial nonlinear coupling which is essential to its working as a heat engine. We also showed that we can modulate the coupling between the resonators depending on the flux biasing condition of the SQUID.

8.2 Future work

As suggested in Chapter 3, the use of airbridges in experiments involving giant transmons is crucial, as was implemented by a competing group [73]. They help in producing a cleaner microwave environment, suppressing the spurious modes that could be a result of slotline mode propagation, especially when the transmission line involves extreme meandering. In general, care should also be taken while positioning the SQUID. From our simulations of the braided giant transmons, we observe that stray coupling of the SQUID to ground currents can result in behavior which deviates from theory. Incorporating dedicated readout resonators for the giant transmons provides an alternative way to characterize the qubits [73]. In this case, the transmission line can be terminated by 50 Ω ports which prevent unwanted reflections at the plane of the connectors on the sample box. This also ensures that the qubits are coupled a strict 50 Ω environment [73].

To demonstrate a heat engine with our coupled-resonator device, it is important to quantify the actual coupling strength that can be obtained. The SQUID-terminated $\lambda/4$ resonator, which is also our readout resonator, is strongly overcoupled and hence quantifying the coupling strength between the resonators is challenging. The fundamental frequency of the $\lambda/2$ resonator is outside the measurement band making it difficult to directly measure it. Having a dedicated low frequency cryogenic amplifier to measure the frequency directly is useful. The coupling strength in this case can be directly observed by probing the $\lambda/2$ resonator as it's linewidth is smaller or comparable to the expected coupling strength. For the engine to operate, the single photon coupling strength should be quite high. This can be achieved by fabricating a device with a thin meandering coupling arm, as discussed in Chapter 2. The kinetic inductance of the arm can be used to boost the coupling strength further. Once this is achieved, careful calibration of noise drives at room temperature is required to drive the system for showing the Otto-cycle operation.

References

[1] R J Thompson, G Rempe, and H J Kimble. Observation of normal-mode splitting for an atom in an optical cavity. *Physical Review Letters*, 68(8):1132–1135, February 1992.

[2] A Boca, R Miller, K M Birnbaum, A D Boozer, J McKeever, and H J Kimble. Observation of the Vacuum Rabi Spectrum for One Trapped Atom. *Physical Review Letters*, 93(23):233603, December 2004.

[3] J M Raimond, M Brune, and S Haroche. Manipulating quantum entanglement with atoms and photons in a cavity. *Reviews of Modern Physics*, 73(3):565–582, August 2001.

[4] P Hyafil, J Mozley, A Perrin, J Tailleur, G Nogues, M Brune, J M Raimond, and S Haroche. Coherence-Preserving Trap Architecture for Long-Term Control of Giant Ryberg Atoms. *Physical Review Letters*, 93(10):103001, September 2004.

[5] I Chiorescu, P Bertet, K Semba, Y Nakamura, C J P M Harmans, and J E Mooij. Coherent dynamics of a flux qubit coupled to a harmonic oscillator. *Nature*, 431(7005):159–162, September 2004.

[6] A Wallraff, D I Schuster, A Blais, L Frunzio, R S Huang, J Majer, S Kumar, S M Girvin, and R J Schoelkopf. Strong coupling of a single photon to a superconducting qubit using circuit quantum electrodynamics. *Nature*, 431(7005):162–167, September 2004.

[7] P Forn-Díaz, J J García-Ripoll, B Peropadre, J L Orgiazzi, M A Yurtalan, R Belyansky, C M Wilson, and A Lupascu. Ultrastrong coupling of a single artificial atom to an electromagnetic continuum in the nonperturbative regime. *Nature Physics*, 13(1):39–43, October 2016.

[8] Fumiki Yoshihara, Tomoko Fuse, Sahel Ashhab, Kosuke Kakuyanagi, Shiro Saito, and Kouichi Semba. Superconducting qubit–oscillator circuit beyond the ultrastrong-coupling regime. *Nature Physics*, 13(1):44–47, January 2017.

[9] Xiu Gu, Anton Frisk Kockum, Adam Miranowicz, Yu-xi Liu, and Franco Nori. Microwave photonics with superconducting quantum circuits. *Physics Reports*, 718-719:1–102, November 2017.

[10] Anton Frisk Kockum, Adam Miranowicz, Simone De Liberato, Salvatore Savasta, and Franco Nori. Ultrastrong coupling between light and matter. *Nature Reviews Physics*, 1(1):19–40, January 2019.

[11] E T Jaynes and F W Cummings. Comparison of quantum and semiclassical radiation theories with application to the beam maser. *Proceedings of the IEEE*, 51(1):89–109, January 1963.

[12] Dibyendu Roy, C M Wilson, and Ofer Firstenberg. ¡i¿Colloquium¡/i¿: Strongly interacting photons in one-dimensional continuum. *Reviews of Modern Physics*, 89(2):021001, May 2017.

[13] O Astafiev, A M Zagoskin, A A Abdumalikov, Yu A Pashkin, T Yamamoto, K Inomata, Y Nakamura, and J S Tsai. Resonance Fluorescence of a Single Artificial Atom. *Science*, 327(5967):840–843, February 2010.

[14] Io-Chun Hoi, C M Wilson, Göran Johansson, Joel Lindkvist, Borja Peropadre, Tauno Palomaki, and Per Delsing. Microwave quantum optics with an artificial atom in one-dimensional open space. *New Journal of Physics*, 15(2):025011, February 2013.

[15] Sankar R Sathyamoorthy, L Tornberg, Anton F Kockum, Ben Q Baragiola, Joshua Combes, C M Wilson, Thomas M Stace, and G Johansson. Quantum Nondemolition Detection of a Propagating Microwave Photon. *Physical Review Letters*, 112(9):093601, March 2014.

[16] Io-Chun Hoi, Anton F Kockum, Tauno Palomaki, Thomas M Stace, Bixuan Fan, Lars Tornberg, Sankar R Sathyamoorthy, Göran Johansson, Per Delsing, and C M Wilson. Giant Cross–Kerr Effect for Propagating Microwaves Induced by an Artificial Atom. *Physical Review Letters*, 111(5):053601, August 2013.

[17] Io-Chun Hoi, Tauno Palomaki, Joel Lindkvist, Göran Johansson, Per Delsing, and C M Wilson. Generation of Nonclassical Microwave States Using an Artificial Atom in 1D Open Space. *Physical Review Letters*, 108(26):263601, June 2012.

[18] C M Wilson, G Johansson, A Pourkabirian, M Simoen, J R Johansson, T Duty, F Nori, and P Delsing. Observation of the dynamical Casimir effect in a superconducting circuit. *Nature*, 479(7373):376–379, November 2011.

[19] Io-Chun Hoi, C M Wilson, Göran Johansson, Tauno Palomaki, Borja Peropadre, and Per Delsing. Demonstration of a Single-Photon Router in the Microwave Regime. *Physical Review Letters*, 107(7):073601, August 2011.

[20] P Forn-Díaz, C W Warren, C W S Chang, A M Vadiraj, and C M Wilson. On-Demand Microwave Generator of Shaped Single Photons. *Physical Review Applied*, 8(5):054015, November 2017.

[21] I C Hoi, A F Kockum, L Tornberg, A Pourkabirian, G Johansson, P Delsing, and C M Wilson. Probing the quantum vacuum with an artificial atom in front of a mirror. *Nature Physics*, 11(12):1045–1049, December 2015.

[22] Arjan F van Loo, Arkady Fedorov, Kevin Lalumière, Barry C Sanders, Alexandre Blais, and Andreas Wallraff. Photon-Mediated Interactions Between Distant Artificial Atoms. *Science*, 342(6165):1494–1496, December 2013.

[23] P Y Wen, K T Lin, A F Kockum, B Suri, H Ian, J C Chen, S Y Mao, C C Chiu, P Delsing, F Nori, G D Lin, and I C Hoi. Large Collective Lamb Shift of Two Distant Superconducting Artificial Atoms. *Physical Review Letters*, 123(23):233602, December 2019.

[24] Gustav Andersson, Baladitya Suri, Lingzhen Guo, Thomas Aref, and Per Delsing. Non-exponential decay of a giant artificial atom. *Nature Physics*, 65:1–5, August 2019.

[25] Martin V Gustafsson, Thomas Aref, Anton Frisk Kockum, Maria K Ekström, Göran Johansson, and Per Delsing. Propagating phonons coupled to an artificial atom. *Science*, 346(6206):207–211, October 2014.

[26] Thomas Aref, Per Delsing, Maria K Ekström, Anton Frisk Kockum, Martin V Gustafsson, Göran Johansson, Peter J Leek, Einar Magnusson, and Riccardo Manenti. Quantum Acoustics with Surface Acoustic Waves. In *Superconducting Devices in Quantum Optics*, pages 217–244. Springer International Publishing, Cham, March 2016.

[27] Anton Frisk Kockum, Per Delsing, and Göran Johansson. Designing frequency-dependent relaxation rates and Lamb shifts for a giant artificial atom. *Physical Review A*, 90(1):1, July 2014.

[28] Anton Frisk Kockum, Göran Johansson, and Franco Nori. Decoherence-Free Interaction between Giant Atoms in Waveguide Quantum Electrodynamics. *Physical Review Letters*, 120(14):140404, April 2018.

[29] Anton Frisk Kockum. Quantum optics with giant atoms – the first five years. *arXiv e-prints*, page arXiv:1912.13012, December 2019.

[30] Andreas Ask, Maria Ekström, Per Delsing, and Göran Johansson. Cavity-free vacuum-Rabi splitting in circuit quantum acoustodynamics. *Physical Review A*, 99(1):013840, January 2019.

[31] Lingzhen Guo, Arne Grimsmo, Anton Frisk Kockum, Mikhail Pletyukhov, and Göran Johansson. Giant acoustic atom: A single quantum system with a deterministic time delay. *Physical Review A*, 95(5):053821, May 2017.

[32] Lingzhen Guo, Anton Frisk Kockum, Florian Marquardt, and Göran Johansson. Oscillating bound states for a giant atom. *arXiv e-prints*, page arXiv:1911.13028, November 2019.

[33] Shangjie Guo, Yidan Wang, Thomas Purdy, and Jacob Taylor. Beyond Spontaneous Emission: Giant Atom Bounded in Continuum. *arXiv e-prints*, page arXiv:1912.09980, December 2019.

[34] Jens Koch, Terri M Yu, Jay Gambetta, A A Houck, D I Schuster, J Majer, Alexandre Blais, M H Devoret, S M Girvin, and R J Schoelkopf. Charge-insensitive qubit design derived from the Cooper pair box. *Physical Review A*, 76(4):042319, October 2007.

[35] Jeremy L O'Brien, Akira Furusawa, and Jelena Vučković. Photonic quantum technologies. *Nature Photonics*, 3(12):687–695, December 2009.

[36] Lucas Lamata, Adrian Parra-Rodriguez, Mikel Sanz, and Enrique Solano. Digital-analog quantum simulations with superconducting circuits. *Advances in Physics: X*, 3(1):1457981, April 2018.

[37] Richard P Feynman. There's Plenty of Room at the Bottom. February 1960.

[38] H E D Scovil and E O Schulz-DuBois. Three-Level Masers as Heat Engines. *Physical Review Letters*, 2(6):262–263, March 1959.

[39] Marlan O Scully. Extracting Work from a Single Thermal Bath via Quantum Negentropy. *Physical Review Letters*, 87(22):220601–4, November 2001.

[40] Marlan O Scully. Quantum Afterburner: Improving the Efficiency of an Ideal Heat Engine. *Physical Review Letters*, 88(5):050602–4, January 2002.

[41] M O Scully. Extracting Work from a Single Heat Bath via Vanishing Quantum Coherence. *Science*, 299(5608):862–864, January 2003.

[42] Marlan O Scully. Quantum Photocell: Using Quantum Coherence to Reduce Radiative Recombination and Increase Efficiency. *Physical Review Letters*, 104(20):207701–4, May 2010.

[43] Tien D Kieu. The Second Law, Maxwell's Demon, and Work Derivable from Quantum Heat Engines. *Physical Review Letters*, 93(14):140403, September 2004.

[44] T D Kieu. Quantum heat engines, the second law and Maxwell's daemon. *The European Physical Journal D*, 39(1):115–128, July 2006.

[45] Jukka P Pekola. Towards quantum thermodynamics in electronic circuits. *Nature Physics*, 11(2):118–123, February 2015.

[46] H T Quan, P Zhang, and C P Sun. Quantum-classical transition of photon-Carnot engine induced by quantum decoherence. *Physical Review E*, 73(3):036122–6, March 2006.

[47] O Abah, J Roßnagel, G Jacob, S Deffner, F Schmidt-Kaler, K Singer, and E Lutz. Single-Ion Heat Engine at Maximum Power. *Physical Review Letters*, 109(20):203006–6, November 2012.

[48] J Roßnagel, O Abah, F Schmidt-Kaler, K Singer, and E Lutz. Nanoscale Heat Engine Beyond the Carnot Limit. *Physical Review Letters*, 112(3):030602–5, January 2014.

[49] P G Steeneken, K Le Phan, M J Goossens, G E J Koops, G J A M Brom, C van der Avoort, and J T M van Beek. Piezoresistive heat engine and refrigerator. *Nature Physics*, 7(4):354–359, January 2011.

[50] S Whalen, M Thompson, D Bahr, C Richards, and R Richards. Design, fabrication and testing of the P3 micro heat engine. *Sensors and Actuators A: Physical*, 104(3):290–298, May 2003.

[51] Johannes Roßnagel, Samuel T Dawkins, Karl N Tolazzi, Obinna Abah, Eric Lutz, Ferdinand Schmidt-Kaler, and Kilian Singer. A single-atom heat engine. *Science*, 352(6283):325–329, April 2016.

[52] J R Johansson, G Johansson, and Franco Nori. Optomechanical-like coupling between superconducting resonators. *Physical Review A*, 90(5):053833–10, November 2014.

[53] Ali Ü C Hardal, Nur Aslan, C M Wilson, and Özgür E Müstecaplıoğlu. Quantum heat engine with coupled superconducting resonators. *Physical Review E*, 96(6):062120, December 2017.

[54] H Kamerlingh Onnes. The superconductivity of mercury. *Comm. Phys. Lab. Univ. Leiden*, 122:122–124, 1911.

[55] J Bardeen, L N Cooper, and J R Schrieffer. Microscopic Theory of Superconductivity. *Physical Review*, 106(1):162–164, April 1957.

[56] J Bardeen, L N Cooper, and J R Schrieffer. Theory of Superconductivity. *Physical Review*, 108(5):1175–1204, December 1957.

[57] V L Ginzburg. On the theory of superconductivity. *Il Nuovo Cimento (1955-1965)*, 2(6):1234–1250, 1955.

[58] W Meissner and R Ochsenfeld. Ein neuer Effekt bei Eintritt der Supraleitfähigkeit. *Die Naturwissenschaften*, 21(44):787–788, November 1933.

[59] B D Josephson. Possible new effects in superconductive tunnelling. *Physics Letters*, 1(7):251–253, July 1962.

[60] R C Jaklevic, John Lambe, A H Silver, and J E Mercereau. Quantum Interference Effects in Josephson Tunneling. *Physical Review Letters*, 12(7):159–160, February 1964.

[61] Theodore Van Duzer and Charles William Turner. *Principles of Superconductive Devices and Circuits*. Prentice Hall, 1999. Google-Books-ID: uoViQgAACAAJ.

[62] Vinay Ambegaokar and Alexis Baratoff. Tunneling Between Superconductors. *Physical Review Letters*, 10(11):486–489, June 1963.

[63] Y Nakamura, Yu A Pashkin, and J S Tsai. Coherent control of macroscopic quantum states in a single-Cooper-pair box. *Nature*, 398(6730):786–788, April 1999.

[64] V Bouchiat, D Vion, P Joyez, D Esteve, and M H Devoret. Quantum coherence with a single Cooper pair. *Physica Scripta*, 1998(T76):165, 1998.

[65] Audrey Cottet. *Implementation of a quantum bit in a superconducting circuit*. PhD thesis, 2002.

[66] David M Pozar. Microwave Engineering. pages 1–756, October 2011.

[67] Rainee N Simons. Coplanar Waveguide Circuits, Components, and Systems. pages 1–459, December 2010.

[68] B Chiaro, A Megrant, A Dunsworth, Z Chen, R Barends, B Campbell, Y Chen, A Fowler, I C Hoi, E Jeffrey, J Kelly, J Mutus, C Neill, P J J O'Malley, C Quintana, P Roushan, D Sank, A Vainsencher, J Wenner, T C White, and John M Martinis. Dielectric surface loss in superconducting resonators with flux-trapping holes. *Superconductor Science and Technology*, 29(10):104006, October 2016.

[69] Jan Goetz, Frank Deppe, Max Haeberlein, Friedrich Wulschner, Christoph W Zollitsch, Sebastian Meier, Michael Fischer, Peter Eder, Edwar Xie, Kirill G Fedorov, Edwin P Menzel, Achim Marx, and Rudolf Gross. Loss mechanisms in superconducting thin film microwave resonators. *Journal of Applied Physics*, 119(1):015304, January 2016.

[70] A Megrant, C Neill, R Barends, B Chiaro, Yu Chen, L Feigl, J Kelly, Erik Lucero, Matteo Mariantoni, P J J O'Malley, D Sank, A Vainsencher, J Wenner, T C White, Y Yin, J Zhao, C J Palmstrøm, John M Martinis, and A N Cleland. Planar superconducting resonators with internal quality factors above one million. *Applied Physics Letters*, 100(11):113510, 2012.

[71] Io Chun Hoi. *Quantum Optics with Propagating Microwaves in Superconducting Circuits*. PhD thesis, Chalmers University of Technology, 2013. ISBN: 9789173858786.

[72] H Wang, M Hofheinz, M Ansmann, R C Bialczak, E Lucero, M Neeley, A D O'Connell, D Sank, J Wenner, A N Cleland, and John M Martinis. Measurement of the Decay of Fock States in a Superconducting Quantum Circuit. *Physical Review Letters*, 101(24):240401, December 2008.

[73] Bharath Kannan, Max Ruckriegel, Daniel Campbell, Anton Frisk Kockum, Jochen Braumüller, David Kim, Morten Kjaergaard, Philip Krantz, Alexander Melville, Bethany M. Niedzielski, Antti Vepsäläinen, Roni Winik, Jonilyn Yoder, Franco Nori, Terry P. Orland o, Simon Gustavsson, and William D. Oliver. Waveguide Quantum

Electrodynamics with Giant Superconducting Artificial Atoms. *arXiv e-prints*, page arXiv:1912.12233, December 2019.

[74] Markus Aspelmeyer, Tobias J Kippenberg, and Florian Marquardt. Cavity optomechanics. *Reviews of Modern Physics*, 86(4):1391–1452, December 2014.

[75] Michael A. Boles and Yunus A. Cengel Dr. *Thermodynamics: An Engineering Approach*. McGraw-Hill Education, January 2014. Google-Books-ID: Ao95ngEACAAJ.

[76] J M Fink, L Steffen, P Studer, Lev S Bishop, M Baur, R Bianchetti, D Bozyigit, C Lang, S Filipp, P J Leek, and A Wallraff. Quantum-To-Classical Transition in Cavity Quantum Electrodynamics. *Physical Review Letters*, 105(16):163601, October 2010.

[77] Simon E Nigg, Hanhee Paik, Brian Vlastakis, Gerhard Kirchmair, S Shankar, Luigi Frunzio, M H Devoret, R J Schoelkopf, and S M Girvin. Black-Box Superconducting Circuit Quantization. *Physical Review Letters*, 108(24):260, June 2012.

[78] G E Ponchak, J Papapolymerou, and M M Tentzeris. Excitation of coupled slotline mode in finite-ground CPW with unequal ground-plane widths. *IEEE Transactions on Microwave Theory and Techniques*, 53(2):713–717.

[79] Sotiris Alexandrou, Roman Sobolewski, and Thomas Y Hsiang. Bend-induced even and odd modes in picosecond electrical transients propagated on a coplanar waveguide. *Applied Physics Letters*, 60(15):1836–1838, June 1998.

[80] Chung-Yi Lee, Yaozhong Liu, and Tatsuo Itoh. The effects of the coupled slotline mode and air-bridges on CPW and NLC waveguide discontinuities. *IEEE Transactions on Microwave Theory and Techniques*, 43(12):2759–2765, 1995.

[81] Zijun Chen, A Megrant, J Kelly, R Barends, J Bochmann, Yu Chen, B Chiaro, A Dunsworth, E Jeffrey, J Y Mutus, P J J O'Malley, C Neill, P Roushan, D Sank, A Vainsencher, J Wenner, T C White, A N Cleland, and John M Martinis. Fabrication and characterization of aluminum airbridges for superconducting microwave circuits. *Applied Physics Letters*, 104(5):052602, February 2014.

[82] G J Dolan. Offset masks for lift-off photoprocessing. *Applied Physics Letters*, 31(5):337–339, September 1977.

[83] Jay M Gambetta, Conal E Murray, Y K K Fung, Douglas T McClure, Oliver Dial, William Shanks, Jeffrey W Sleight, and Matthias Steffen. Investigating Surface Loss

Effects in Superconducting Transmon Qubits. *IEEE Transactions on Applied Superconductivity*, 27(1):1–5.

[84] Oliver Dial, Douglas T McClure, Stefano Poletto, G A Keefe, Mary Beth Rothwell, Jay M Gambetta, David W Abraham, Jerry M Chow, and Matthias Steffen. Bulk and surface loss in superconducting transmon qubits. *Superconductor Science and Technology*, 29(4):044001, March 2016.

[85] B Selikson and T A Longo. A study of purple plague and its role in integrated circuits. *Proceedings of the IEEE*, 52(12):1638–1641.

[86] L J Zeng, S Nik, T Greibe, P Krantz, C M Wilson, P Delsing, and E Olsson. Direct observation of the thickness distribution of ultra thin AlO x barriers in Al/AlO x /Al Josephson junctions. *Journal of Physics D: Applied Physics*, 48(39):395308, October 2015.

[87] Lukas Grünhaupt, Nataliya Maleeva, Sebastian T Skacel, Martino Calvo, Florence Levy-Bertrand, Alexey V Ustinov, Hannes Rotzinger, Alessandro Monfardini, Gianluigi Catelani, and Ioan M Pop. Loss Mechanisms and Quasiparticle Dynamics in Superconducting Microwave Resonators Made of Thin-Film Granular Aluminum. *Physical Review Letters*, 121(11):117001, September 2018.

[88] Mehran Vahdani Moghaddam, C W Sandbo Chang, Ibrahim Nsanzineza, A M Vadiraj, and C M Wilson. Carbon nanotube-based lossy transmission line filter for superconducting qubit measurements. *Applied Physics Letters*, 115(21):213504, November 2019.

[89] Bo Lv, Rujiang Li, Jiahui Fu, Qun Wu, Kuang Zhang, Wan Chen, Zhefei Wang, and Ruyu Ma. Analysis and modeling of Fano resonances using equivalent circuit elements. *Scientific Reports*, 6(1):1–6, August 2016.

[90] Michael J Peterer, Samuel J Bader, Xiaoyue Jin, Fei Yan, Archana Kamal, Theodore J Gudmundsen, Peter J Leek, Terry P Orlando, William D Oliver, and Simon Gustavsson. Coherence and Decay of Higher Energy Levels of a Superconducting Transmon Qubit. *Physical Review Letters*, 114(1):010501, January 2015.

[91] B R Mollow. Power Spectrum of Light Scattered by Two-Level Systems. *Physical Review*, 188(5):1969–1975, December 1969.

[92] S H Autler and C H Townes. Stark Effect in Rapidly Varying Fields. *Physical Review*, 100(2):703–722, October 1955.

[93] M Baur, S Filipp, R Bianchetti, J M Fink, M Göppl, L Steffen, P J Leek, A Blais, and A Wallraff. Measurement of Autler-Townes and Mollow Transitions in a Strongly Driven Superconducting Qubit. *Physical Review Letters*, 102(24):243602, June 2009.

[94] Mika A Sillanpää, Jian Li, Katarina Cicak, Fabio Altomare, Jae I Park, Raymond W Simmonds, G S Paraoanu, and Pertti J Hakonen. Autler-Townes Effect in a Superconducting Three-Level System. *Physical Review Letters*, 103(19):193601, November 2009.

[95] G Wendin and V S Shumeiko. Quantum bits with Josephson junctions (Review Article). *Low Temperature Physics*, 33(9):724–744, September 2007.

[96] M Naghiloo, M Abbasi, Yogesh N Joglekar, and K W Murch. Quantum state tomography across the exceptional point in a single dissipative qubit. *Nature Physics*, 15(12):1232–1236, December 2019.

[97] Michael Fleischhauer, Atac Imamoglu, and Jonathan P Marangos. Electromagnetically induced transparency: Optics in coherent media. *Reviews of Modern Physics*, 77(2):633–673, July 2005.

[98] Petr M Anisimov, Jonathan P Dowling, and Barry C Sanders. Objectively Discerning Autler-Townes Splitting from Electromagnetically Induced Transparency. *Physical Review Letters*, 107(16):163604, October 2011.

[99] G Lindblad. On the generators of quantum dynamical semigroups. *Communications in Mathematical Physics*, 48(2):119–130, June 1976.

[100] Tony Y Abi-Salloum. Electromagnetically induced transparency and Autler-Townes splitting: Two similar but distinct phenomena in two categories of three-level atomic systems. *Physical Review A*, 81(5):053836, May 2010.

[101] Kenneth P. Burnham and David R. Anderson. *Model Selection and Multimodel Inference: A Practical Information-Theoretic Approach*. Springer-Verlag, New York, 2 edition, 2002.

[102] Mohammad Mirhosseini, Eunjong Kim, Xueyue Zhang, Alp Sipahigil, Paul B Dieterle, Andrew J Keller, Ana Asenjo-Garcia, Darrick E Chang, and Oskar Painter. Cavity quantum electrodynamics with atom-like mirrors. *Nature*, 569(7758):692–697, May 2019.

APPENDICES

Appendix A

Fabrication recipes

A.1 Giant transmon

1. Bare subtrate cleaning:
    - Piranha acid clean:
        - Prepare, 600 ml of H_2SO_4 + 150 ml of H_2O_2.
        - Clean for 15 min.
    - HF acid clean
        - Prepare 960 ml of DI water + 40 ml of HF (49%). The combination is 1 part of HF (49%) in 24 parts of DI water, so that you end up with a 2% HF solution.
        - Clean for 90 s. To check if the oxide is removed, the surface should be hydrophobic. After this, sequentially transfer the substrate to a set of beakers with DI water to remove any traces of HF.
2. Metal depostion: Al
    - Load the wafer immediately into the Plassys loadlock after HF clean. Pump overnight
    - Deposit 80 nm, with 5 rpm planary rotation.
3. Marker lithography:

- Resist spin coating:
  - Spin: S1811:
    - Step 1: 500 rpm, 100 rpm/s, 5 s
    - Step 2: 5000 rpm, 500 rpm/s, 60 s
  - Bake: at 120^0 C for 90 s
- Optical lithography:
  - Using MaskLess Aligner,
    - Laser: 405 nm
    - Dose: 130 mJ/cmˆ2
    - Defocus: 2
- Development: 2 min in MF319 solution, followed by DI water for 30 s.

4. Descumm:
   - Procedure: Load wafers in the YES ASH tool and run recipe 6 – 2 times
   - Recipe 6: 50 W, 120 s, 25^0 C
5. Si RIE:
   - Load cleaning wafer
   - Run recipe "OPT O_2/SF_6 clean" for 15 min
   - Load wafer
   - Run recipe "OPT Bosch¿2μm" with loop count step=9
   - Load cleaning wafer
   - Run recipe "OPT O_2/SF_6 clean" for 15 min
6. Solvent cleaning:
   - Clean wafers in a bath of hot PG Remover (1 hr) followed by a cold PG remover (5 min), IPA (10 min) and DI water (10 min). Transfer to quick dump rinse (QDR).
7. Substrate bake: at 110^0 C for 2 min.
8. Descumm
   - Procedure: Load wafers in the YES ASH tool and run recipe 11 – 1 time

9. Al lithography
    - Resist spin coating:
        - Prebake: at 120^0 C for 90 s
        - Spin: S1811:
            * Step 1: 500 rpm, 100 rpm/s, 5 s
            * Step 2: 5000 rpm, 500 rpm/s, 60 s
        - Bake: at 120^0 C for 90 s
    - Optical lithography:
        - Using MaskLess Aligner,
            * Laser: 405 nm
            * Dose: 130 mJ/cmˆ2
            * Defocus: 2
            * Use rotation correction only
    - Development: 60 s in AZ developer (1:1), followed by DI water for 30 s. Blow dry.
10. Descumm:
    - Procedure: Load wafers in the YES ASH tool and run recipe 6 – 3 times
    - Recipe 6: 50 W, 120 s, 25^0 C
11. Aluminum RIE
    - Load cleaning wafer
    - Run recipe "OPT O_2/SF_6 clean" for 10 min
    - Load wafer
    - Run recipe "OPT Al ICP new". Modify this recipe with $N_2 = 50$ sccm.
    - Immediately put wafer in DI water for 10 min
12. Solvent cleaning
    - Clean wafer in cold PG Remover (overnight) followed by IPA (15 min) and DI water (10 min). Transfer to quick dump rinse (QDR).
13. Descumm

- Procedure: Load wafers in the YES ASH tool and run recipe 11 – 1 time

14. Dicing resist coating
    - Spin coating:
      - Spin SPR4.5:
        * Step1: 500 rpm, 100 rpm/s, 5 s
        * Step2: 3000 rpm, 500 rpm/s, 60 s
      - Bake: at 110^0 C for 90 s
15. Block clean
    - Acetone (5 min) + sonication (2 mins)
    - IPA (5 min) + sonication (2 mins)
    - DI water (2 min) + sonication (2 mins)
    - Blow dry
16. Block bake
    - Bake block at 170^0 C for 2 min.'
17. Descumm
    - Procedure: Load wafers in the YES ASH tool and run recipe 11 – 1 time
18. Ebeam lithography
    - Spin coating:
      - Bake: at 170^0 C for 2 min. Cool.
      - Spin MMA-MAA EL11:
        * Step 1: 500 rpm, 100 rpm/s, 5 s.
        * Step: 4000 rpm, 1000 rpm/s, 60 s. This gives ˜450 nm
      - Bake: at 170^0 C for 8 min. Cool.
      - Spin 1:2::Zep:Anisol:
        * Step 1: 500 rpm, 100 rpm/s, 5 s.
        * Step: 6000 rpm, 1000 rpm/s, 60 s. This gives ˜60 nm
      - Bake: at 170^0 C for 5 min. Cool.

- Ebeam writing:
  - JEOL:
    - @ 100 kV: I use the top loading holder (2B)
      - Dose: 350 uC/cmˆ2 with PEC. The PEC file is simulated in Beamer.
      - Shot pitch: 8 nm
      - Condition files: 2nA_AP60 (for the junction patterns) and 4nA_AP130 (for the capacitor electrode patterns)
- Development:
  - 1:2::Zep:Anisol: 2 min in N-Amyacetate (ZED-N50) and 30 s in IPA, blow dry
  - MMA-MAA EL11: 8 min in IPA:DI water::4:1 solution, i.e, 25 ml of IPA in 100 ml of DI water. 30 s in IPA, blow dry

19. Al deposition- junction fabrication

    - Procedure: Load the block into the Plassys loadlock. Pump the LL for 1.5 hours before loading it into the evaporation chamber.
    - Deposition angle: $\pm 18^{\circ}$
    - Ion milling: 1min at each angle
    - Deposition thickness: 40 nm + 60 nm
    - Oxidation parameters: 10Torr, 35 mins (static oxidation)

20. Liftoff of junctions

    - Hot PG Remover@ 70 deg (2-3 hrs) followed by cold PG remover (5 min), IPA (5 min) and DI water (5 min). Blow dry. I use a pipette to gently squish liquid to aid liftoff. Also, use pipette to suck the film residues. Sonicate for 1 min in both solvents.
    - Or one can use cold liftoff in PG Remover. Keep the sample overnight. I found that doing cold liftoff gives me the best results. The film releases better. Sonicate for 1 min in cold PG remover. Transfer to IPA (5 min) and DI water (5 min). Blow dry.

21. Dicing resist coating: same as before

22. Dice block

- Dice block into chips using the Disco Dicer tool. Make sure the blade is the right one for Silicon. ALso check the dimensions of the chip beforehand

23. Chip clean
    - Acetone (5 min) + sonication (2 mins)
    - IPA (5 min) + sonication (2 mins)
    - DI water (2 min) + sonication (2 mins)
    - Blow dry
24. Wire bonding
    - Use semi-automatic wire bonder to bond the chip to a PCB.

A.2 Coupled resonators

1. Bare subtrate cleaning
    - Piranha acid clean:
        - Prepare, 600 ml of H_2SO_4 + 150 ml of H_2O_2.
        - Clean for 15 min.
    - HF acid clean
        - Prepare 960 ml of DI water + 40 ml of HF (49%). The combination is 1 part of HF (49%) in 24 parts of DI water, so that you end up with a 2% HF solution.
        - Clean for 90 s. To check if the oxide is removed, the surface should be hydrophobic. After this, sequentially transfer the substrate to a set of beakers with DI water to remove any traces of HF.
2. HMDS depositon. Use the standard cleanroom recipe.
3. Marker Lithography
    - Resist spin coating:
        - Spin: PMGI SF7:
            * Step 1: 500 rpm, 100 rpm/s, 5 s

        * Step 2: 5000 rpm, 500 rpm/s, 60 s
    - Bake: at 150^0 C for 5 mins
    - Spin: S1811:
        * Step 1: 500 rpm, 100 rpm/s, 5 s
        * Step 2: 5000 rpm, 500 rpm/s, 60 s
    - Bake: at 120^0 C for 90 s
- Optical lithography:
    - Using Mask aligner: Vac contact, 4.2s exposure, 30um Alignment gap, 5 s for all vacuum parameters
    - Using MaskLess Aligner,
        * Dose: 130 mJ/cmˆ2
        * Defocus: 2
- Development: 47 s in MF319 solution, followed by DI water for 30 s.

4. Descumm

    - Procedure: Load wafers in the YES ASH tool and run recipe 6 – 6 times
    - Recipe 6: 50 W, 120 s, 25^0 C

5. Metal depositon: Ti/Au/Pd

    - Procedure: Load wafer in the INTLVAC evaporator. Make sure the crucibles are loaded with the right material. Pump overnight
        - Ti: 3 nm @ 0.5 A/s
        - Au: 80 nm @ 2 A/s
        - Pd: 5 nm @ 0.5 A/s

6. Liftoff

    - Cold PG remover overnight for atleast 12 hours. Alternatively, hot bath of PG remover at 70^0 C for atleast 3 hours. After liftoff, rinse with IPA for 60s and DI water for 30s.

7. Substrate cleaning with Ti/Au/Pd

    - RCA1 clean:
        - Prepare 750 ml of DI water + 150 ml of NH4OH. Heat solution to 70^0 C.

- Prepare 150 ml of H2O2. Add this to the above solution. Stop heating.
- Clean subtrate in this solution for 20 min.

- HF acid clean: As before.

8. Metal depostion: Al
   - Load the wafer immediately into the Plassys loadlock after HF clean. Pump overnight
   - Deposit 80 nm at 12^0 deg tilt angle, 5 rpm planary rotation.
9. Al lithography
   - Resist spin coating:
     - Spin: PMGI SF7:
       * Step 1: 500 rpm, 100 rpm/s, 5 s
       * Step 2: 5000 rpm, 500 rpm/s, 60 s
     - Bake: at 150^0 C for 5 mins
     - Spin: S1811:
       * Step 1: 500 rpm, 100 rpm/s, 5 s
       * Step 2: 5000 rpm, 500 rpm/s, 60 s
     - Bake: at 120^0 C for 90 s
   - Optical lithography:
     - Using Mask aligner: Vac contact, 4.2s exposure, 30um Alignment gap, 5 s for all vacuum parameters
     - Using MaskLess Aligner,
       * Dose: 130 mJ/cmˆ2
       * Defocus: 2
   - Development: 47 s in MF319 solution, followed by DI water for 30 s.
10. Descumm
    - Procedure: Load wafers in the YES ASH tool and run recipe 6 – 6 times
    - Recipe 6: 50 W, 120 s, 25^0 C
11. Aluminum wet etching

- Use Aluminum Etchant A solution. Dip the wafer into this solution and slightly agitate. You will start to notice the Al etch in about 1min 30s. Rinse with DI water afterwards in two separate containers. Overetch to make sure all the Al is gone. Also, the time of etch depends on the temperature of the etch solution. Before beginning, wait for ˜10 min for the etch solution to thermalize to the ambient temperature.

12. Solvent cleaning

    - Clean wafers in a bath of PG Remover (20 mins) followed by a cold PG remover (5 mins) and IPA (5mins). I use the wafer cassette with wafers face down.

13. Dicing resist coating

    - Spin coating: Spin coat twice to get a thick resist layer. Make sure to bake them at each step
      - Spin S1811:
        * Step1: 500 rpm, 100 rpm/s, 5 s
        * Step2: 5000 rpm, 500 rpm/s, 60 s
      - Bake: at 120^0 C for 90 s
    - Alternatively, it is advisable to use SPR photoresist as a dicing resist as this gives a thicker film. The resist also easily strips down with Acetone and IPA.

14. Dicing

    - Dice wafer into blocks using the Disco Dicer tool. Make sure the blade is the right one for Silicon.

15. Block clean

    - Clean blocks in a bath of PG Remover (20 mins) followed by a cold PG remover (5 mins) and IPA (5mins).

16. Descumm

    - Procedure: Load wafers in the YES ASH tool and run recipe 6 – 6 times
    - Recipe 6: 50 W, 120 s, 25^0 C

17. Ebeam lithography

- Spin coating:
  - Spin PMGI SF11:
    - Step: 4000 rpm, 1000 rpm/s, 60 s. This gives ˜1200 nm
  - Bake: at 200^0 C for 10 min
  - Spin PMMA A3:
    - Step1: 5000 rpm, 1000 rpm/s, 60 s. This gives ˜120 nm
  - Bake: at 180^0 C for 5 min
- Ebeam writing:
  - RAITH:
    - @ 25KV: Smaller SQUID sections written with 10 um aperture @˜33 pA, dose factor (in CAD)=1.2. Larger SQUID sections written with 20um aperture @˜139 pA, dose factor (in CAD)=1. The dose factor in the position list is 1.05.
    - @15 KV The contact pads (big features) were written with 15um aperture @˜275 pA. The dose factor for both cad and position list is set to 1.
  - JEOL:
    - @ 100 kV: I use the top loading holder (2B)
      - Dose: 900 uC/cmˆ2 with PEC. The PEC file is simulated in Beamer.
      - Condition files: 2nA_AP60 (for the fine patterns) and 20nA_AP130 (for the coarse patterns)
- Development:
  - PMMA: 45s in MIBK:IPA (1:3) and 20 s in IPA, blow dry
  - PMGI: 25 s in developer concentrate, 30 s in DI water, 5 s in IPA, blow dry

18. Descumm
    - Procedure: Load wafers in the YES ASH tool and run recipe 8 – 1 time
19. Al deposition- SQUID fabrication
    - Procedure: Load the block into the Plassys loadlock. Pump the LL for 1.5 hours before loading it into the evaporation chamber.
    - Deposition angle: ±10∘
    - Ion milling: 1min at each angle

- Deposition thickness: 40 nm + 60 nm
- Oxidation parameters: 1Torr, 10 mins (Dynamic oxidation)

20. Liftoff of junctions

    - Hot PG Remover@ 70 deg (2-3 hrs) followed by cold PG remover (5 mins) and IPA (5mins). I use a pipette to gently squish liquid to aid liftoff. Also, use pipette to suck the film residues. Sonicate for 1 min in both solvents.

21. Dicing resist coating: same as before

22. Dice block

    - Dice block into chips using the Disco Dicer tool. Make sure the blade is the right one for Silicon. ALso check the dimensions of the chip beforehand

23. Chip clean

    - Clean chips in a bath of hot PG Remover (20 mins) followed by a cold PG remover (5 mins) and IPA (5mins). This step generally increases the junction resistance due to the hot PG remover. If cold PG remover is used, leave the chip for an hour.

24. Wire bonding

    - Use semi-automatic wire bonder to bond the chip to a PCB.